

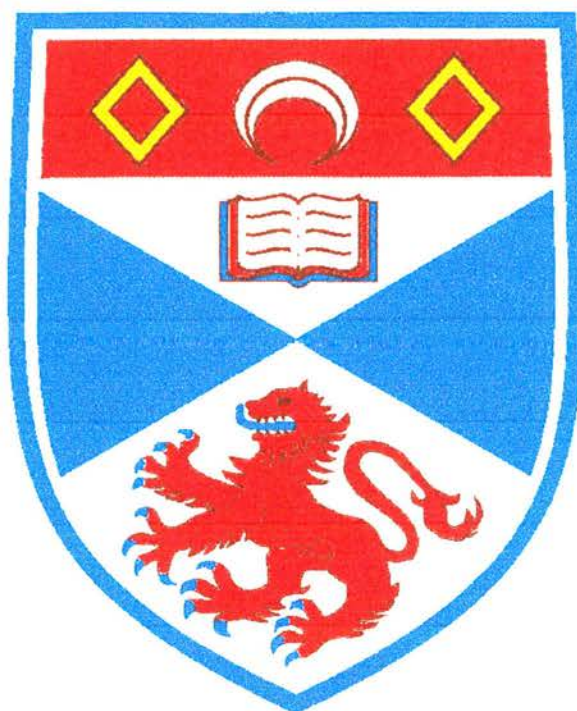
# University of St Andrews



Full metadata for this thesis is available in  
St Andrews Research Repository  
at:

<http://research-repository.st-andrews.ac.uk/>

This thesis is protected by original copyright



**Structural Studies of  
Technologically Important  
Compounds Using Powder  
Diffraction**

A Thesis presented for the degree of

Doctor of Philosophy

in the Faculty of Science of the University of St. Andrews

by Graham Stewart MacGlashan, *B.Sc.*

September 1999

School of Chemistry  
St. Andrews



## DECLARATION

I, Graham MacGlashan, hereby certify that this thesis, which is approximately 35,000 words in length, has been written by me, that it is a record of work carried out by me and that it has not been submitted in any previous application for a higher degree.

Date: 29/9/99      Signature of Candidate:

I was admitted as a research student in October 1995 and as a candidate for the degree of Doctor of Philosophy in September 1996; the higher study for which this is a record was carried out in the University of St. Andrews between 1995 and 1999.

Date: 29/9/99      Signature of Candidate:

## CERTIFICATION

I hereby certify that the candidate has fulfilled the conditions of the Resolution and Regulations appropriate for the degree of Doctor of Philosophy in the University of St. Andrews and that the candidate is qualified to submit this thesis in application for that degree.

Date: 29/9/99      Signature of Supervisor:

## LIBRARY DECLARATION

In submitting this thesis to the University of St. Andrews I understand that I am giving permission for it to be made available for use in accordance with the regulations of the University Library for the time being in force, subject to any copyright vested in the work not being affected thereby. I also understand that the title and abstract will be published, and that a copy will be made available to any bona fide library or research worker.

Date: 21/11/11 Signature of Candidate

## **Acknowledgements**

There are a great many people who I would like to thank for helping me through the last four years. Thanks must go to Professor Peter Bruce for his supervision, guidance, good judgement and help in guiding the project to fruition. An extra special mention has to go to Dr. Yuri Andreev for schooling me in structure solution and for his sorely tested patience, in particular his expertise in the spelling of names. This thesis is a testimony to his tutelage. Additional thanks also go to Dr. Ali Christie for introducing me to polymer electrolytes and some of the experimental aspects of my work in addition to lightening some dark days with his practical jokes and humour. Thanks are also due to Peter, Yuri and Ali for proof reading.

I would also like to mention the members of the PGB/CAV groups past and present for making my stay in St. Andrews as enjoyable as it was and for all the laughs and support.

Thanks to all my true friends for sticking with me and supporting me through the hard days as well as the good.

Finally, I must offer huge thanks to my family whose unwavering love and support have been appreciated beyond words.

## ABSTRACT

Three important crystalline polymer:salt compounds were fabricated and their crystal structures elucidated, in the cases of PEO:NaCF<sub>3</sub>SO<sub>3</sub> and PEO<sub>6</sub>:LiAsF<sub>6</sub> through application of a customised *ab-initio* structure solution method. The simulated annealing procedures used to solve each structure were developed such that they were unique for each structure solved and minimised computational time through the use of geometrical descriptions.

The structures of PEO:NaCF<sub>3</sub>SO<sub>3</sub> and PEO:KCF<sub>3</sub>SO<sub>3</sub> were shown to be 3 dimensional ionically cross linked structures. The PEO chains were shown to adopt stretched, zigzag chains. The anionic co-ordination was shown to vary, with the smaller sodium ion being six co-ordinated whilst the larger potassium ion being seven co-ordinated. The anions were shown to be not enveloped by the PEO chain.

The structure of PEO<sub>6</sub>:LiAsF<sub>6</sub> was shown to be a tunnelar structure showing several features which are unique amongst PEO:salt compounds. These include the fact that two PEO chains arrange themselves into two interlocking hemi-cylinders. Also unique is the way in which the cations do not interact with the anions, which are located inside the PEO cylinders.

Section	Title	Page no.
	Chapter 1: Modern Battery Developments	1
1.1	Introduction	1
1.2	Ionicly Conducting Polymer/Salt Complexes	5
1.3	Theoretical Treatments of Ionic Conduction in Polymer Electrolytes	12
1.4	Further Work	23
1.5	References	25
	Chapter 2: X-Ray Diffraction, Theory and Application	29
2.1	X-ray Diffraction Theory	30
2.2	Instrumentation & Structure Solution Techniques	40
2.3	Application of Structure Solution Using X-ray Diffraction to the Study of Ionicly Conducting Polymer:Salt Complexes	59
2.4	References	74
	Chapter 3: The Simulated Annealing Method of Ab-Initio Structure Solution from Powder Diffraction	77
3.1	Introduction	77
3.2	The Simulated Annealing Method	79
3.3	References	93
	Chapter 4: Ab-Initio Structure Solution of PEO:Sodium Trifluoromethane Sulphonate from Powder X-ray Diffraction Data	94
4.1	Introduction – The Need for Structure Solution	94
4.2	Experimental Details	95
4.3	Structure Determination	96
4.4	Discussions & Conclusions	106
4.5	References	110
	Chapter 5: The Structure Determination of PEO:KCF <sub>3</sub> SO <sub>3</sub> From Powder X-ray Diffraction Data Chapter 5: The Structure Determination of PEO:KCF <sub>3</sub> SO <sub>3</sub> From Powder X-ray Diffraction Data	128
5.1	Introduction	128
5.2	Phase Corroboration	129
5.3	Experimental Details	132
5.4	Discussions & Conclusions	135
5.5	References	140

Section	Title	Page no.
	Chapter 6: The Ab-Initio Structure Solution of PEO <sub>6</sub> :LiAsF <sub>6</sub> from Powder X-Ray and Neutron Diffraction Data	144
6.1	Introduction	144
6.2	Experimental Details	145
6.3	Structure Determination	147
6.4	Discussions & Conclusions	155
6.5	References	160
	Chapter 7: Conclusions and Further Work	
7.1	Introduction	180
7.2	The Effect of Salt Concentration	181
7.3	The Effect of Cation Variation	188
7.4	The Effect of Anion Variation	191
7.5	Suggestions for Further Work	193
7.6	References	196
App.1	Published Papers	210
App.2	Table of Data on PEO:salt Crystal Structures	211

# Chapter 1: Modern Battery Developments

## Section 1.1: Introduction

A major feature of the recent expansion of consumer electronics has been the increased demand for portable applications<sup>1,2,3</sup>. This increased demand has arisen from the expansion in the scope of consumer electronics, which, in turn has developed in part from applications that relied on digital processing. This can be seen around us today with the increased prevalence of portable items of consumer electronics such as mobile phones, laptop computers, pagers, personal compact disk players and personal television sets. Everyday use of this new, portable technology relies heavily on the batteries that are used to power them.

Battery technology originated over 100 years ago with the most widespread primary battery, the Zinc-Carbon Leclanché cell<sup>4</sup>, first being developed in 1866, and the worlds most widely used secondary battery, the lead-acid cell being first proposed by Planté in 1854<sup>5</sup>. Whilst many improvements have been made on these cells since their invention, such battery designs have many shortcomings when faced with the challenges of new technologies. Modern consumers demand portable devices that are smaller yet maintain high charge capacity and are environmentally friendly. Traditional batteries, such as Zinc-Carbon, Nickel-Cadmium and lead-acid cells have limitations that include poor energy density, a high

weight to power ratio, a tendency to self discharge, a high manufacturing cost, hazardous leakage products, poor cyclability and environmentally unfriendly components such as cadmium and lead<sup>1</sup>. One promising avenue is the use of lithium based technology to overcome these shortcomings.

<b>METAL</b>	<b>Specific Capacity / A h kg<sup>-1</sup></b>	<b>E<sup>o</sup>'s / V</b>
Lithium	3860	-3.04
Sodium	2923	-2.71
Zinc	820	-0.76
Lead	260	-0.13

Table 1. Comparison of Specific capacity and standard reduction potential for some metals frequently found in batteries.

Table 1 demonstrates why the material of choice for modern batteries is lithium. However, the reactivity of lithium, specifically its high negative potential, creates its own problems. Conventional aqueous electrolytes are clearly unsuitable as they could be susceptible to reaction with lithium, thus, non-aqueous materials such as organic or polymeric solvents must be used to dissolve an appropriate lithium-based salt.

Initially, cells were developed that included a lithium anode separated by the liquid electrolyte from the cathode, which was generally a composite material such as V<sub>6</sub>O<sub>13</sub>, TiS<sub>2</sub> or MnO<sub>2</sub>. These cathode materials function

as intercalation compounds that allow the lithium ions to reversibly intercalate into spaces in the host lattice. However, batteries of this nature were prone to problems, particularly on recharging. During this process, metallic lithium is plated onto the anode. At high rates or in some solvents, this can cause dendrite or needle growth of very reactive lithium which can result in short-circuits and overheating. Modern design tends to substitute an insertion compound such as graphite in place of the lithium anode. Batteries of this type where lithium ions are reversibly inserted and removed from both the negative and positive electrodes are termed “rocking chair cells” or more recently, lithium-ion cells, fig. 1.1.

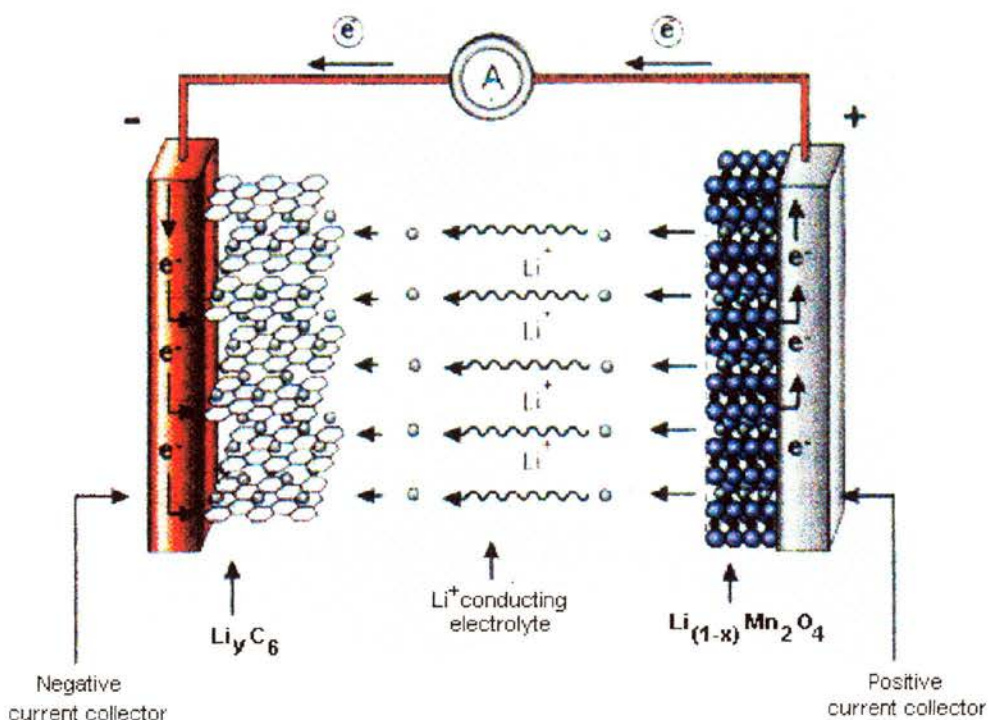


Figure 1.1. A schematic of a typical rocking chair cell, from ref.17.

Solvent free polymer electrolytes have another important advantage in addition to those mentioned above. They may make possible the construction of safe lithium metal anode based cells. This arises because on charging, the solid polymer inhibits dendrite formation, encouraging the formation of a stable lithium interface. Most notably, Hydro-Quebec in Canada is developing such a battery for electric vehicle applications.

When choosing the material for use as the electrolyte, polymeric materials have some distinct advantages over liquid organic solvents. For instance, they can be cast as thin films with a large surface area, thus

allowing high power levels ( $>100 \text{ W dm}^{-3}$ )<sup>1</sup> to be reached. In addition, the solid film-like properties of this type of electrolyte allow the use of simpler mass production techniques, leading to a cheaper product. Furthermore, the plastic nature of these materials allows for expansion and contraction within the cell without cracking of the electrolyte or degradation of the electrode / electrolyte interface, in this sense, they are superior to ceramic electrolytes. Electrolytes based on high molecular weight polymers have the advantage that their solid structure prevents migration of the solvent with the mobile ionic species thus preventing significant volume change. The most common form of polymer electrolyte is the gel electrolyte, which consists of very short chain solvent molecular species such as propylene carbonate, di-methyl carbonate and ethyl methyl carbonate in a polymer host. These materials involve co-ordination of the cationic species primarily by the solvent, which then diffuses with the cation through the electrolyte. The physical properties of these materials may be altered by selection of the gel host as well as by altering the type and composition of solvent. The gel electrolytes offer the highest ionic conductivity of this class of compound but have less favourable physical and mechanical properties than polymer electrolytes.

### **Section 1.2: Ionically conducting Polymer/Salt complexes**

In 1973, Wright and co-workers<sup>6</sup> reported the discovery that certain alkali metal salts, when dissolved in poly(ethylene oxide), commonly known as

PEO, formed an ionically conducting polymeric material. Despite this, the use of these materials as electrolytes was not widely recognised until Armand<sup>7</sup> began to develop these materials in 1978. Since then, the field has seen great expansion in the range of polymer hosts<sup>8-10</sup> and salts<sup>11,12</sup> used. In addition, the range of potential applications has grown, with proposed uses including electrochromic devices and ionic sensors<sup>1</sup> as well as batteries.

Electrochromic devices, such as smart windows, are devices that use electrochemical methods to effect a change in colour or transparency. Polymer electrolytes have successfully been used to facilitate a transparent ion conduction pathway in these devices<sup>13</sup>. Further uses include an internal ionic bridge in ion sensors<sup>14</sup>, however, the main impetus for development of these materials remains battery applications.

Given the obvious potential for commercial application of these true polymer electrolytes, it is desirable to investigate the morphology and conduction mechanism of this type of compound. In general, polymer-salt complexes can be considered in terms of either the crystalline or amorphous state, although the two are often concurrently present. The most important state in terms of ionic conduction is the amorphous state, above the glass transition temperature,  $T_g$ , since the conductivities achievable in this state are vastly superior to those achieved in the

corresponding crystalline phase. The amorphous state is typified by a near complete lack of long range order in the material. It has been postulated that the amorphous state of PEO:salt compounds consists largely of randomly oriented, short-range sections of crystalline type environments<sup>16</sup>. This has been supported by recent results<sup>16-17</sup> which reported that the structure of crystalline  $\text{PEO}_3:\text{LiCF}_3\text{SO}_3$  remained essentially unchanged up to its melting point and that the local environment around the ions and polymer did not significantly change upon entering the amorphous state above this temperature. The amorphous phase is a glass when below  $T_g$ , where molecular motion is generally restricted to short range vibrations and rotations, it transforms to a liquid state above  $T_g$  in which there is a far greater degree of conformational freedom. At  $T_g$ , an increase in free volume can be observed in the material as well as a variation in the rate of change of entropy. This is indicative of a system that allows greater segmental motion of the chain, in which for poly(ethylene oxide) typically 18 – 51 atoms are moving together. There is a considerably increased ionic conduction above the glass transition temperature and this is attributed to the segmental motion of the chain inducing fluctuating free volume, allowing a greater degree of “passing” of the anion along and between chains thus leading to greater diffusivity. However, although the structure of this state has been studied using Raman, IR, NMR and EXAFS techniques amongst others, interpreting the data generally relies on an

accurate structural model as a basis of the calculations. It is my contention that the best approach to studying the structure of the amorphous state is to first establish the structure of the analogous crystalline polymer-salt complexes using diffraction techniques. The unambiguous information provides a more robust basis for subsequent analysis of spectroscopic studies of the amorphous state.

The crystalline state arises when the nature of the polymer chains and dissolved salt is such that it allows them to align in a regular, ordered, fashion. This arrangement usually corresponds to a minimum energy state and thus segmental motion is suppressed. This leads to a reduction of ionic mobility as described in chapter 1.3 and indeed only very low ionic conductivities are observed in the crystalline state. However, what is generally considered to be the crystalline state in PEO:salt complexes is rarely purely crystalline as described by the fringed micelle model.

The polymer chains can be shown<sup>18</sup> to be folded and arranged in plate-like lamellae such that the chain axis is parallel with the shortest dimension of the lamella. A single polymer chain may span more than one lamella, resulting in a linked, branched network of lamellae and this has been given credit for some of the physical resilience of these materials. These tend to order themselves into pom-pom type three-dimensional spheres termed spherulites. These spherulites consist of

several lamellae radiating from a central point with the chain axis of the individual polymer chains tending to lie perpendicular to the radius of the spherulite. The spherulites tend to grow until they impinge on another spherulite. This leaves gaps in the structure, which generally contain a semi-crystalline phase consisting of pure polymer with dissolved salt. These regions tend to crystallise very slowly and as a result, they can be considered to be in a non-static condition.

Despite this doubt as to the validity of phase equilibrium, phase diagrams can provide a useful reference when it comes to production of materials of a desired crystallinity or composition. However, it should be stressed again that the kinetics of these systems are slow and non-equilibrium states are probable which, when coupled with the fact that different fabrication techniques can lead to slightly varying materials, means that phase diagrams should only be taken as a rough guide to thermal properties. Thermal characterisation has been greatly helped by the proliferation of thermal analysis techniques such as differential scanning calorimetry (DSC), thermal gravimetric analysis (TGA) and variable temperature powder X-ray diffraction (VTXRD). Several polymer-salt systems have been studied and the thermal properties can vary markedly from system to system depending on the polymer and salt under investigation. The most studied systems are those that involve

poly(ethylene oxide), PEO, as the host polymer and some useful trends can be observed from this work.

Crystalline complexes tend to form at only certain discrete compositions. The most common include complexes with an ethylene oxide (EO) unit to salt ratio of 3:1 including many lithium compounds such as  $\text{PEO}_3\text{LiI}^{19}$ ,  $\text{PEO}_3\text{:LiAsF}_6^{20}$ ,  $\text{PEO}_3\text{:LiClO}_4^{21}$  and  $\text{PEO}_3\text{:LiCF}_3\text{SO}_3^{21}$  as well as some sodium compounds such as  $\text{PEO}_3\text{:NaSCN}^{22}$  and  $\text{PEO}_3\text{:NaI}^{23}$ . The compounds with larger cations such as  $\text{K}^+$  and  $\text{NH}_4^+$  tend to form complexes with an EO:salt ratio of 4:1 such as  $\text{PEO}_4\text{:KSCN}$  and  $\text{PEO}_4\text{:NH}_4\text{SCN}^{24}$ . However, many crystalline complexes with differing EO:salt ratios have been discovered and the composition of the complex appears to be a function of both the anion and cation as indicated by the existence of, for example,  $\text{PEO}_5\text{:NaB(Ph)}_4$  and  $\text{PEO}_8\text{:NaB(Ph)}_4^{25}$ .

Having already examined the composition and morphology of polymer-salt complexes it is now prudent to consider the mechanism by which these polymers ionically conduct and which properties or features are favourable when it comes to choosing the polymer for use as an ionic conductor. For a polymer to be suitable, it must be able to solvate the cation as well as conduct it. A key feature of this is the polymer-salt interaction. This is heavily influenced, like many salt-neutral species interactions, on the ability of the host, in this case the polymer, to donate

electrons, its ability to accept electrons and the consideration of entropy. These determine its effectiveness as a cationic solvent, its effectiveness as an anionic solvent, and its stability respectively. To satisfy the electron donor requirement, a suitable polymer must contain charged sites that can associate with the mobile ion, resulting in co-ordination bonds between the ion and the polymer. Furthermore, these negative sites must be optimally spaced to ensure that the polymer chain can suitably interact with the ion. In addition, for successful conduction to take place, polymer electrolytes of this type rely on movement of ions in addition to local segmental motion of the chain combined with the effects of inter-chain hopping. Thus, segmental motion of the chain must not be too hindered, sterically or otherwise, allowing conduction of the ion by means of conformational rearrangement in the polymer chain. Examples of such polymers include PEO and poly(ethylene imine) or PEI.

Once the salt is solvated, the important factor in the use of these materials is their conductivity. Since conduction of ions in these materials is largely in the amorphous phase, the tendency of a compound to form a crystalline material and the temperature at which it undergoes a glass transition,  $T_g$ , are also important factors. However, for improvement of the properties and for material selection it is important to collate these factors, along with some of the observable or desirable properties, into a

theoretical treatment of the conduction mechanism for these polymer/salt complexes.

### **Section 1.3: Theoretical Treatments of Ionic Conduction in Polymer Electrolytes**

The transport of ions is fundamental to the usefulness of polymer/salt complexes in applications such as electrolytes and there have been several varying approaches to the theoretical modelling of the ionic transport process. There are also various quantities whose successful prediction can be used as a measure of the success of a theory. These include conductivity, viscosity and the diffusion coefficient. In addition to simple prediction of measurable quantities, a theoretical treatment can be viewed to be even more successful if it gives a greater insight into the actual microscopic conduction mechanism. Conduction can be considered as having two components, electronic and ionic. In most polymer/salt complexes there is convincing evidence that conduction is overwhelmingly ionic. This was shown in the work by Dupon et al.<sup>26</sup> who calculated the ratio of ionic to electronic conduction by comparing the current through a cell containing ion blocking electrodes versus the current through an equivalent cell with ion-reversible electrodes. Supporting evidence can be found in the fact that for all but very high ionic concentrations, conduction increases with salt concentration. Furthermore, the host polymer in these systems generally lacks

conjugation or charge transfer structures that would be crucial to electronic conduction. Thus, having established that conduction is mainly ionic, a mechanism for this conduction may be considered.

Ionic conduction is expressed by the following equation:

$$\sigma = \sum_{i \text{ carriers}} n_i q_i \mu_i \quad \text{Eqn. 1.1}$$

Where  $\sigma$  is the ionic conductivity,  $n_i$  is the number of carrier ions of species  $i$ ,  $q_i$  is the charge of species  $i$  and  $\mu_i$  is the ionic mobility. If the assumption is made that the number of carriers and amount of charge remains largely constant, then the ionic conductivity becomes a function of the ionic mobility. There has been much conjecture as to the mechanism of conduction and the factors affecting ionic mobility, which remains of considerable debate. However, there are many approaches that attempt to obtain useful relationships from experimental findings without much consideration of mechanistic detail. These include the use of the Williams-Landel-Ferry (WLF) equation<sup>27</sup>, which was originally used to describe the dependence of conductivity with temperature in liquid like systems:

$$\log \left[ \frac{\sigma(T)}{\sigma(T_g)} \right] = \frac{C_1(T - T_g)}{C + (T - T_g)} \quad \text{Eqn. 1.2}$$

Where  $T_g$  is the glass transition temperature whilst  $C_1$  and  $C_2$  are constants which are calculated experimentally but may be given significance in the free volume theory.

Most initial theories were based around free volume theory, which is itself based on the premise that the transport of particles is dependent on the formation of holes or free volume large enough for the particle to diffuse into. The free volume is redistributed through a process of segmental motion of the chain. This approach gives good predictions for the temperature dependence of transport properties such as conductivity and diffusivity as well as properties such as viscosity. Most of the experimental work using this theory involves the application of the Vogel-Tamman-Fulcher (VTF) equation<sup>28-30</sup>:

$$\sigma = \frac{A}{\sqrt{T}} \exp\left[\frac{-B}{T - T_o}\right] \quad \text{Eqn. 1.3}$$

Where  $A$  is a constant which is proportional to the number of carrier ions,  $B$  is also a constant and  $T_o$  is the temperature at which configurational entropy is zero. The free volume theory of which both the WLF and VTF equations are part has its origins in the work of Cohen and Turnbull<sup>31</sup> on the diffusion of small particles in amorphous media. As part of this, it was

shown that the diffusion coefficient could be expressed using the following equation:

$$D = g d v \exp\left(\frac{-\gamma V^*}{V_f}\right) \quad \text{Eqn.1.4}$$

Where  $g$  is a constant which is approximately  $1/6$ ,  $d$  is the distance through which a particle is transported, which in this case can be approximated to be a molecular diameter,  $v$  is the particle velocity which is proportional to  $T^{1/2}$ ,  $\gamma$  is a free volume overlap factor,  $V^*$  is the volume required for the particle to move and  $V_f$  is the free volume of the system which is temperature dependent and can be expressed by the equation:

$$V_f = V_g [f_g + \alpha(T - T_g)] \quad \text{Eqn. 1.5}$$

Where  $V_g$  is the specific volume at the glass transition temperature,  $\alpha$  is the free volume expansion co-efficient and  $f_g$  is the fraction of volume which is free volume at the glass transition temperature. Thus, by combining equations 1.4 and 1.5, it is possible to derive the following relationship:

$$\log\left[\frac{D(T)}{D(T_g)}\right] \approx \left\{ \frac{\gamma V^* (T - T_g)}{2.303 V_g V_f \left(\frac{f_g}{\alpha} + (T - T_g)\right)} \right\} \quad \text{Eqn. 1.6}$$

Also of use is the Nernst-Einstein equation, which relates the mobility of an ion to its diffusion coefficient:

$$\mu_i = q_i D_i / kT \quad \text{Eqn. 1.7}$$

If we assume that there is only one ionic species migrating in polymer electrolytes and that the variation of the number of carriers with temperature is negligible then from equations 1.1 and 1.7 it can be shown that:

$$\log \left[ \frac{\sigma(T)}{\sigma(T_g)} \right] \approx \log \left[ \frac{D(T)}{D(T_g)} \right] \quad \text{Eqn. 1.8}$$

Thus substituting in equation 1.6 gives the WLF equation, Eqn. 1.2, but with the constants

$$C_1 = \gamma V_i^* / 2.303 V_g f_g \text{ and } C_2 = f_g / \alpha$$

Similarly, if equations 1.1, 1.4 and 1.7 are combined then the following relationship can be obtained:

$$\sigma = [nq^2 / kT] g d v \exp(-\gamma V_i^* / V_i) \quad \text{Eqn. 1.9}$$

Thus by substituting in equation 1.5 and assuming velocity to be proportional to  $T^{1/2}$  i.e.  $v=mT^{1/2}$  where  $m$  is a constant and furthermore assuming that the fraction of free volume at  $T_g$  is negligible, then the VTF equation may be derived with:

$$A = [nq^2/k]gdm \text{ and } B=2.303C_1C_2$$

These equations can be used to investigate some interesting properties for example, the segmental motion of the chain. Using a similar treatment to that employed previously, the segmental mobility of the chain, which is inversely proportional to its relaxation time,  $\tau$ , which may be measured experimentally, can be expressed in terms of its temperature dependence:

$$\log \left[ \frac{\tau(T_g)}{\tau(T)} \right] = \frac{C_1'(T - T_g)}{C_2' + (T - T_g)} = -\log a_T \quad \text{Eqn. 1.10}$$

Where  $C_1' = \gamma V_s^*/2.303V_g f_g$ ,  $C_2' = f_g/\alpha$  and  $V_s^*$  is the free volume required for a unit of chain to move into it.

Thus, the conductivity may be related to segmental motion of the chain in the following fashion:

$$\log \left[ \frac{\sigma(T)}{\sigma(T_g)} \right] = -\frac{V_i^*}{V_s^*} \log a_T \quad \text{Eqn. 1.11}$$

For many systems, a plot of  $\log[\sigma(T)]$  against  $-\log(a_T)$ , where  $a_T$  is the WLF shift factor, is linear with a slope of unity<sup>32-33</sup>. This suggests that the carrier ion and the moving polymer unit have the same jump frequency. The fact that the small ion moves at the same rate as a motion of a much larger polymer unit would be surprising unless the segmental motions controlling free volume distribution are considered to be the rate determining process in ionic conduction. Despite the successes of free volume theory, there are discrepancies in the theory. These include the fact that conductivity at reduced temperature can increase by a factor of 10-100 times with increasing salt concentration whereas free volume theory predicts constant ionic mobilities at a constant reduced temperature ( $T-T_g$ ). Also, free volume theory, whilst accurately predicting transport properties such as conductivity and diffusivity only takes into account carrier migration, not formation. There are other theories with a similar basis to free volume theory such as the configurational entropy model proposed by Gibbs et al.<sup>34-35</sup> and extended by Ratner<sup>36</sup>.

This model, like free volume theory, is based solely on the properties of the host lattice, in this case the polymer. Configurational entropy theory treats the transport mechanism as a co-operative group rearrangement of the polymer chain with a rearrangement probability of:

$$W = C \exp\left[\frac{-\Delta\mu S_c^*}{kTS_c}\right] \quad \text{Eqn. 1.12}$$

Where  $S_c^*$  is the minimum configurational entropy needed for a chain rearrangement,  $S_c$  is the configurational entropy at temperature  $T$ ,  $C$  is a constant and  $\Delta\mu$  is the free energy barrier per mole which has to be overcome for a rearrangement to take place.

This theory can be used to give analogs of the WLF and VTF equations but the constants in the WLF and VTF equations are now variables. The theory has been successfully applied to polymer:salt systems by Cowie<sup>37</sup>. However, macroscopic approaches such as configurational entropy theory and free volume theory lack mechanistic detail concerning the ionic conduction process. Clearly a more microscopic approach is required to accurately describe the mechanism of ionic conduction and to understand frequency dependent observations such as spectroscopic results and dielectric relaxation.

The initial microscopic theories involved ions travelling down cylinders formed by polymer chains such as in the proposal by Armand<sup>38</sup>. However, it was noted that the conduction is almost exclusively in the amorphous phase where any polymer structures would be more chaotic than in the crystalline phase and therefore should give rise to poorer

conduction. Furthermore, work by Dupon<sup>39</sup> showed that the addition of ion-paired NaBH<sub>4</sub> to a PEO:NaBF<sub>4</sub> complex does not reduce the sodium conductivity which might be expected with the neutral ion pairs blocking some polymer “tunnels”.

Static percolation theory has been successfully used to model transport processes in disordered systems<sup>40</sup>. This theory involves defining a set of possible sites that the carrier can occupy. The rate of transport between sites is then determined using the following equation:

$$P_i = \sum_j^k P_j W_{ji} - P_i W_{ij} \quad \text{Eqn. 1.13}$$

Where  $P_i$  is the probability of finding a carrier on site  $i$  at time  $t$  and  $W_{ji}$  is the rate at which carriers move from site  $j$  to site  $i$ . The carriers are limited to movements between nearest neighbour sites up to site  $k$ . If it is possible for a carrier to move from one site to another, then a pathway is said to exist between the two sites. The number of pathways is determined at the start of the calculation and remains fixed. This leads to a rate of transport defined as:

0, Probability of  $1-f$

$W_{ij} = w$ , Probability of  $f$

Where  $f$  is the fraction of pathways which are available to the carrier.

This theory allows for independent motion of carriers but is fundamentally flawed in that it models the co-ordination sites of the host polymer as a static, regular array of lattice points. So whilst this theory has some uses, for example, modelling of the effects of interspersed crystalline and amorphous regions, its application in the modelling of ionic conduction mechanisms needs some refining.

Dynamic bond percolation theory is a modification of static percolation theory, which contains an allowance for reassignment of pathways at a frequency,  $\lambda$ . This is an analogue of segmental motion of the chain in which co-ordinating sites are constantly being brought into and moved out of "hopping range" of the cation. The hopping probabilities are thereby a function of  $w$ ,  $f$  and  $\lambda$  which can then be related to physical observations. This theory can be used to successfully describe frequency dependent behaviour such as microwave conductivity<sup>41</sup>. It can also describe the effects on ionic conduction of varying renewal times, i.e. rate of segmental motion and observation time. However successful, there are still many shortcomings of these theories. Their validity is limited by

assumptions such as the host species is a regular lattice, which is not a good representation of an amorphous, elastomeric polymer. Furthermore, the assumption that the carrier is an independent particle is suspect due to the fact that ionically conducting polymer-salt complexes generally have sufficiently high salt concentration to allow coulombic interactions between carriers. This leads to phenomenon, such as ion pairing, which can have a highly significant effect on ionic mobility and conductivity. However, attempts have been made to compensate for ionic interactions by Ratner and Nitzen<sup>42</sup> who have proposed a model which has contributions based on ionic cross linking of polymer chains.

In summary, there are a wide range of approaches and theories available, each with its own successes and shortcomings. Thus, the correct approach has to be selected according to the nature of the experiment and the type of results required. However, despite the disparity, there are several features in common. There is an overall concept of the cation being co-ordinated by an envelope of electronegative sites on the polymer backbone with conduction being controlled by modification of the coordination sphere through segmental motion of the chain. This concept remains constant throughout all of the approaches detailed here. Despite this, further work is required in order to create a "unified" theory that addresses the shortcomings of the approaches detailed here and also presents a useful microscopic picture of the conduction mechanism.

#### **Section 1.4: Further Work**

Clearly, a full understanding of the conduction mechanism and the factors affecting it are essential for optimisation of these materials for application purposes. At the same time, the nature and significance of the actual mobile species (ion pairs, clusters etc.) requires further investigation. It is in order to address these issues that we have embarked on the present structural studies. Furthermore, the structural chemistry of polymer electrolytes is not established to any significant degree. A great many polymer-salt complexes have been prepared and they represent a unique class of co-ordination compound standing between conventional discrete molecular complexes and conventional solid state chemistry.

There are two main problems in applying diffraction techniques to study polymer electrolyte structure. The first is that although many crystalline polymer-salt complexes have been prepared previously, it is generally difficult or impossible to produce crystals that yield single crystal diffraction patterns of sufficient quality for analysis by that technique. Powder diffraction is the only route to the application of crystallographic methods. Although it is at least possible to produce polymer electrolyte samples for powder diffraction it presents a challenge to produce samples capable of yielding the high quality powder data so essential to successful structural studies.

The second problem with the use of powder X-ray diffraction, is that it is difficult to solve compounds for which no good starting model of the structure is already available, especially if there is no dominant scattering from a heavy atom. Despite this, ab-initio structure solution using powder diffraction data is being made more accessible by exciting developments in structure solution methods such as simulated annealing and genetic algorithm based methods, of which more is discussed later.

## Section 1.5: References

- [1] F.M.Gray, *Solid Polymer Electrolytes - Fundamentals and Technological Applications*, VCH publishers, New York, 1991
- [2] C.A.Vincent, *Chemistry and Industry*, Sept. 1996
- [3] Emerging Technologies Report, Institute of Electrical and Electronics Engineers, 1995
- [4] G.Leclanché, French Patent No. 71865, 1866
- [5] H.Bode, *Lead-Acid Batteries*, John Wiley & Sons, New York, 1997
- [6] D.E.Fenton, J.M.Parker, P.V.Wright, *Polymer*, **14** (1973) 589
- [7] M.B.Armand, J.M.Chabagno, M.Duclot, *Second International Meeting on Solid Electrolytes - St. Andrews, Scotland, 20-22 September 1978, extended abstract*
- [8] L.Wang, B.Yang, X.L.Wang, X.Z.Tang, *Journal of Applied Polymer Science*, **71** (1999) 1711
- [9] F.Alloin, J.Y.Sanchez, M.Armand, *J. Electrochem. Soc.*, **141** (1994) 1915
- [10] F.B.Dias, S.V.Batty, J.P.Voss, G.Ungar, P.V.Wright, *Solid State Ionics*, **85** (1996) 43
- [11] D.Benrabah, J.Y.Sanchez, M.Armand, *Solid State Ionics*, **60** (1993) 87
- [12] D.Benrabah, J.Y.Sanchez, D.Deroo, M.Armand, *Solid State Ionics*, **70** (1994) 157

- [13] R.B.Goldner, T.E.Haas, G.Seward, K.K.Wong, P.Norton, G.Foley, G.Berera, G.Wei, S.Schultz, R.Chapman, *Solid State Ionics*, **28-30** (1988) 1715
- [14] P.Fabry, C.Montero-Ocampo, M.Armand, *Sensors Actuators*, **15** 1988, 1
- [15] A.M.Christie, Personal Communication
- [16] R.Frech, S.Chintipalli, P.G.Bruce, C.A.Vincent, *Chem. Commun.*, **2** (1997) 157
- [17] J.B.Thomson, Ph.D. Thesis, University of St.Andrews (1996)
- [18] H.D.Kieth, F.J.Padden, *J. Appl. Phys.*, **34** (1963) 2409
- [19] D.Fateaux, Ph.D. Thesis, INRS
- [20] M.Z.A.Munshi, B.B.Owens, *Appl. Phys. Commun.*, **6** (1987) 279
- [21] C.D.Robitaille, D.Fateaux, *J. Electrochem. Soc.*, **133** (1986) 315
- [22] C.D.Robitaille, S.Marquis, D.Bolis, J.Prud'homme, *Macromolecules*, **20** (1987) 3023
- [23] Y.Chatani, S.Okamura, *Polymer*, **28** (1985) 1815
- [24] P.Lightfoot, J.L.Nowinski, P.G.Bruce, *J. Am. Chem. Soc.*, **116** (1994) 7469
- [25] S.Besner, A.Valleé, J.Prud'homme, *Polym. Prepr.*, **30** (1989) 406
- [26] R.Dupon, D.H.Whitmore, D.F.Schrifer, *J. Electrochem. Soc.*, **138** (1981) 715
- [27] M.L.Williams, R.F.Landel, J.D.Ferry, *J. Amer. Chem. Soc.*, **77** (1955) 3701

- [28] H.Vogel, *Phys. Z.*, **22** (1921) 645
- [29] G.Tamman, W.Hesse, *Z. Anorg. Allg. Chem.*, **156** (1926) 245
- [30] G.S.Fulcher, *J. Amer. Ceram. Soc.*, **8** (1925) 339
- [31] M.H.Cohen, D.Turnbull, *J. Chem. Phys.*, **31** (1959) 1164
- [32] A.Killis, J.F.LeNest, H.Cheradame, A.Gandini, *Makromol. Chem.*, **183** (1982) 2835
- [33] H.Cheradame, *IUPAC Macromolecules*, ed. H.Benoit, P.Remp, Pergamon Press, Oxford (1982) 251
- [34] J.H.Gibbs, E.A.DiMarzio, *J. Chem. Phys.*, **28** (1958) 373
- [35] J.H.Gibbs, *Modern Aspects of the Vitreous State*, Butterworths, London (1965)
- [36] B.L.Papke, M.A.Ratner, D.F.Schrifer, *J. Electrochem. Soc.*, **129** (1982) 1694
- [37] J.M.G.Cowie, A.C.S.Martin, A.M.Firth, *Br. Polym. J.*, **20** (1988) 247
- [38] M.B.Armand, J.M.Chabagno, M.J.Duclot, *Fast-Ion Transport in Solids*, eds. P.Vashishta, J.N.Munday, G.Shenog, North-Holland, Amsterdam (1979) 247
- [39] R.Dupon, B.L.Papke, M.A.Ratner, D.H.Whitmore, D.Schrifer, *J. Amer. Chem. Soc.*, **104** (1982) 6247
- [40] R.Zallen, *The Physics of Amorphous Solids*, Wiley, New York (1983)

- [41] S.D.Druger, M.A.Ratner, A.Nitzan, *Solid State Ionics*, **18/19**  
(1986) 106
- [42] M.A.Ratner, A.Nitzan, *Faraday Discuss. Chem. Soc.*, **88** (1989)  
19

## Chapter 2: X-Ray Diffraction, Theory and Application

Improved understanding of the key features of ionically conducting polymers such as polymer ion interactions, polymer conformation and cation-anion interactions are crucial to a greater understanding of the conduction mechanism and chemistry of these materials<sup>1</sup>. Information on local order and environments can be obtained using a variety of spectroscopic techniques including IR, Raman solid state NMR and EXAFS. However, the majority of long range structural information of compounds in the crystalline state has been discovered using various diffraction methods, most notably single crystal x-ray diffraction. As noted in the previous chapter, ionically conducting polymeric materials of this type only exhibit useful conductivity in the amorphous state. However, knowledge of the crystalline state structure can be used as a good starting basis for investigations of the amorphous state<sup>2,3</sup>. In addition, it has been shown using IR spectroscopy that in the case of  $\text{PEO}_3:\text{LiCF}_3\text{SO}_3$ , the lithium and triflate environments are virtually identical in the crystalline and amorphous states<sup>3</sup>. Thus it can be hypothesised that the amorphous structure of this class of compound consists in the short range, of the same structure in the crystalline and amorphous states. However, another problem arises in that in most ionically conducting polymer systems, it is difficult or impossible to

synthesise single crystals of a suitable standard. Thus the main technique implemented in this work was powder x-ray diffraction.

### **Section 2.1: X-Ray Diffraction Theory<sup>4,5,6</sup>**

Diffraction effects arise when radiation passes through a diffraction grating where the diffracting objects are spaced a distance apart which is roughly comparable with the wavelength of the radiation. Thus for diffraction from atoms which are typically spaced 1-4Å apart, x-ray radiation, having a wavelength of 0.4-2.5Å, is suitable (1Å=10<sup>-10</sup>m). In laboratory x-ray diffractometers, x-rays are produced by accelerating electrons from a heated filament through an electric field and using them to bombard a metal target, such as copper, molybdenum or iron. The set-up of the apparatus is such that the energy of the electron is enough to ionize electrons from the K (1s) shell of the target atoms. Electrons from the higher energy L (2p) or M (3p) shells then fill these vacancies with the release of the difference of energy as electromagnetic radiation, in this case, x-rays. The L → K transition gives rise to two particularly intense K $\alpha_1$  and K $\alpha_2$  lines whilst the M → K transition leads to the K $\beta_1$  and K $\beta_2$  doublet. The double lines arise from the existence of two possible electronic configurations that vary slightly in energy. Since the energy of the L levels is lower than that of the M levels, by the Boltzmann distribution law, the L → K transitions are more probable, thus the K $\alpha$  transitions are more intense. The K $\alpha_1$  peak can be solely selected from

the incident radiation through the use of a monochromator, to select the required wavelength. Therefore, the wavelength of radiation can be selected to a certain extent by varying the peak selected or by varying the element, since the wavelength of the characteristic emissions decreases with increasing atomic number. Typical wavelengths produced include  $\lambda=1.54051\text{\AA}$  for Cu  $K\alpha_1$  and  $\lambda=0.71354\text{\AA}$  for Mo  $K\beta_1$ .

Having produced the radiation, it is now pertinent to examine its diffraction from crystals. Crystalline materials are those which contain a structural unit (basis) which is repeated many times by translation to give the crystal structure. The lattice is defined as an array of equivalent points that can be superimposed onto one another by translation using a lattice vector:

$$\underline{T} = u_1\underline{a}_1 + u_2\underline{a}_2 + u_3\underline{a}_3$$

Where  $u_j$  is the vector magnitude and  $\underline{a}_j$  is the unitary direction vector between two lattice points. The lattice may also be described in reciprocal space where the primitive lattice vectors are of the form

$$\underline{b}_1 = (2\pi\underline{a}_2 \wedge \underline{a}_3) / [\underline{a}_1 \underline{a}_2 \underline{a}_3], \underline{b}_2 = (2\pi\underline{a}_1 \wedge \underline{a}_3) / [\underline{a}_1 \underline{a}_2 \underline{a}_3], \underline{b}_3 = (2\pi\underline{a}_1 \wedge \underline{a}_2) / [\underline{a}_1 \underline{a}_2 \underline{a}_3]$$

Which gives a reciprocal lattice vector of:

$$\underline{G} = v_1\underline{b}_1 + v_2\underline{b}_2 + v_3\underline{b}_3$$

Where  $v_i$  is the magnitude and  $\underline{b}_i$  is the direction vector between two points in the reciprocal lattice. The crystal then diffracts the incident radiation in a definite manner.

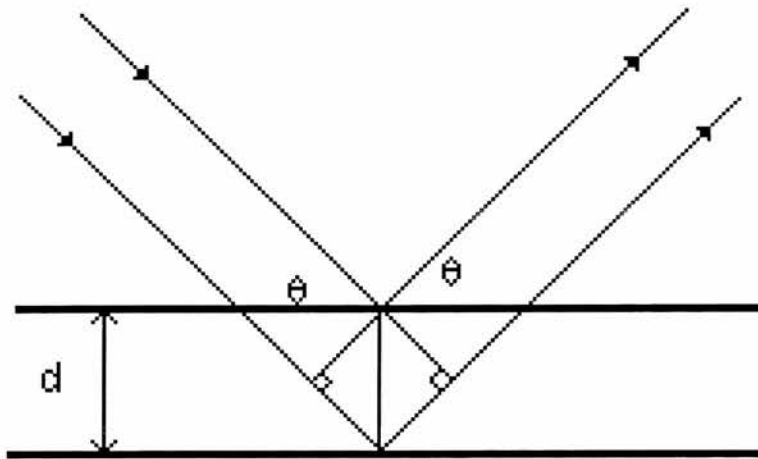


Fig.2.1: Derivation of Bragg's law

In the treatment used by Bragg, the crystal planes are treated as semi-transparent mirrors. Whilst this is not the true process, the results hold non-the less. The model considers that some of the x-rays are reflected from each plane and some pass through to reflect from subsequent planes. The reflected intensity from the many planes will then interfere either constructively or more likely destructively. Constructive interference will occur when the path difference between the reflected

beams is an integer number of wavelengths. Thus, from fig. 2.1, for two planes of interplanar spacing  $d$  upon which there is radiation incident with an angle  $\theta$ , the path difference will be  $2d\sin\theta$  and thus the condition for constructive interference will be:

$$n\lambda=2d\sin\theta$$

Where  $n$  is an integer and  $\lambda$  is the wavelength of the incident radiation. Due to the large number of varying planes in most crystals, if the path difference varies even by a fraction of a degree then the intensity of the reflection is virtually negligible due to deconstructive interference. By convention,  $n$  is taken as equal to 1, whilst assigning different Miller indices to high-order peaks such that they are equivalent to first order scattering from subsequent equivalent planes of Miller indices  $(nh, nk, nl)$ . Although this treatment works quite well and gives a good, simple picture, it is over simplified and it is useful to consider a full treatment.

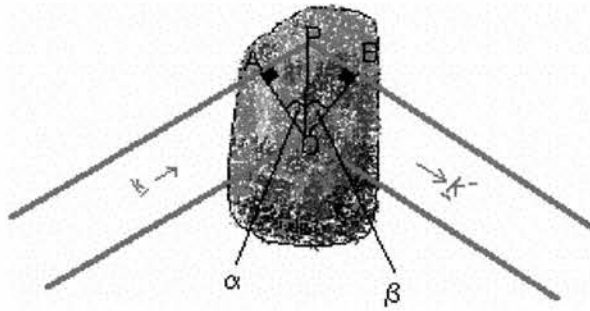


Fig.2.2: The diffraction of x-rays from a crystalline sample

The rate of scattering  $\propto \rho(r)dV$ , where  $\rho(r)$  is the electron density in the infinitesimal volume  $dV$  at point P.

The total scattered amplitude is the sum of all scattering contributions taking into account the relative phases.

The phase factor for element  $dV$  at P is

$$(2\pi / \lambda)\{AP + PB\}$$

From geometry,  $AP = OP \sin \alpha = \underline{k} \cdot \underline{r} / |k|$  and similarly for  $PB = -\underline{k}' \cdot \underline{r} / |k'|$ .

For elastic scattering,

$$|k| = |k'| = 2\pi / \lambda$$

Thus the phase factor is:

$$(2\pi / \lambda) \{ \underline{k} \cdot \underline{r} - \underline{k}' \cdot \underline{r} \} / |\underline{k}| = (\underline{k} - \underline{k}') \cdot \underline{r} = \underline{K} \cdot \underline{r}$$

Therefore, the total scattered amplitude from an infinitesimal point in an atoms electron cloud is

$$f(\underline{k}) = \int n(\underline{r}) e^{i\underline{K} \cdot \underline{r}} dV$$

However, scattering comes from all points in the electron cloud so if the integral is over an atom then this becomes the atomic scattering factor.

To find the total scattered amplitude from a unit cell, it is necessary to sum all the contributions from all of the atoms in the unit cell.

Thus total amplitude scattered from a unit cell is:

$$F(\underline{K}) = \sum_{j \text{ atoms}} f_j(\underline{K}) e^{i\underline{K} \cdot \underline{r}_j}$$

Thus, it follows that the total scattered amplitude from the sample is:

$$\Psi(\underline{K}) = \sum_{\text{nunitcells}} F(\underline{K}) e^{i\underline{K} \cdot \underline{T}_n}$$

Where  $\underline{T} = u_1 \underline{a}_1 + u_2 \underline{a}_2 + u_3 \underline{a}_3$

$\underline{a}_i$  represents the unit lattice vector in real space

$u_i$  represents the magnitude of the atomic position vector

For n large, this is a maximum for  $\underline{K} \cdot \underline{T}_n = 2\pi m$ ,  $m \in \text{set of integers}$

In reciprocal space, the reciprocal lattice vector is

$$\underline{G} = h\underline{b}_1 + k\underline{b}_2 + l\underline{b}_3$$

Where h, k and l are the Miller indices and  $\underline{b}_i$  represents the unit reciprocal lattice vectors  $\underline{b}_i = 2\pi \underline{a}_j \wedge \underline{a}_k / [\underline{a}_1 \underline{a}_2 \underline{a}_3]$ .

$$\underline{a}_i \cdot \underline{b}_j = 2\pi \delta_{ij}$$

Therefore,  $\underline{T} \cdot \underline{G} = 2\pi (u_1 v_1 + u_2 v_2 + u_3 v_3) = 2\pi p$ ,  $p \in \text{set of integers}$

Thus the total scattered amplitude is a maximum for  $\underline{K} = \underline{G}$

This condition is equivalent to the Bragg law discussed previously, since

$$|\underline{K}| = 2|k|\sin\theta = 4\pi\sin\theta/\lambda \text{ and } |\underline{G}| = 2\pi/d_{hkl},$$

Thereby considering that  $\underline{K}=\underline{G} \Rightarrow |\underline{K}|=|\underline{G}| \Rightarrow \lambda=2d_{hkl}\sin\theta$

Thus with  $\underline{r}_j = x_j\underline{a}_1 + y_j\underline{a}_2 + z_j\underline{a}_3$

The structure factor for the unit cell is

$$F(\underline{G}) = \sum_j f_j(\underline{G}) \exp\left[2\pi i(hx_j + ky_j + lz_j)\right] \quad (*)$$

By solving the set of equations (\*), atomic positions can be calculated.

However, the structure factor is not a directly observable quantity so its determination must be via its relation to the intensity of each reflection, which is thus:

$$I_{hkl} \propto sLp |F_{hkl}|^2$$

Where  $s$  is a scale factor,  $L$  is the Lorentz correction and  $p$  is the polarisation correction.

The Lorentz term is a consequence of the fact that different reciprocal lattice points require varying times to cross the sphere of reflection depending on their position in reciprocal space and the velocity with which it moves through the sphere. This correction is more significant in powder as opposed to single crystal experiments and depends also on the instrument used. The polarisation term is due to differences in the scattering of the electronic vector parallel to the reflecting plane compared to that perpendicular to it. These two terms are generally combined and for powder diffraction using Debye-Scherrer geometry with a cylindrical sample takes the form:

$$L_p = \frac{1}{2}(1 + \cos^2 2\theta)(\sin \theta \sin 2\theta)^{-1}$$

The effect of this term is to reduce the intensity of the diffraction maxima at intermediate angles relative to those in the forward and backward directions.

However, there are also other phenomena that affect the intensity of Bragg peaks. Absorption of the diffracted radiation can lead to a loss of intensity. The amount of absorption is dependent on the geometry of the experiment, the scattering angle  $\theta$ , the thickness and composition of the sample. Since absorption is also dependent on atomic number, it is more

of a problem when heavy atoms are present in the sample. In addition to absorption, the extinction effect can also influence the diffracted intensity.

Extinction arises from an almost perfect crystal in which instead of order extending throughout the crystal, the crystal consists of tiny domains, each varying slightly in orientation from its neighbours. Another effect, secondary extinction, results from reflection of a significant proportion of the incident beam from the surface planes, thus reducing the intensity of the beam incident on the deeper planes. Both of these effects are lessened when the sample under consideration is a finely ground powder since this leads to smaller "domains" which reduces the number of multiple reflections from each block as well as lessening the shielding effect. However, the most significant deviation of the expected diffracted intensity is due to preferred orientation.

Preferred orientation is the effect of a tendency of the small single crystals, of which powder consist, to lie in certain directions thus invalidating the assumption that all of the crystallites in the powder are lying in an equal distribution of randomly oriented directions. This leads to the distortion of the ratios of scattering from various planes. The effect is more pronounced in needle or disc like crystals. This distortion can be compensated for during refinement by use of a mathematical correction such as that of March-Dollase<sup>7</sup>.

So, with the use of mathematical corrections for the intensity values, the positions of the atoms within the unit cell may be found by solving a set of equations similar to (\*). However, it should be noted that the observable quantity is the intensity of the reflection. Thus, although the magnitude of the structure factor can be determined, its phase cannot and this will be discussed later.

## **Section 2.2: Instrumentation and Structure Solution Techniques**

From this treatment, it can be seen that collection of single crystal data is fairly straightforward. A four circle geometry is used whereby the crystal can be rotated through Euler's angles,  $\Phi$ ,  $\Theta$  and  $X$ , to bring a desired plane into a position that leads to constructive interference. Thus, by sweeping a counter through the fourth plane of freedom,  $2\theta$  or through the use of an image-plate or CCD stationary detectors, the data can be collected. This, in most cases, allows unambiguous determination of the magnitudes of the individual reflections. However, in powder diffraction where the sample contains many randomly oriented crystallites, it is impossible to arrange for only chosen planes to be in a reflecting position at any one time. For a given set of crystal planes, only those oriented at certain angles,  $\theta$ , with respect to the incident beam will give rise to diffraction. However, since all azimuthal angles are present in the sample, cones of radiation are produced whose axis co-incides with the

incident beam. These data may be collected using one of many methods. The method utilised in the majority of this work, the diffractometer method may be used wherein a detector is swept in an arc around the sample, thus allowing easy intensity collection.

Usually, the initial structural information is obtained from the positions of the peaks in the powder diffraction pattern. These peaks are indicative of the angle at which the diffracted x-rays undergo reinforcement, i.e. when the Bragg condition, eqn. 2.3, is satisfied. The values of two theta at which these peaks occur as well as which peaks are missing depend on the size and shape of the unit cell, i.e. the repeat pattern that is replicated many times to form the crystal. It is also dependent on the symmetry operations used to fill the unit cell and hence the crystal lattice. Thus, examination of the position and presence/absence of the peaks in diffracted intensity can determine the unit cell's size, shape and symmetry group. The peak positions in this work were determined using a computerised peak search package with manual adjustments.

Having determined the values of  $\theta$  at which diffraction maxima are observed, the reciprocal lattice parameters can be determined using the relation:

$$4\lambda^{-2}\sin^2\theta = d^{-2} = h^2a^{*2} + k^2b^{*2} + l^2c^{*2} +$$

$$2hka^*b^*\cos\gamma^* + 2hla^*c^*\cos\beta^* + 2klb^*c^*\cos\alpha^*$$

The solution of the set of the above equations and determination of the lattice parameters were carried out using auto-indexing programs such as TREOR<sup>8</sup> or VISSER<sup>9</sup>. These programs generate a number of solutions that can then be ranked in terms of the de Wolff figure of merit<sup>10</sup>:

$$M_{20} = 2Q_{20}^{-1} \varepsilon N_{20}$$

Where  $Q_{20}$  is the value of  $d^{-2}$  for the 20<sup>th</sup> indexed line,  $N_{20}$  is the number of different calculated Q values up to  $Q_{20}$  and  $\varepsilon$  is the average difference between the calculated and observed line positions. This thereby provides a ratio of the Q space covered by observed lines to the number of possible lines in the same space. Using this grading system, a best-fit unit cell may be determined.

However, size and shape are not the only intrinsic structural properties that can be determined. In addition, every lattice has associated with it a set of symmetry operators that can map a basis point onto an equivalent basis point. As a result of some of these symmetry operations, some of the atoms in one motif may be positioned such that they scatter exactly out of phase with the atoms in another. This leads to systematic

absences of diffraction peaks from the pattern. By consideration of which peaks are absent, the symmetry elements of the lattice may be determined and classified into one of a fixed number of space-groups, which describe the symmetry of the crystal<sup>11</sup>. Having determined the size, shape and symmetry elements of the crystal, traditionally, the next step is to try and obtain an approximate electron density map.

At this point there are two ways of proceeding depending on which structure solution method is to be followed. The most common route is to use procedures such as Direct Methods<sup>12</sup>, Patterson maps<sup>13</sup>, maximum entropy and likelihood ranking<sup>14</sup> or certain variations of Monte-Carlo<sup>15</sup> or genetic algorithms<sup>16</sup>. With these methods, it is first required to extract the intensities of individual reflections. This presents a problem in powder diffraction data in that, since the 3 dimensional information of single crystal techniques is compressed into 1 dimension for powders, there is a resultant increase in the overlap of reflections. Overlap in reflections arise as a result of symmetry in the crystal. It is possible to extract the integrated intensity of individual reflections through the use of a pattern deconvolution method such as those proposed by LeBail<sup>17</sup> or Pawley<sup>18</sup>. The LeBail method is generally used since it is more computationally efficient in addition to giving inherently positive intensities.

The LeBail method relies on a modification of the Rietveld procedure. In the Rietveld method, atomic co-ordinates are refined using a least squares technique which compares observed intensities with those calculated from the structural model. In contrast, the LeBail fitting procedure assigns starting values of individual intensities by positioning a dummy atom in the cell before recalculating them at the end of each cycle in which unit cell dimensions, zero-point error and profile parameters are refined. In the Pawley method, integrated intensities are used as independent variables in the least-squares refinement. However, these processes cannot extract accurate individual intensities, especially if there are peaks with significant overlap, e.g. their interpeak distance is less than half of the peak halfwidth. This is a fundamental limitation of techniques that rely upon this information.

Once the integrated intensities of the individual reflections have been extracted, the crucial step in the structure solution procedure is to overcome the phase problem.

Extending the theoretical treatment of diffraction from crystals mentioned earlier, it can be shown that the electron density at a point can be given by the relation

$$\rho(\underline{r}) = \frac{1}{V} \sum_{\underline{G}} F(\underline{G}) \exp(-2\pi i \underline{G} \cdot \underline{r}_j)$$

Therefore, if the structure factors are known, the electron density,  $\rho(r)$ , at any point in the unit cell may be calculated from which it is possible to determine atomic positions. However, since only the modulus, i.e. the magnitude, of the structure factor is determinable from diffraction intensity and not the phase, some form of guess must be made as to the phase of each of the structure factors. There are several methods for approximating phases, including Direct Methods, Patterson maps and genetic algorithms amongst others.

The Direct Methods technique is underpinned by the use of probabilistic relationships between the extracted integrated intensities and their phases. Another tenet of Direct Methods is the approach used to combat the intensity fall off problem. The intensity fall off problem arises from the fact that the scattering of an atom is the sum of the scattering from all points in its electron cloud. Thus, due to interference between x-rays which have been scattered from different point in the electron cloud, the diffracted intensity falls off as a function of  $\sin(\theta/\lambda)$ .

However, this effect can be overcome through the use of either unitary or normalised structure factors,

The unitary structure factor is given by:

$$|U_H| = |F_H| / \sum f_j$$

This is an analogue of the structure factor  $|F_H|$  but has an absolute value which ranges between 0 and 1. This is equivalent to a structure factor corresponding to an idealised point atom and is thus independent of the scattering angle. Similarly, the normalised structure factor may be used,

$$|E_H| = |F_H| / \sqrt{\varepsilon \sum f_j^2}$$

Where  $\varepsilon$  belongs to the set of integers and depends on the space group of the system. This normalisation of the structure factor diminishes the effect of peaks that have an unusually large intensity due to symmetry considerations.

After normalisation, the determination of phases is usually based upon the Sayre probability relationship<sup>19</sup>:

$$S(hkl) \sim S(h'k'l').S(h-h',k-k',l-l')$$

For a centrosymmetric structure,  $S(hkl)$  is the sign of  $E_{hkl}$ . The probability that this relationship holds,  $P$ , is dependant on  $|E_{hkl}|$  in the following manner:

$$P = \frac{1}{2} + \frac{1}{2} \tanh\{N^{-1}|E_{hkl} \cdot E_{h'k'l'} \cdot E_{-h', -k', -l'}|\}$$

Thus it can be seen that the probability of the relationship holding is a function of the number of atoms in the unit cell,  $N$ , and the average value of  $|E|$  in the triple product. Thus by selecting a basis of reflections with large values of  $|E|$ , assigning three of the reflections as positive, a group of possible starting sets can be obtained with each set containing a different combination of the remaining phases (+ve or -ve). It is generally accepted that a target of roughly ten  $|E|$  values per atom is required for successful further refinement. Thus, it would be usual to take the  $10N$  largest  $|E|$  values and try to generate phases for them using all the possible starting sets. However, since some of the  $|E|$  values will be very small, many of the phase estimates will be incorrect. The most self-consistent model can then be used to generate an electron density map by converting the normalised structure factors back into structure factors using the relationship:

$$\rho(xyz) = V^{-1} \sum_h \sum_k \sum_l E_{hkl} \cos 2\pi(hx+ky+lz)$$

Thereby the atomic co-ordinates can be deduced and in turn used in a refinement process such as Fourier analysis or Rietveld refinement.

The Direct Methods technique tends to work well for structures in which all the atoms have similar x-ray scattering powers and there is a more or less random distribution of atoms within the cell. However, for other systems, where there is an atom which is a dominant scatterer, the Patterson method is usually more effective.

The Patterson method circumvents the phase problem through multiplication of both sides of the structure factor equation by its complex conjugate to yield an expression in terms of  $|F_{hkl}|^2$ :

$$|F_{hkl}|^2 = \sum_i \sum_j f_i f_j \exp[2i(\mathbf{r}_i - \mathbf{r}_j) \cdot \mathbf{h}]$$

The fundamental concept of this method is to then use this term for  $|F_{hkl}|^2$  in the electron density equation instead of  $|F_{hkl}|$ , thus yielding a form of three dimensional electron density map but with peaks corresponding to interatomic vectors, rather than atomic positions. The height of the peak will be proportional to the product of the two atomic numbers. Therefore the most distinguishable vectors will be those between two heavy atoms. Once the heavy atoms have been located, the partial structure factors

considering only the heavy atoms can then be calculated, which although perhaps differing markedly in magnitude are likely to be of the same phase. Thus these phases can be substituted into the equation for electron density, along with the extracted  $|F_{hkl}|$  values in order to find the lighter atom positions thereby providing data suitable for structure refinement.

These techniques have been used successfully to solve the structure of many compounds from powder data such as  $\text{Nd}(\text{OH})_2\text{NO}_3 \cdot \text{H}_2\text{O}$ <sup>20</sup> and  $\text{Ga}_2(\text{HPO}_3)_3 \cdot 4\text{H}_2\text{O}$ <sup>21</sup>. However, techniques that rely on extracted intensity information are fundamentally limited due to the necessity of educated speculation as to the actual magnitude of overlapped reflections coupled to further uncertainty in the determination of phases. Despite this, many novel methods have been used to minimise these problems, especially in experimental methods such as using asymmetric thermal expansion to separate reflections by collecting two patterns at disparate temperatures and analysing how the peak positions in the diffracted intensity change<sup>22</sup>. Furthermore, advances in synchrotron radiation are increasingly leading to higher and higher resolution<sup>23</sup>. However, a different approach has also been developed concurrently with these instrumental improvements.

These approaches completely bypass the overlap and phase problems by employing a modified Rietveld full profile fitting procedure that allows

location of a global minimum in fit from a completely random starting configuration. A variety of methods have been used for this purpose including Monte-Carlo and genetic algorithms, however, the main technique used in the work presented in this thesis is that of simulated annealing and this is detailed further in chapter 4. However, in general, these techniques all rely on creating a random starting model that is then used to generate a calculated diffraction pattern which can be compared to the experimental diffraction pattern using a type of goodness-of-fit-function. Some form of variation, containing a random component, of the model is then made before recalculation of the simulated diffracted pattern is made. Some form of model selection then takes place-involving comparisons of the goodness of fit of each model. This process is then repeated until either the routine converges to a solution or a set number of iterations is made and the model with the best fit of calculated to experimental diffraction patterns is then selected for refinement. Thus, these techniques may be used in cases where extraction of integrated intensities is abstruse due to peak overlap or phase assignment is hindered by factors such as the unfavourable combination or distribution of atoms. However, they are generally less computationally efficient due to the vastly greater time required to compute a full diffraction profile compared to that spent carrying out each phase assignment step. Despite this, there have been several features made possible by full-profile methods that can substantially reduce the computational time such

as constraining bond lengths and angles in molecular structures to only feasible values and assigning the same value to equivalent bond lengths or angles. Thus there is a wealth of techniques available for structure solution from powder diffraction data, however, these methods usually give only approximate structural models. For accurate determination of crystallographic data, further refinement is required, usually involving full profile Rietveld refinement and/or difference Fourier analysis.

The development of the Rietveld method<sup>24</sup> in 1969 heralded the introduction of an easy method for the refinement of structural data from powder diffraction data. The technique relies on data collected in a step-wise fashion such that intensity is recorded in a finite interval of  $2\theta$  or  $d$ . The calculated profile is computed using the unit cell parameters and zero point correction to determine the positions of the Bragg peaks with the atomic positions and displacement parameters being used to determine the intensity of the peaks. The peaks are of a form described using a peak shape function with a background, either fixed or fitted, being used to complete the pattern. The intensity of the calculated profile at each point,  $Y_{ic}$  is compared with the corresponding observed point,  $Y_{io}$  for all  $i$  steps in the pattern. Thus, it is possible to refine the calculated model by carrying out a least squares refinement of a goodness of fit criterion such as:

$$S = \sum w_i |y_{io} - y_{ic}|^2$$

Where  $w_i$  is a weighting factor which is dependant on the standard deviations of intensity associated with the  $i$ -th profile point.

The process of refinement involves the variation of several parameters including the scale factor, background function, zero point correction, profile parameters, preferred orientation correction, lattice parameters, atomic positions and displacement factors.

The profile parameters are coefficients of a function used to simulate the shape of the diffraction peaks. There is a range of profile functions available depending on the peak shape required. However, the function used for all the work presented here is the pseudo-Voigt function<sup>25</sup> which is a linear combination of a Gaussian function and a Lorentzian function and provides good description of the peak. Thus, the peak shape function is defined as:

$$G_{ik} = \eta L + (1-\eta)G$$

Where  $\eta$  is a mixing coefficient that determines the proportion of Lorentzian to Gaussian character in the peak shape.  $L$  is the Lorentzian contribution:

$$L = \eta C_1^{1/2} \{ \pi H_k (1 + C_1 X_{ik}^2) \}^{-1}$$

And  $G$  is the Gaussian component:

$$G = C_0^{1/2} \pi^{-1/2} H_k^{-1} \exp(-C_0 X_{ik}^2)$$

Where  $C_0 = 4 \ln 2$ ,  $C_1 = 4$ ,  $X_{ik} = \Delta \theta_{ik} H_k^{-1}$  and  $H_k$  is the full width at half maximum, FWHM, of the  $k$ th Bragg reflection. However, the FWHM of a diffraction peak has an angular dependence that is defined in terms of a Gaussian and a Lorentzian component,  $H_{kG}$  and  $H_{kL}$ .

$$H_{kG} = (U \tan^2 \theta + V \tan \theta + W)^{1/2}$$

$$H_{kL} = X \tan \theta + Y \cos^{-1} \theta + Z$$

$$\text{And } H_k = (H_{kG}^5 + 2.69269 H_{kG}^4 H_{kL} + 2.42843 H_{kG}^3 H_{kL}^2 + 4.47163 H_{kG}^2 H_{kL}^3 + 0.07842 H_{kG} H_{kL}^4 + H_{kL}^5)^{0.2}$$

Furthermore, the mixing coefficient,  $\eta$ , can be described in terms of FWHM components:

$$\eta = 1.36603(H_{kL} H_k^{-1}) - 0.47719(H_{kL} H_k^{-1})^2 + 0.11116(H_{kL} H_k^{-1})^3$$

Thus it is possible to refine fully the peak shape using only the components of  $H_{kG}$  and  $H_{kL}$ , namely  $U, V, W, X, Y$  and  $Z$ . However, despite the flexibility of the pseudo-Voigt function, the peak shapes described by it are all symmetrical which is rarely the case in the experimental case due to instrumental and sample effects. Thus an extra term is needed to describe the asymmetry of the peak.

In addition to the peak shape function, another refineable parameter to be considered is the background. For most of the work carried out in this thesis, the background was described using a linear interpolation of points in the diffraction pattern which have no nearby Bragg peaks. However, it is also possible to describe the background using a  $\theta$  dependent mathematical function such as a power or cosine series that contains some refineable parameters. Further to the background considerations, the effect of preferred orientation must be accounted for.

Preferred orientation emanates from the tendency of crystals to lie in certain planes and has the effect of varying the relative intensities of certain reflections, thereby distorting the available data. Using a spinning capillary filled with loose packed powder may lessen this effect since the crystallites are constantly being reoriented with respect to the beam. Despite this, in some cases the effect is still significant and must be compensated for during the refinement process using a mathematical

correction. The correction used in the work presented here is the March-Dollase function<sup>32</sup>. This involves modifying the extracted intensities in the following fashion:

$$I_{k \text{ corrected}} = I_k P_k$$

$$\text{Where } P_k = [R_o^2 \cos^2 \alpha + \sin^2(\alpha R_o^{-1})]^{-3/2}$$

$R_o$  is a refinable variable representing the effective compression or extension of the sample along the cylinder axis as a result of preferred orientation and  $\alpha$  is the acute angle between the preferred orientation axis and the diffracting plane. However, preferred orientation is not the only phenomenon to affect the diffraction pattern.

Earlier, we assumed that atoms were spherical and that the contribution to diffraction from each atom depended only on the size of its electron cloud (and thus its atomic number) and the fall off of scattering power due to interference between x-rays diffracted from different parts of the atom. However, thermal motions or static random displacements of the atoms also affect the scattering by effectively broadening the electron cloud. It can be shown that for isotropic vibrations, the effect is to modify the atomic scattering factor in the following fashion:

$$f_{corrected} = f e^{-B(\sin^2\theta)/\lambda^2}$$

Where  $B$  is a function of the mean squared amplitude of the atomic vibration,  $\bar{u}^2$ :

$$B = 8\pi^2 \bar{u}^2$$

Thus a correction can be made in the refinement to allow for this with either the value of  $B$  or  $u$  for each atom being refined. It is also possible to describe the displacements as an ellipsoid rather than a sphere. Having considered the parameters to be refined, it is prudent to examine the method by which the parameters are refined.

The refinement process itself involves the minimisation of a quality of fit term,  $S$ , defined by:

$$S = \sum w_i (Y_{io} - Y_{ic})^2$$

Where  $w_i$  is a weight assigned to each measured  $i$ -th intensity, which is based on the standard deviations associated with the interval. This is then refined using a least squares method such as the Newton-Raphson method. The quality of the final model is judged using the quality of the fit of calculated to observed patterns. There are several subtly varying

criteria for this assessment. The most useful are the weighted R-factor and the goodness of fit,  $\chi^2$  since these terms include  $S$ , the term being minimised.

$$R_{wp} = [S/(\sum W_i Y_{io}^2)]^{1/2}$$

$$\chi^2 = S/(N-P)$$

Where  $N$  is the number of profile points and  $P$  is the number of parameters. In all of these cases, the lower the value the better the fit, with  $\chi^2$  having an ideal perfect value of unity.

Thus, the actual refinement process involves the least squares minimisation of  $\chi^2$  through variation of the atomic co-ordinates, displacement factors, profile parameters, background function, asymmetry, preferred orientation parameter(s), extinction coefficients and scale factor. The least squares process itself can take several forms such as the Newton-Raphson method, the Gauss-Newton method or variable metric method, which are all variations of the same principle. This involves calculating gradients of the  $\chi^2$  function and trying to solve for the gradient being zero, i.e. to find a set of parameters corresponding to the minimum of  $\chi^2$ . Since all the methods are basically similar, only the Newton-Raphson method is included here as an example.

The goodness-of-fit function,  $\chi^2$ , can be expressed as follows:

$$\chi^2 = \sum_{i=1}^N \{ [Y_{io} - Y_{ic}] / \sigma(Y_{io}) \}^2$$

For N observed points.

This is a minimum when the rate of change of  $\chi^2$  with parameter variation is zero. i.e. for M parameters  $p_k$ , the local minimum in  $\chi^2$  is when:

$$\partial \chi^2 / \partial p_k = 0 = -2 \sum_{i=1}^N \{ [Y_{io} - Y_{ic}] / \sigma(Y_{io}) \} \partial y_{ic} / \partial p_k = f_k$$

Thus we have a series of M non-linear equations which have to be solved. This can be done by means of a Taylor series expansion in the neighbourhood of the root, i.e.:

$$f_k(\bar{p} + \delta \bar{p}) = f_k(\bar{p}) + \sum_{j=1}^M \frac{\partial f_k}{\partial p_j} \delta p_j + \text{higher order terms}$$

where  $p$  is the parameter set,  $\begin{pmatrix} p_1 \\ p_2 \\ \vdots \\ p_M \end{pmatrix}$

From the minimum condition, in the neighbourhood of a root:

$$f_k(p + \delta p) = 0 \Rightarrow f_k(p) + \sum_{j=1}^M [\partial f_k / \partial p_j] \delta p_j = 0 \quad (**)$$

Where  $\partial f_k / \partial p_j$  can be calculated using:

$$\frac{\partial f_k}{\partial p_j} = \frac{\partial^2 \chi^2}{\partial p_k \partial p_j} = 2 \sum_{i=1}^N \frac{1}{\sigma^2(y_i^e)} \left[ \frac{\partial y_i^c}{\partial p_k} \frac{\partial y_i^c}{\partial p_j} - (y_i^e - y_i^c) \frac{\partial^2 y_i^c}{\partial p_k \partial p_j} \right]$$

The set of equations, (\*\*), is then solved for all  $\delta p_i$ , the parameter increments towards the nearest minimum of  $\chi^2$ . After that, a new set of variable parameter values  $p_{new}$  is obtained with  $p_{new} = p + \delta p$  and the process re-iterates until the minimum is reached.

Using these methods, precise crystallographic structures can be obtained which in turn can yield useful information such as bond lengths, bond angles, torsion angles and atomic co-ordination. As explained in the start of this chapter, this information is of great interest in the field of ionically conducting polymer salt compounds and over the years, there has been considerable application of these methods to the field.

### **Section 2.3: Application of Structure Solution using X-Ray Diffraction to the Study of Ionically Conducting Polymer:Salt Complexes**

The structure solution of polymer:salt complexes has seen a great evolution since the first work was reported in the field by Tadokoro et al. in 1968<sup>26</sup>. The evolution has seen significant change and innovation in

both sample preparation and the techniques used in the structural solution process.

Crystal structural determination of polymer/salt complexes with potential as ionically conducting materials has been carried out exclusively on complexes of the archetypal ionically conducting polymer, PEO. The first work to this end was carried out on PEO:Mercuric Chloride complexes by Tadokoro and co-workers, the first compound to be determined being  $\text{PEO}_4:\text{HgCl}_2$ <sup>26</sup>.

### **Section 2.3.1: $\text{PEO}_4:\text{HgCl}_2$ <sup>26</sup>**

Crystalline fibres of  $\text{PEO}_4:\text{HgCl}_2$  were produced by soaking PEO fibres in a saturated solution of mercuric chloride for a week at room temperature. Fibre diffraction, a variation of the single crystal method, was carried out. The data used in this is of poor quality but despite this, an orthorhombic unit cell  $a=13.55\text{\AA}$ ,  $b=8.58\text{\AA}$  and a fibre axis of  $c=11.75\text{\AA}$  could still be deduced. There was a certain amount of ambiguity surrounding the spacegroup but the refinement was carried out in Ccmm. Paterson methods were used to locate the Hg and Cl atoms. Whilst this method was of use in determining the positions of the heavy atoms, the large absorption and scattering of these atoms meant that it was impossible to determine the position of the atomic constituents of the PEO chain. This was instead determined by trying to fit a chain into the remaining space in

the unit cell with the condition that it had to be continuous at the unit cell edges. This was confirmed using a Fourier projection that was derived from powder x-ray diffraction data. The PEO conformation obtained was a very unusual  $t_5gt_5\bar{g}$  arrangement, with all C-O bonds trans and C-C bonds taking up gauche, anti-gauche or trans conformations. In addition, both the cation and the anions lay external to the chain and were not wrapped around. However, it must be stressed again that this early data is of relatively poor quality and there are further complications imposed by the adsorption and dominant scattering of the Hg atom. Still, whilst investigating the  $\text{PEO}_4:\text{HgCl}_2$  compound, it was found that if the fibres of  $\text{PEO}_4:\text{HgCl}_2$  were either left soaking in saturated  $\text{HgCl}_2$  solution for a year or soaked in boiling  $\text{HgCl}_2$  solution for two days before being rolled, then another complex of composition  $\text{PEO}_1:\text{HgCl}_2$  is produced.

### **Section 2.3.2: $\text{PEO}:\text{HgCl}_2$ <sup>27</sup>**

Once again, information obtained from fibre diffraction was used as a basis in the structure solution process. This yielded an orthorhombic cell of  $a=7.75\text{\AA}$ ,  $b=12.09\text{\AA}$  and a chain axis of  $c=5.88\text{\AA}$ . The space group was determined through systematic absences to be either  $\text{Pn}cm$  or  $\text{P}nc2$ . The position of the mercuric chloride molecule was determined via the Paterson method. In contrast to the previous case, in which the chain in the  $\text{PEO}_4:\text{HgCl}_2$  system was placed using human judgement based on available space, far-infrared IR spectroscopy was used to help determine

the conformation of the chain in addition to human judgement, consideration of remaining space in the cell and assumptions including that the co-ordination of the mercury by the PEO was similar to the 4:1 case. Using these considerations, a PEO chain conformation of  $tg_2t\bar{g}_2$  was determined, with all C-C bonds being gauche or anti-gauche and the C-O bonds lying in either the gauche, anti-gauche or trans conformation. This corresponds to a stretched “zigzag” chain and is in marked contrast to the more helical chain of pure PEO. The cations are not enveloped by the chain and are co-ordinated by two ether oxygens. There also appears to be ionic cross-links formed by O-Hg-Cl-Hg-O’ associations where O and O’ belong to different PEO chains. This could have the effect of raising the melting point of the compound and suppressing the conduction mechanism. It was pointed out that the widely held theory of conduction, namely that ions were conducted down tunnels or some form of helices of PEO was incompatible with the structural picture given by these two mercuric chloride compounds. This was due to the fact that the PEO chain does not form any sort of tunnel structure and does not enclose the cation. However, multivalents are known as having poorer conductivity than the alkali metal analogues. This lack of tunnel structure may be as a result of the large cation size or the salt concentrations studied. Clearly further investigation is required. To further complete the picture, some alkali metal complexes were studied by Chatani et al.<sup>28</sup>

### Section 2.3.3: PEO<sub>3</sub>:NaI<sup>28</sup>

This compound was a landmark in that it was the first alkali metal containing conducting polymer structure to be solved. As with the previously solved structures, the samples used were uniaxially oriented fibres, in this case, created using a hot drawing process. Using the fibre diffraction data obtained from these samples, a monoclinic unit cell was obtained for the compound with a chain axis of 7.98Å. The I<sup>-</sup> position was located by using an un-named technique involving extracted intensities whilst the Na<sup>+</sup> ion was placed using a trial and error method. Similarly the PEO chain was determined using human judgement based on the remaining space in the unit cell, space group considerations, chain continuity and a conformation which was known from the infra-red and Raman spectroscopic studies of Papke et al<sup>29,30</sup>. The chain was found to be helical with all C-O bonds trans and all C-C bonds alternating between gauche and anti-gauche. Both the cations and ions lay within the PEO helix with the anions being bridged by the cations, forming a zigzag arrangement. The cation was 5 co-ordinated by two I<sup>-</sup> anions and three ether oxygens which all belonged to the same chain. Thus the compound was found to be a one dimensional complex with each PEO chain being associated with a dedicated set of anions and cations, no ionic cross-linking was visible. Clearly this model is more consistent with the picture proposed by many of the early theorists of the cation being enclosed by some form of polymer "tunnel"<sup>31,32</sup>. However, the close co-ordination of

the cations probably means that any conduction process would have to involve the making and breaking of these co-ordinating bonds which would in turn probably involve some rearrangement of the cations co-ordinating sphere such as by segmental motion of the chain. However, clearly more investigation is needed into the effects of cation type, salt concentration and anion type. The latter of these was explored further by Chatani following the structure determination of  $\text{PEO}_3:\text{NaSCN}$ <sup>33</sup>.

#### **Section 2.3.4: $\text{PEO}_3:\text{NaSCN}$ <sup>23</sup>**

Again, the structure of this compound was determined from fibre diffraction data. The unit cell was found to be monoclinic with a chain axis of 7.19Å. This is of a similar magnitude to that in  $\text{PEO}_3:\text{NaI}$  so the structure of  $\text{PEO}_3:\text{NaSCN}$  was determined from a starting model based on that of the NaI analogue through a combination of Rietveld refinement and trial and error. Thus unsurprisingly, the chain was found to take up a similar double helical  $t_2gt_2gt_2\bar{g}$  conformation with all C-O bonds trans and all C-C bonds gauche or anti-gauche. However, one surprising difference is the co-ordination number of the sodium, being six, rather than five as in the case of  $\text{PEO}_3:\text{NaI}$ . Four ether oxygens and two nitrogens from the thiocyanate groups co-ordinate the sodium. Despite the fact that the thiocyanate anion is larger than iodide, the anions still lie stacked along the chain axis and are associated with one chain only and there is thus no

ionic cross-linking between the chains. However, this is in marked contrast to the case in PEO:NaSCN<sup>33</sup>.

### Section 2.3.5: PEO:NaSCN<sup>33</sup>

The samples used in this structure determination were prepared by soaking a PEO fibre that had been placed under tension in a concentrated sodium thiocyanate solution. As in the previous cases, fibre diffraction was used in the structure solution process. A monoclinic unit cell was determined which contained a possible chain axis of 5.83Å which is comparable to that found in PEO:HgCl<sub>2</sub>. Thus, structure solution was effected using a trial and error method based on the PEO:HgCl<sub>2</sub> structure as well as space group and unit cell size considerations. The PEO chain was found to take up a  $tg_2t\bar{g}_2$  stretched zigzag conformation similar to that of PEO:HgCl<sub>2</sub>. This is in contrast to the helical chain in PEO<sub>3</sub>:NaSCN and would perhaps indicate that the chain conformation is more a property of the salt concentration rather than the salt species. However, as in PEO<sub>3</sub>:NaSCN, the sodium is six co-ordinated although in this case, the sodium co-ordination sphere consists of only two ether oxygens as well as two nitrogen atoms and two sulphur atoms from the anion. A feature of this co-ordination is the sharing of a thiocyanate group by two sodium atoms, each being associated with a different PEO chain. This results in an ionically cross-linked three dimensional network which could

retard the freedom of the PEO chain to undergo segmental motion and also raise the melting point. The compounds solved so far present an interesting insight into some of the basic structural properties and patterns of ionically conducting polymer/salt complexes. However, one of the main hindrances to widespread structure solution in this field is the difficulty in obtaining single crystals of sufficient quality. It is to this end that further work was carried out exploring the use of powder x-ray diffraction data as a basis in the determination of these solid electrolyte structures.

#### **Section 2.3.6: PEO<sub>3</sub>:NaClO<sub>4</sub><sup>34</sup>**

The structure of PEO<sub>3</sub>:NaClO<sub>4</sub> was solved from high quality powder x-ray diffraction data obtained from a laboratory x-ray diffractometer using a sample prepared using the cryogrinding method. The unit cell was determined to be monoclinic with a possible chain axis of 8.355Å which is similar to the chain axis length of 7.98Å of PEO<sub>3</sub>:NaI. Thus, the structure was derived through Rietveld refinement of a model based on the PEO<sub>3</sub>:NaI structure with a Cl<sup>-</sup> anion initially residing on the I<sup>-</sup> position. Soft constraints were used in order to achieve a chemically sensible model. An excellent fit was obtained after refinement, with agreement factors of  $R_{wp}=6.9\%$  and  $\chi^2=1.95$ . The PEO chain conformation was unsurprisingly similar to that of previously solved PEO<sub>3</sub>:salt compounds in that all C-C bonds were gauche or anti-gauche and all C-O bonds trans, resulting in a

helical  $t_2gt_2gt_2\bar{g}$  formation. This helical chain wrapped the sodium cations in such a way as to co-ordinate the cation through three ether oxygens, the five-fold co-ordination being completed by two perchlorate oxygens. As in PEO<sub>3</sub>:NaI, the anions bridge neighbouring cations and are associated with only one PEO chain. Thus there is no evidence of any ionic crosslinking. The stretching of the PEO helix along its axis and also the greater separation of the helices relative to those in PEO<sub>3</sub>:NaI provides greater free space in the material which could be a factor in the relatively high conductivity of perchlorate based systems. However, the materials studied so far tend not to be those most used or studied by other methods and clearly further work on these is needed.

### **Section 2.3.7: PEO<sub>3</sub>:LiCF<sub>3</sub>SO<sub>3</sub><sup>35</sup>**

The archetypal polymer electrolyte, LiCF<sub>3</sub>SO<sub>3</sub> solvated in PEO, is a widely studied system, both in terms of applications and fundamental research. Thus in terms of linking structural observations to results from other techniques as well as providing insights for technological improvements, the solution of the structure of a complex like PEO<sub>3</sub>:LiCF<sub>3</sub>SO<sub>3</sub> is pivotal. The unit cell was determined to be monoclinic of similar dimensions to that of PEO<sub>3</sub>:NaSCN. Thus the structural determination process involved Rietveld refinement of an initial model which was based on that obtained for PEO<sub>3</sub>:NaSCN with the use of soft constraints to bias the refinement towards the helical PEO conformation

typical of PEO<sub>3</sub>:salt compounds. In addition, difference Fourier techniques were employed in order to help determine the position of the CF<sub>3</sub>SO<sub>3</sub><sup>-</sup> moiety. Initially, the refinement was carried out using powder x-ray diffraction data obtained at a temperature of 100K to minimise thermal vibrations with the results later being used as a starting point in a refinement of room temperature data. At the end of all the refinements, the final fit to room temperature data was good, giving agreement indices of  $R_{wp}=3.84\%$  and  $\chi^2=1.83$ . The chain was found to take up the helical  $t_2gt_2gt_2\bar{g}$  conformation that allows the PEO chain to wrap around the cation. The lithium ion was found to be five co-ordinated by three oxygens from the chain and one oxygen from each of two individual triflate groups. As in previous 3:1 compounds, the anions span adjacent cations with two of the three oxygens on each triflate moiety being co-ordinated to a cation with the third oxygen being free. An observation that could have important consequences is that the -CF<sub>3</sub> group projects into the interchain space. If this trend were repeated in similar compounds then it would account for the difficulty of crystallisation and conductivity in compounds which have larger groups at this position such as PEO:Li[(CF<sub>3</sub>SO<sub>2</sub>)<sub>2</sub>N] and PEO:Li[(CF<sub>3</sub>SO<sub>2</sub>)<sub>3</sub>C]. In addition, it is again apparent that the chain conformation is largely a function of salt concentration. However, it is also clear that cation type could also be important with cations residing outside the chain in certain structures such as PEO<sub>1</sub>:NaSCN and PEO<sub>4</sub>:HgCl<sub>2</sub> but being wrapped inside a PEO helix

in some others such as  $\text{PEO}_3:\text{NaClO}_4$  and  $\text{PEO}_3:\text{LiCF}_3\text{SO}_3$ . To this end, further investigation of PEO:salt ratios differing to that of the widely investigated 3:1 is required in addition to an examination of the effect of cation size on structural properties.

### **Section 2.3.8: $\text{PEO}_4:\text{KSCN}$ , $\text{PEO}_4:\text{NH}_4\text{SCN}$ <sup>36</sup> and $\text{RbSCN}$ <sup>37</sup>**

The solution of these compounds would satisfy those avenues for further investigation. However, it would also present a considerable challenge since most of the previously solved compounds relied on the Rietveld refinement of a model based on the structure of an isostructural compound which had been solved using single crystal techniques. However, the only 4:1 compounds which had been attempted to be solved were those of  $\text{PEO}_4:\text{HgCl}_2$  and  $\text{PEO}_4:\text{RbSCN}$ , both solved from very poor quality single crystal diffraction data. Furthermore, it was clear that the models proposed for these compounds were incompatible with the unit cells determined from high quality powder diffraction data in these cases. In addition, attempts to solve the structures from starting models based on  $\text{PEO}_3$ :salt complexes were equally unsuccessful. Thus an ab-initio structure determination had to be carried out. Direct methods were employed to locate the sulphur atom in  $\text{PEO}_4:\text{NH}_4\text{SCN}$ . Difference Fourier techniques were then employed in order to locate the rest of the structure before the application of Rietveld refinement methods to give accurate atomic co-ordinates. The structures of  $\text{PEO}_4:\text{KSCN}$  and

PEO<sub>4</sub>:RbSCN were then determined by Rietveld refinement of the refined structural model of PEO<sub>4</sub>:NH<sub>4</sub>SCN.

The three complexes are nearly isostructural with small differences in chain size due to variances in the size of the cation. In all cases, the PEO chain adopts a helical arrangement that envelops the cation. However, unlike the helix of the 3:1 compounds, the helix is larger and adopts a  $t_2gt_2gt_2\bar{g}t_2\bar{g}$  conformation with all C-O bonds trans but the C-C bonds taking up a gauche or anti-gauche conformation. This is in marked contrast to the models proposed for PEO<sub>4</sub>:RbSCN by Hibma<sup>38</sup> or the structure proposed by Takodoro<sup>26</sup> for PEO<sub>4</sub>:HgCl<sub>2</sub>, which in both cases have PEO chains which are non-helical with cations external to the enclaves of the PEO chain. Thus, the doubt cast on ionic transport theories that involve some sort of ionic movement inside a co-ordinating polymer cylinder or helix as a result of these previous structural determinations has to be questioned. The larger helix also allows greater co-ordination of the cations with all three, Rb<sup>+</sup>, K<sup>+</sup> and NH<sub>4</sub><sup>+</sup> all being 7 co-ordinated by five ether oxygens, all from the same chain, and two nitrogens from the thiocyanate groups. It also shows that even cations as large as rubidium can be accommodated inside the PEO helix. Even with the larger helices and cations, there is still no ionic cross-linking evident, with all cations and anions being associated with no more than one chain. Despite the admirable structural solution performed in this case, solutions

from direct methods rely heavily on obtaining reliable extracted intensities and can be limited in use depending on the atomic distribution. Clearly a wider range of methods for use in ab-initio structure determinations is desirable.

### **Section 2.3.9: PEO<sub>3</sub>:LiN(SO<sub>2</sub>CF<sub>3</sub>)<sub>2</sub>**<sup>39</sup>

Interest in the structure of PEO<sub>3</sub>:LiN(SO<sub>2</sub>CF<sub>3</sub>)<sub>2</sub> arises from the observation that the -CF<sub>3</sub> groups projecting into the interchain space in PEO<sub>3</sub>:LiCF<sub>3</sub>SO<sub>3</sub> results in increased spacing of the PEO helices. Thus, it was proposed that this could be a reason for the high conductivity of systems involving this salt and also for the higher conductivity still of systems based on salts such as PEO:Li[(CF<sub>3</sub>SO<sub>2</sub>)<sub>2</sub>N] and PEO:Li[(CF<sub>3</sub>SO<sub>2</sub>)<sub>3</sub>C]. In addition, with a salt of this type with two coordinating groups which have a certain degree of independent motion there is a possibility of interchain cross-links or a higher degree of intra-chain cation co-ordination.

As interesting as this system is, initial attempts at structural solution proved difficult. Techniques such as Patterson synthesis, direct methods and model building based on the PEO<sub>3</sub>:LiCF<sub>3</sub>SO<sub>3</sub> structure were tried but none yielded a refinable structural model. The failure of these methods was partly due to the highly flexible N(SO<sub>2</sub>CF<sub>3</sub>)<sub>2</sub><sup>-</sup> anion. Thus a novel variation of the simulated annealing method was developed which

included the ability to handle flexible molecules and include tests for chemical reasonableness. The mechanics of this method are covered in further detail in chapter 3 of this thesis.

After Rietveld refinement of the best model from the simulated annealing procedure, a good fit was obtained with agreement factors of  $R_{wp}=5.6\%$  achieved. The structure involved the PEO chain taking up the helical  $t_2gt_2gt_2\bar{g}$  conformation typical of  $PEO_3:salt$  compounds but with a chain axis slightly larger than that of  $PEO_3:LiCF_3SO_3$  at  $8.66\text{\AA}$  against  $8.61\text{\AA}$ . The PEO chains were also spaced slightly further apart, as may be predicted given the larger unit cell. As in  $PEO_3:LiCF_3SO_3$ , the  $Li^+$  ions are located in every turn of the helix and are five co-ordinated by three ether oxygens and one oxygens from each of two separate imide anions. Only one  $-SO_2$  moiety from the imide group is involved in co-ordination, the rest of the imide projects into the interchain space but does not interact with other PEO chains or the anions and cations associated with them. Thus this compound, like the other  $PEO_3:salt$  compounds, exhibits no cross linking between chains and can be regarded as isolated, columnar co-ordination compounds. The increased interchain space relative to  $PEO_3:LiCF_3SO_3$  could be one reason for the increased amorphicity, decrease in melting temperature for the crystalline phase and increased conductivity. Despite this, other factors such as the high degree of

charge delocalisation, low basicity and relative immobility of the anion are highly likely to also be of significance in the high ionic conductivity.

## Section 2.4: References

- [1] F.M.Gray, *Solid Polymer Electrolytes - Fundamentals and Technological Applications*, VCH publishers, New York (1991)
- [2] D.F.Schriver and P.G.Bruce in *Solid State Electrochemistry*, ed. P.G.Bruce, Cambridge University Press, Cambridge (1995)
- [3] R.Frech, S.Chintapalli, P.G.Bruce, C.A.Vincent, *J. Chem. Soc. Chem. Commun.*, **2** (1997) 157
- [4] A.K.Cheetham, P.Day, *Solid State Chemistry – Techniques* (1987)
- [5] A.Larson, R.Von.Dreele, Los Alamos National Laboratory, LA-UR-86-748 (1987)
- [6] C.Giacovazzo, *Fundamentals of crystallography*, IUCr (1992)
- [7] A.March, *Z. Kristallogr.*, **81** (1932) 267  
W.A.Dollase, *J.Appl. Cryst.*, **19** (1986) 267
- [8] P-E.Werner, L.Eriksson, M.Westdahl, *J. Appl. Crystallogr.*, **18** (1985) 367
- [9] J.W.Visser, *J. Appl. Cryst.*, **2** (1969) 89
- [10] P.M.DeWolff, *J. Appl. Crystallogr.*, **1**(1968) 108
- [11] *International Tables for Crystallography Volume A – Space Group Symmetry* ed. T.Hahn, IUCr, Holland (1983)
- [12] C.Giacovazzo, *Acta Crystallographica Section A*, **40** (1984) 418
- [13] C.Giacovazzo, *Acta Crystallographica Section A*, **47** (1991) 256
- [14] W.Dong, C.J.Gilmore, *Acta Crystallographica Section A*, **54** (1998) 438

- [15] K.D.M.Harris, B.M.Kariuki, M.J.Tremayne, *Materials Science Forum*, **278** (1998) 32
- [16] B.M.Kariuki, H.Serrano-Gonzalez, R.L.Johnston, K.D.M.Harris, *Chemical Physics Letters*, **280** (1997) 189
- [17] A.LeBail, H.Duroy, J.L.Fourquet, *Mat. Res. Bull.*, **23** (1988) 447
- [18] G.S.Pawley, *J. Appl. Crystallogr.* **14** (1981) 357.
- [19] D.Sayre, *Acta Cryst.*, **5** (1952) 60
- [20] D.Louer, M.Louer, *J. Solid State Chem.*, **68** (1987) 292
- [21] R.E.Morris, W.T.A.Harrison, J.M.Nicol, A.P.Wilkinson, A.K.Cheetham, *Nature*, **359** (1992) 519
- [22] K.Shankland, W.I.F.David, D.S.Sivia, *J. Mater. Chem.*, **7(3)** (1997) 569
- [23] D.Louer, *Journal de Physique IV*, **6** (1996) 57
- [24] H.M.Rietveld, *J. Appl. Cryst.*, **2** (1969) 65
- [25] C.J.Howard, *J. Appl. Cryst.*, **15** (1982) 615
- P.Thomson, D.E.Cox, J.B.Hastings, *J.Appl. Cryst.*, **20** (1987) 79
- [26] R.Iwamoto, Y.Saito, H.Ishihara, H.Tadokoro, *J. Polymer Sci.*, **6** (1968) 1509
- [27] M.Yokoyama, H.Ishihara, R.Iwamoto, H.Tadokoro, *Macromolecules*, **2** (1969) 184
- [28] Y.Chatani, S.Okamura, *Polymer*, **28** (1987) 1815
- [29] B.L.Papke, *J. Phys. Chem. Solids*, **42** (1981) 493

- [30] B.L.Papke, M.A.Ratner, D.F.Schrive, *J. Electrochem. Soc.*, **129** (1982) 1694
- [31] J.M.Parker, P.V.Wright, C.C.Lee, *Polymer*, **22** (1981) 1305
- [32] M.B.Armand, J.M.Chabagno, M.J.Duclot, *Fast-ion Transport in Solids*, ed. P.Vashishta, J.N.Mundy, G.Shenog, North-Holland, Amsterdam (1979) 131
- [33] Y.Chatani, Y.Fujii, T.Takayanagi, A.Honma, *Polymer*, **31** (1990) 2238
- [34] P.Lightfoot, M.A.Mehta, P.G.Bruce, *J. Mater. Chem.*, **2(4)** (1992) 379
- [35] P.Lightfoot, M.A.Mehta, P.G.Bruce, *Science*, **262** (1993) 883
- [36] P.Lightfoot, J.L.Nowinski, P.G.Bruce, *J. Am. Chem. Soc.*, **116** (1994) 7469
- [37] J.B.Thomson, P.Lightfoot, P.G.Bruce, *Solid State Ionics*, **85** (1996) 203
- [38] T.Hibma, *Solid State Ionics*, **9/10** (1983) 1101
- [39] Y.G.Andreev, P.Lightfoot, P.G.Bruce, *Chem. Commun.*, (1996) 2169

## **Chapter 3: The Simulated Annealing Method of Ab-Initio Structure Solution from Powder Diffraction**

### **Section 3.1: Introduction**

As detailed in the previous chapter, powder x-ray diffraction provides a unique level of structural information in systems where single crystals are unavailable. However, the technique is far from trivial and hurdles such as the phase and the overlap problems must be overcome. The phase problem arises as a result of the fact that information on the magnitude of a reflection can be obtained from the x-ray diffraction experiment but not the phase of the reflection. This can be overcome in single crystal methods through the use of techniques such as direct methods and the Patterson function. However, these rely on the accurate extraction of the intensities of each reflection. This is a trivial problem in single crystal diffraction in which it is possible to select a plane to bring into a condition to diffract via mechanical rotation of the crystal. This is impossible in powder diffraction due to the fact that the sample is made up of crystallites in many different orientations. Thus, the data received contains a superposition of the reflections from all the planes in three dimensions into a one-dimensional data set, resulting in the accidental overlap of peaks. This overlap can also arise from symmetry imposed degeneracy of the Bragg peaks. The problem of accidental overlap of peaks is compounded by the effect of peak broadening which is caused

by several factors including instrumental effects, crystallite size and thermal vibrations. Several instrumental and procedural advances have been made in order to minimise these effects. High resolution, tuneable synchrotron sources such as the ESRF in Grenoble have allowed the separation of overlapped peaks through good instrumentation coupled with variable wavelength radiation<sup>1</sup>. Also, novel methods have been developed to allow separation of overlapped peaks through thermal treatments<sup>2</sup>.

Most approaches to structural solution from powder diffraction data involve an extension of single crystal methods and as such rely on determining the individual contribution of several overlapped Bragg peaks. There are a number of methods available for carrying out this determination. These include the Pawley<sup>3</sup> and LeBail<sup>4</sup> methods in which a least-squares refinement is carried out on a goodness of fit function but with only peak shape, background and zero-point being refined. In the LeBail method, the initial intensities are calculated using an arbitrarily positioned dummy atom and recalculated at the end of each refinement cycle. More advanced techniques have incorporated the use of statistical methods such as Bayesian methods<sup>5</sup>. A more diverse approach was taken in the use of entropy maximisation and likelihood ranking<sup>6</sup>, which repeatedly partitions the intensities during the actual process of structure solution. However, these techniques are fundamentally limited in that any

assigning of intensities to overlapped peaks necessarily involves a degree of speculation that becomes more severe as the degree of peak overlap increases. Thus, a method that bypasses the problem would be preferable.

One approach is to adapt the Rietveld method<sup>7</sup> which is used to refine approximate structural models into more exact solutions. This technique involves the generation of a calculated diffraction pattern from the approximate structures, which can then be compared to that obtained experimentally. However, this technique relies on a least squares algorithm that, by only allowing downhill steps in the goodness of fit function, necessarily finds only the closest minimum to the starting point. Therefore, unless a good starting model is known, it is unlikely to find the global minimum, which corresponds to the true structure. Thus for ab-initio structure solution, where no reasonable starting model is available, some algorithm capable of finding the global minimum must be used.

### **Section 3.2: The Simulated Annealing Method**

The simulated annealing algorithm is one such algorithm and has been successfully applied to several general modelling problems such as component placement in a computer circuit board and in minimising journey times for travelling salesmen<sup>8</sup>. The potential of simulated annealing for structure solution from powder diffraction data was first

demonstrated by Newsam, Deam and Freeman<sup>9</sup> and subsequently developed and applied to the solution of previously unknown structures by Andreev, Lightfoot and Bruce<sup>10</sup>. An analogy of the simulated annealing algorithm can be found in the process of crystallisation.

In the statistical mechanics of solid state chemistry, when materials are at elevated temperatures, i.e. the atoms have high kinetic energy; the crystalline state is insignificant. However, the crystalline state, corresponding to a minimum energy configuration, is vastly more common at lower temperatures. In the high temperature state, motions of the constituent atoms are chaotic. If the temperature is reduced quickly, i.e. the material is quenched, then the system tends to get frozen in an amorphous state, which corresponds to a local minimum in energy of the system. This is generally higher in energy than the appropriate crystalline state. The crystalline state is commonly reached by slowly reducing the temperature, allowing the atoms to fully explore the energy space, taking both uphill and downhill steps until they are trapped in the deepest (global) minimum. The simulated annealing algorithm originates from comparing energy to goodness of fit and introducing a temperature like attenuating term which controls the size of variation in goodness of fit allowed.

Thus, the simulated annealing method when applied to structure solution involves the generation of a random but chemically plausible initial structural model. The modification of the model is achieved through alteration of the parameter values, for example, bond lengths, bond angles and torsion angles as follows:

$$p_l = p_l + r\Delta p_l \quad \text{Eqn. 3.1}$$

For all parameters  $p_l$  where  $l$  ranges from 1 to  $N$ ,  $N$  being the total number of parameters,  $r$  is a fractional random number in the range  $[-1,1]$  and  $\Delta p_l$  is a predefined maximum step size for the parameter.

Once the variations in the parameter set have taken place, i.e. a new structural model has been generated, a x-ray diffraction pattern for the model is generated. This calculated pattern is then compared with the experimental pattern using the  $\chi^2$  goodness of fit function described previously in chapter 2. The choice of whether a variation of the parameters, known as a move, is accepted must include the possibility of accepting a move that increases the  $\chi^2$  of the system. This is carried out using an importance-sampling algorithm<sup>11</sup>, which performs selection on the following basis:

A move is accepted if:

$$\chi^2_{\text{new}} < \chi^2_{\text{old}} \quad \text{or} \quad \text{Eqn.3.2}$$

$$\exp[-(\chi^2_{\text{new}} - \chi^2_{\text{old}})/\delta\chi^2_{\text{cur}}] > R \quad \text{Eqn.3.3}$$

Where  $\chi^2_{\text{new}}$  is the goodness of fit of the proposed model,  $\chi^2_{\text{old}}$  is the goodness of fit of the last accepted model,  $\delta\chi^2_{\text{cur}}$  is the temperature analogue term and R is a random number in the range [0,1].

In this way, downhill steps in  $\chi^2$  are always accepted using Eqn.3.2, thus ensuring minimisation. However, the key to the method and also where it differs from Rietveld least squares refinement, is in the second term, Eqn.3.3. This uses Boltzmann type statistics to allow moves to be accepted which result in an increase in the  $\chi^2$  function. The size of the uphill steps possible is determined by the temperature term. This is generally large at the start of the structure solution process, allowing large uphill steps in  $\chi^2$  which allows the minimisation process to escape any local minima. The "temperature" is then slowly reduced throughout the process, lessening the likelihood of large uphill steps and thus allowing the minimisation to converge to the global minimum. This process of making displacements in the parameter values followed by the acceptance/rejection procedure continues until a set number of moves or accepted moves are made at a particular temperature,  $\delta\chi^2_{\text{cur}}$ . After this

point, the temperature is reduced by a predetermined factor,  $f_1$ . The cycle continues in iterative fashion until a set number of temperature reductions have been made or until there are no accepted moves at a particular temperature. At this point, the model with the lowest  $\chi^2$  should be the actual solution.

Despite, the effectiveness of this method in locating the global minimum, there is also a disadvantage. The repeated model generating and profile calculation steps, coupled with the necessity of a slow reduction in temperature make this procedure relatively slow and computationally expensive. Thus, it is preferable to take a range of measures in order to reduce the calculation time.

One way to reduce the calculation time is to fix certain parameters, such as profile parameters, at approximate values which however provide a reasonable non structure related fit to the experimental pattern. During the course of this work, the unit cell size and the profile parameters were all kept at constant values obtained from a LeBail fit<sup>4</sup> of the experimental pattern. The obvious gain from this approach lies in the reduction of variables, leading to a reduction of computational requirements and hence time. The trade-off is that, although the values obtained for these parameters from the LeBail fit are a reasonable approximation, they are not exact. Therefore, the simulating annealing algorithm can only be

expected to finish close to, rather than exactly at, the global minimum. Thus, the saving must be considered against the need for Rietveld refinement to complete the structure solution. Another method used to reduce the computational time, lessen the problem complexity and bias the structure solution towards reasonable results is through the use of chemical restraints.

Chemical restraints or constraints provide a means of "building" chemical knowledge into the structure solution process in order to reduce the computational workload or to aid the location of the global minimum. In general, two types of approach can be used, either soft restraints or hard constraints.

Soft restraints are already widely used in the refinement process and involve the addition of a punishing term to the goodness of fit function. The punishing term is generally a function of the difference between the actual and an expected value. Thus, parameters can vary markedly from the expected value as long as the gain in goodness of fit justifies it. This has the advantages that the minimisation process can progress from an incorrect model to the correct model via an unrealistic model. In addition, if a parameter has an actual value that is outwith the range of those found before, it can be determined. It has the disadvantage that before any consideration is made then a new x-ray diffraction profile has to be

calculated, thus wasting time by calculating patterns for unrealistic structures, which is very time consuming. Thus, in order to save computational time, a system of hard restraints has been employed in the structure solutions carried out in the work presented in this thesis.

The hard restraint system involves setting a range within which a parameter, e.g. a bond length, can vary. The range is chosen based on knowledge of usual values of the parameter from similar systems with a bit of lee-way added. If a parameter is found to lie outwith the set range then the variation in the parameter is rejected immediately without the need to calculate a diffraction pattern. This method has the advantage that it vastly reduces the computational time and also rules out unrealistic models. However, the trade off, as discussed above, is that the minimisation process does not have the freedom to move to the global minimum via an unrealistic model. It is not just parameter values that can be subjected to this removal of unrealistic models. It is also possible to reject a move due to two molecular fragments approaching too close. In addition, if the compound has a molecular fragment that is continuous at a junction of the asymmetric unit, such as a continuous chain of a polymer, then this continuity can be used as the basis of a hard restraint. Once again, these time saving measures should be considered against the chance that the global minimum will not be found due to the fact that the proximity check will not allow molecular fragments to pass through

each other. Thus if there are two large molecular fragments in a crowded unit cell then they may prevent each other from moving to their correct positions. In addition, the time savings generated through the use of hard constraints must be balanced against the time wasted through the rejection of a large amount of moves. This is particularly prevalent in the case of continuity checks at the junction of the asymmetric unit. The careful use of hard restraints can result in significant savings in computational time. In order for them to be applied, it is necessary to describe the molecular fragments in the unit cell in terms of meaningful parameters such as bond lengths, angles and torsion angles that can be subject to chemical intuition.

In the work presented here, this geometrical description was achieved by describing each molecular fragment in its own Cartesian frame with an origin on an atom that is bonded to at least two other atoms. This allows definition of one of the bonds as being the direction of the X-axis. The Y-axis is defined as being perpendicular to the X-axis and lying in the plane containing both bonds attached to the origin atom. Appropriate placing of the Z-axis then creates a right-handed orthogonal frame. A typical Cartesian frame set up is shown in fig. 3.1 for an trifluoromethane sulphonimide,  $(\text{CF}_3\text{SO}_2)_2\text{N}^-$ , ion. After selection of the frame of reference, the next step is to devise a system to geometrically describe the molecular fragment.

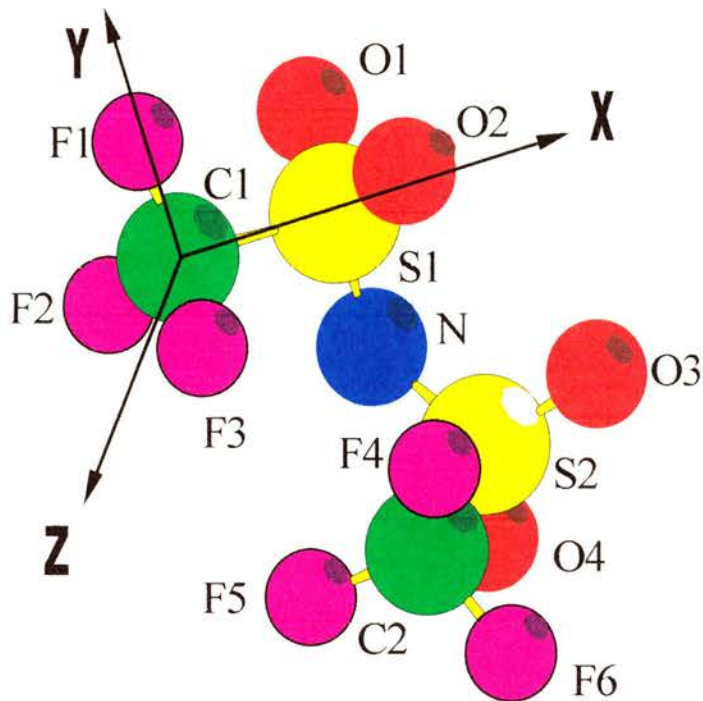


Fig.3.1: The Local Cartesian Frame for an Imide Anion<sup>10</sup>

Clearly, the placement of the atoms connected to the origin is a trivial case of geometry involving the appropriate bond lengths and angles. The other atoms of a fragment present a more complicated case that requires the use of the following formula to describe the position of an atom lying on a bonded path or chain<sup>12</sup>:

$$\begin{bmatrix} x_m^j \\ y_m^j \\ z_m^j \end{bmatrix} = \sum_{i=m}^{N-3} \left( \left( \prod_{j=N-3, -1}^i [\mathbf{A}^j] \right) \begin{bmatrix} l_{i,i+1} \\ 0 \\ 0 \end{bmatrix} \right) + \begin{bmatrix} l_{N-2, N-1} \\ 0 \\ 0 \end{bmatrix}$$

Where  $[\mathbf{A}^j]$  is a rotational matrix defined by:

$$[\mathbf{A}^j] = \begin{bmatrix} -\cos \phi^j & -\sin \phi^j & 0 \\ \sin \phi^j \cos \tau^j & -\cos \phi^j \cos \tau^j & \sin \tau^j \\ -\sin \phi^j \sin \tau^j & \cos \phi^j \sin \tau^j & \cos \tau^j \end{bmatrix},$$

where  $\theta^j \equiv \theta_{j,j+1,j+2}$ ,  $\tau^j \equiv \tau_{j,j+1,j+2,j+3}$ ,

Also,  $l_{i,i+1}$  denotes the length of the bond between atom  $i$  and atom  $i+1$ ,  $\phi_{j,j+1,j+2}$  denotes the angle formed by atoms  $j$ ,  $j+1$  and  $j+2$  and  $\tau$  denotes the torsion angle between atoms  $j$ ,  $j+1$ ,  $j+2$  and  $j+3$ .

When an atom is bonded to more than two neighbours, it is often convenient to compute the coordinates of the  $k^{\text{th}}$  bonded neighbour of an atom,  $m-1$ , by rotating the  $m^{\text{th}}$  atom around the bond between atom  $m-1$  and atom  $m-2$  and adjusting the new bond length accordingly, fig. 3.2.

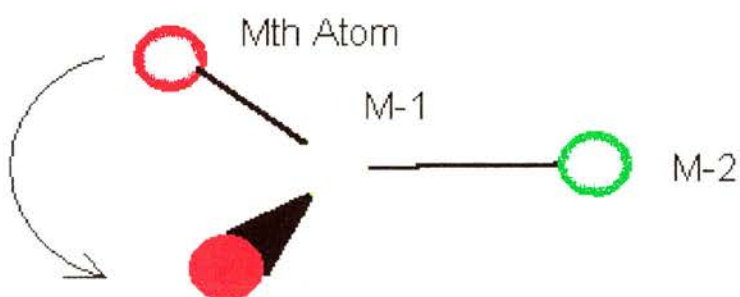


Fig.3.2: Description of an atoms location through the rotation of another atom.

This can be achieved using a rotational transformation of the form<sup>10</sup>:

$$\begin{bmatrix} x'_{m+k} & y'_{m+k} & z'_{m+k} \end{bmatrix} = \begin{bmatrix} x'_m(l_{m-1,m+k}) & y'_m(l_{m-1,m+k}) & z'_m(l_{m-1,m+k}) \end{bmatrix} \cdot [\mathbf{r}],$$

With,

$$[\mathbf{r}] = \begin{bmatrix} \cos \alpha + l_1^2(1 - \cos \alpha) & l_1 l_2(1 - \cos \alpha) + l_3 \sin \alpha & l_3 l_1(1 - \cos \alpha) - l_2 \sin \alpha \\ l_1 l_2(1 - \cos \alpha) - l_3 \sin \alpha & l_3 \cos \alpha + l_2^2(1 - \cos \alpha) & l_2 l_3(1 - \cos \alpha) + l_1 \sin \alpha \\ l_3 l_1(1 - \cos \alpha) + l_2 \sin \alpha & l_2 l_3(1 - \cos \alpha) - l_1 \sin \alpha & \cos \alpha + l_3^2(1 - \cos \alpha) \end{bmatrix},$$

$l_1$ ,  $l_2$  and  $l_3$  are the direction cosines in the Cartesian frame of the rotation axis, i.e. the bond between then  $(m-1)^{\text{th}}$  atom and atom  $m-2$ .  $\alpha$  is the angle of rotation.

So, in summary, a geometrical description of each molecular fragment can be achieved by describing the fragment in terms of its own Cartesian frame of reference. Once a suitable atom has been selected as an origin, the rest of the fragment can be described using a series of chain generations and rotations all involving geometrical quantities such as bond lengths, bond angles and torsion angles. Thus, the parameter set has been changed such that the variables are all geometrical quantities that are easier to check for reasonableness and restrain than crystallographic co-ordinates. In addition, this approach establishes connectivity between atoms, thus further reducing the searchable parameter space. However, in order to calculate the expected diffraction pattern from each trial model, it is necessary to transform the system back into the crystallographic frame.

In order to make the transformation into the crystallographic frame it is necessary to know the position and orientation of each local Cartesian frame with respect to the crystallographic frame. Thus, in addition to the chemical parameters discussed above, the crystallographic co-ordinates of each origin atom and the Eulerian angles of each Cartesian frame have to be added to the parameter set. Using these additional parameters, the transformation from an individual Cartesian frame to the crystallographic frame may be carried out by first transforming the local frame into the general Cartesian frame, whose origin is coincident to that of the crystallographic frame. Thus, the total transformation may be carried out using the following equation for all atoms  $i$ :

$$\begin{bmatrix} x_i \\ y_i \\ z_i \end{bmatrix} = [\mathbf{C}] \cdot \left( [\mathbf{R}] \cdot \begin{bmatrix} x'_i \\ y'_i \\ z'_i \end{bmatrix} \right) + \begin{bmatrix} x_{N-1} \\ y_{N-1} \\ z_{N-1} \end{bmatrix},$$

The matrix  $[\mathbf{R}]$  performs the transformation into the general Cartesian frame<sup>13</sup>,  $[\mathbf{C}]$  then executes the transformation into the crystallographic frame<sup>13</sup>. The crystallographic co-ordinates of the origin atom of the local Cartesian frame are  $x_{N-1}$ ,  $y_{N-1}$  and  $z_{N-1}$ .

The transformational matrix  $[\mathbf{R}]$  has the following components:

$$[\mathbf{R}] = \begin{bmatrix} \cos \Psi \cos \Phi - \cos \Theta \sin \Phi \sin \Psi & -\sin \Psi \cos \Phi - \cos \Theta \sin \Phi \cos \Psi & \sin \Theta \sin \Phi \\ \cos \Psi \sin \Phi + \cos \Theta \cos \Phi \sin \Psi & -\sin \Psi \sin \Phi - \cos \Theta \cos \Phi \cos \Psi & -\sin \Theta \cos \Phi \\ \sin \Theta \sin \Psi & \cos \Psi \sin \Theta & \cos \Theta \end{bmatrix}$$

Whilst the  $[\mathbf{C}]$  matrix is defined as follows:

$$[\mathbf{C}] = \begin{bmatrix} \frac{1}{a} & \frac{-ab \cos \gamma}{a^2 b \sin \gamma} & \frac{bc(\cos \gamma \cos \alpha - \cos \beta)}{V \sin \gamma} \\ 0 & \frac{1}{b \sin \gamma} & \frac{ac(\cos \beta \cos \gamma - \cos \alpha)}{V \sin \gamma} \\ 0 & 0 & \frac{ab \sin \gamma}{V} \end{bmatrix},$$

where  $V = abc \sqrt{1 + 2 \cos \alpha \cos \beta \cos \gamma - \cos^2 \alpha - \cos^2 \beta - \cos^2 \gamma}$ ,

$\Theta$ ,  $\Phi$  and  $\Psi$  are the Euler angles, superscript  $l$  denotes a parameter belonging to the local Cartesian frame and  $a$ ,  $b$ ,  $c$ ,  $\alpha$ ,  $\beta$  and  $\gamma$  are the unit cell parameters.

Using these transformations to convert the crystallographic co-ordinates into a parameter set which consists largely of chemically meaningful quantities, it is trivial to restrict the bond lengths, bond angles and torsion angles to realistic limits. In addition, it is possible to add further restraints by defining certain like bond lengths or angles to have identical values, thus further reducing the computational time. Furthermore, it is also provides the convenience of being able to follow the minimisation process by analysing meaningful parameters. Thus, the technique presented here

provides a structure solution method that does not rely on extracted intensities and is thus less susceptible to the overlap problem. It is also capable of reasonably rapid operation as well as a capacity for handling fully flexible molecules. It is however not to be taken as a fully automated technique as it still requires both judgement of the level of compromises made in order to reduce computational time and chemical knowledge to assist the solution process.

### Section 3.3: References

- [1] D.Louer. *Journal de Physique IV*, **6** (1996) 57
- [2] K.Shankland, W.I.F.David, D.S.Sivia, *J. Mater. Chem.*, **7(3)** (1997) 569
- [3] G.S.Pawley, *J. Appl. Crystallogr.* **14** (1981) 357.
- [4] A.LeBail, H.Duroy, J.L.Fourquet, *Mat. Res. Bull.* **23** (1988) 447.
- [5] D.S.Sivia, W.I.F.David, *Acta Crystallogr. A* **50** (1994) 703.
- [6] C.J.Gilmore, K.Henderson, G.Bricogne, *Acta Crystallogr. A* **47** (1991) 830.
- [7] H.M.Rietveld, *J. Appl. Cryst.*, **2** (1969) 65
- [8] S.Kirkpatrick, C.D.Gelatt Jr., M.P.Vecchi, *Science* **220** (1983) 671.
- [9] J.M.Newsam, M.W.Deam, C.M.Freeman, *Accuracy in powder diffraction II - NIST special publication no.846* (1992) 80
- [10] Y.G.Andreev, P.Lightfoot, P.G.Bruce, *J.Appl. Crystallogr.* **30** (1997) 294.
- [11] N.Metropolis, A.W.Rosenbluth, M.W.Rosenbluth, A.H.Teller and E.Teller, *J. Chem. Phys.* **21** (1953) 1087
- [12] S.Arnott, A.J.Wonacott, *Polymer* **7** (1966) 157
- [13] H.Goldstein, *Classical Mechanics*, Addison-Wesley, 1980

## Chapter 4: Ab-Initio Structure Solution of PEO:Sodium Trifluoromethane Sulphonate (PEO:NaCF<sub>3</sub>SO<sub>3</sub>) from Powder X-ray Diffraction Data

### Section 4.1: Introduction - The Need for Structure Solution

As discussed in chapter 1, knowledge of detailed structural data of ionically conducting polymers can provide great insight into the ion conduction and solvation processes in these materials. In addition, knowledge of crystal structures is of great assistance when applying other techniques such as IR spectroscopy<sup>1</sup> and NMR<sup>2</sup>. In terms of crystal structures, the most complete studies have been of complexes with ethylene oxide (EO) to salt ratios of 3:1 and 4:1<sup>3-10</sup>. Only two polymer:salt complexes with an EO:salt ratio of 1:1, PEO:HgCl<sub>2</sub><sup>11</sup> and PEO:NaSCN<sup>6</sup>, have been solved so far. There are several reasons for widening knowledge of the structures of these 1:1 compounds. A structural study of a compound such as PEO:NaCF<sub>3</sub>SO<sub>3</sub> can, through comparison with the structure of PEO:NaSCN, provide greater insight into the anionic effects in 1:1 compounds. Furthermore, both of the existing structures in this class were determined largely from single crystal data. However, it is extremely hard to produce single crystals of sufficient quality and it has been shown<sup>9</sup> that in the case of PEO<sub>4</sub>:KSCN, the structure proposed on the basis of single crystal data<sup>12</sup> was in error. Thus, in the light of developments in the ab-initio structure solution of polymer/salt complexes from higher quality powder diffraction data<sup>4,9</sup> it is of interest to apply these

techniques to the study of a compound with an EO:salt ratio of 1:1. In addition, there has been some variation in sodium co-ordination in the PEO:Na salt compounds solved so far, with the sodium ion being five co-ordinated in PEO<sub>3</sub>:NaI and PEO<sub>3</sub>:NaClO<sub>4</sub> and six co-ordinated in PEO:NaSCN and PEO<sub>3</sub>:NaSCN. The study of PEO:NaCF<sub>3</sub>SO<sub>3</sub> allows further examination of this phenomenon.

#### **Section 4.2: Experimental Details**

PEO (Aldrich) was dried under dynamic vacuum at 60°C and Sodium triflate (Aldrich, 98%) was dried under dynamic vacuum at 100°C, both for three days, before being transferred to an argon filled glove box. The dried PEO and sodium triflate was mixed together in appropriate quantities and sealed into a cryogrinding pot, along with a selection of metal ball bearings. This was then placed in a bath of liquid nitrogen and shaken vigorously for 30 minutes. The resulting finely ground mixture was used to fill a 0.7mm diameter, Lindemann (glass capillary) tubes whilst in an argon atmosphere. These were sealed using silicone sealant. The thermal treatment of these samples is crucial in achieving a high degree of crystallisation.

To optimise crystallisation, it is best to heat samples in the region of the melting point before annealing below the melting point. However, this can vary depending on the system under study. To determine the optimum

conditions for crystallisation in the case of PEO:NaCF<sub>3</sub>SO<sub>3</sub>, a range of heating schemes was applied to the mixtures, after consultation of the phase diagram for the system<sup>13</sup>. Powder x-ray diffraction experiments were carried out on each sample. As can be seen from the results, fig. 4.1, the best results, with no visible PEO or salt and the highest signal to noise ratio was achieved when the mixture was just melted at 275°C for three hours before being annealed at 70°C for three days to promote crystallisation. After this time, the temperature was slowly reduced to room temperature. Thus, this thermal treatment was used to prepare the samples used in the structure solution process.

The powder x-ray diffraction data was collected in the range  $5^\circ < 2\theta < 60^\circ$  in  $0.02^\circ$  steps on a Stoe Darmstadt Stadi/p high-resolution x-ray powder diffractometer, using Cu K<sub>α1</sub> radiation and a small angle, position sensitive detector over a period of twelve hours.

### **Section 4.3: Structure Determination**

Indexing of the lattice parameters by means of the TREOR<sup>14</sup> program yielded a monoclinic unit cell with approximate cell dimensions of  $a = 9.831\text{\AA}$ ,  $b = 12.758\text{\AA}$ ,  $c = 5.761\text{\AA}$ ,  $\beta = 90.5$ . All lines were indexed with a DeWolff<sup>15</sup> figure of merit of 30.8. In addition, there was also the possibility of an orthorhombic cell of  $a = 9.830\text{\AA}$ ,  $b = 12.761\text{\AA}$ ,  $c = 5.762\text{\AA}$  with a figure of merit of 48.2. This is interesting because the unit cell for

PEO:HgCl<sub>2</sub> is also orthorhombic<sup>11</sup>, however, there were also five significant unindexed peaks in the pattern which implies that there are either impurities in the system which are neither salt nor PEO or that the proposed orthorhombic cell is wrong. For the more plausible monoclinic cell, a space group of P2<sub>1</sub>/c was selected based on systematic absences. A Le Bail fitting procedure<sup>16</sup> was carried out on some of the possible space groups and unit cells. Of these, the best fit was achieved with the monoclinic space group P2<sub>1</sub>/c with a  $\chi^2$  of 2.94, fig.4.2. The best orthorhombic group was P2mm with a  $\chi^2$  of 5.243, fig.4.3, whilst the orthorhombic group Pca2<sub>1</sub> found by Yokoyama et al.<sup>11</sup> for PEO:HgCl<sub>2</sub> achieved a  $\chi^2$  of only 6.241, fig. 4.4. In addition, the ratios of the main peaks in diffraction intensity were consistently wrong in the case of all the orthorhombic systems tried. Thus, it can be deduced without much doubt that this compound belongs to the monoclinic P2<sub>1</sub>/c spacegroup. It was assumed that there were four formula units in the unit cell, which gave a density of 1.53gcm<sup>-3</sup> which is consistent with other, similar compounds. Thus, it is probable that all the atoms in the unit cell occupy 4e general positions.

The simulated annealing method has been shown to be effective in the structural solution of PEO<sub>3</sub>:LiN(SO<sub>2</sub>CF<sub>3</sub>)<sub>2</sub><sup>4</sup> which has many aspects in common with PEO:NaCF<sub>3</sub>SO<sub>3</sub> such as a flexible polymer chain and anion. Thus, this method was also selected for the structure solution in

this case. The simulated annealing program was written using Microsoft Visual C++ on a dual 100MHz Pentium PC. The calculated diffraction intensities and pattern-profile calculation were carried out using code modified from the public domain software package CPSR<sup>17</sup>. The routines<sup>18</sup> RAN3 and IRBIT1 were used to generate random numbers and random bits respectively.

As detailed in chapter 3, the key aspect of this method is the separation of the system into different fragments and the use of chemically interpretable variables in local Cartesian frames. There are three molecular fragments in the asymmetric unit, namely the Na<sup>+</sup> cation, the CF<sub>3</sub>SO<sub>3</sub><sup>-</sup> anion and one ethylene oxide unit. The hydrogens belonging to the ethylene oxide (EO) repeat unit were not included at this stage of the structure solution in order to reduce the computational workload. No local Cartesian frame was used to describe the sodium cation since this can be adequately placed using the crystallographic co-ordinates alone.

The sulphur atom of the triflate anion was used as the origin of the triflate's Cartesian frame. The x-axis was placed along the S-C bond and the y-axis placed perpendicular to the x-axis in the plane of the S-O1 bond with the z-axis being selected to make up a right-handed orthogonal frame, fig. 4.5. The remaining oxygens were located via rotations of the S-O1 bond about the S-C axis as detailed in section 3.2. The position of

the first fluorine atom, F1, was described using the chain formula, eqn.3.4, and the remaining fluorines were placed via rotations of the C-F1 bond around the S-C axis in similar fashion to the oxygens. In this first S.A. run, in order to save time and simplify the solution process, all S-O bond lengths were treated as equivalent and similarly for C-S-O angles, O-S-O angles, C-F bond lengths, S-C-F angles and F-C-F angles. This did not appear to significantly hamper the structural solution of  $\text{PEO}_3:\text{LiN}(\text{SO}_2\text{CF}_3)_2$  but greatly reduces the number of variables. Thus, the triflate group can be described using 14 variables instead of 24. Namely, the crystallographic co-ordinates of the sulphur atom ( $x_s$ ,  $y_s$  and  $z_s$ ), the Eulerian angles,  $\Theta$ ,  $\Phi$  and  $\Psi$ , the C-S bond length, the C-F bond length, the S-O bond length, the S-C-F angle, the C-S-O angle, the O-S-O angle, the F-C-F angle and the F-C-S-O torsion angle.

In similar fashion, the origin of the Cartesian frame for the section of PEO chain was defined as the middle atom, i.e. the penultimate carbon. The x-axis was defined as lying along the C-O bond, the y-axis as lying perpendicular to the x-axis in the plane of the C-C bond and the z-axis placed to make up a right-handed orthogonal set, fig. 4.6. Thus, the positions of the two non-origin atoms of the PEO chain repeat unit can be determined through application of simple geometry to the C-O bond length, the C-C bond length and the O-C-C angle. Therefore, including the crystallographic co-ordinates of the origin carbon and the Eulerian

angles, the PEO chain was described by nine variables. This results in a total of 27 parameters being varied in the whole of this stage of the structure solution process. This also includes the scale factor which was refined using a linear least squares method at the end of each cycle.

In order to reduce the parameter space and create a bias towards believable models, checks were made on the plausibility of each model before calculation of the diffraction pattern. These included checks to prevent two triflate anions or a triflate anion and the PEO chain or two cations coming too close to one another, with the criteria for this being no less than 80% of the sum of the Van der Waals radii.

The starting point of the first MC run consisted of randomly generated but plausible molecular fragments with equivalent bond lengths and angles in the triflate group having the same value, fig. 4.7. The starting configuration was clearly random with a very poor fit, fig. 4.8. The 27 parameters were then varied according to the simulated annealing scheme. The total number of moves at a particular temperature,  $N_{\text{tot}}$ , was set to 5000; the initial "temperature" ( $\Delta\chi^2_{\text{cur}}$ ) set to 5 and the temperature reduction factor,  $f_1$ , was 0.1. This allowed large variations in  $\chi^2$  which permits a significant number of uphill steps at the early stages of minimisation. This reduction in temperature allows the process to be "frozen out" at a position that is considerably more likely to correspond to

the global minimum than the application of least squares to a randomly chosen structure.

Considerable movement of the fragments can be seen as a result of this first MC run, fig. 4.9, which resulted in a significant improvement of fit, fig. 4.10. However, as can be seen from fig. 4.9, the polymer chain is still non-continuous at the junctions of the asymmetric units. An attempt was made to remedy this situation by re-running the MC procedure using the results from the first MC run but with only the chain being varied and only trial configurations which gave a continuous polymer chain along the c-axis being accepted. The continuity of the chain was decided through visual inspection. This led to a small, expected 7% increase in  $\chi^2$ , but still gave a reasonable fit, fig. 4.11. However, this model, with a continuous chain, fig. 4.12, is a more sensible starting point for least squares refinement than that with the discontinuous chain.

If a proposed structure can be obtained which is a reasonable approximation to the actual structure, then the Rietveld method can be used to give a final refinement of the fit. This procedure was carried out on the structure obtained from the simulated annealing process using the package GSAS<sup>19</sup>. In this refinement, hydrogen atoms were placed in idealised tetrahedral sites with respect to the carbons in the chain. The

positions of these hydrogens were included in the refinement, resulting in a total of 16 atoms being considered during the refinement process. During the refinement, soft constraints were placed on certain bond distances and angles based on values obtained from the structure of  $\text{PEO}_3:\text{LiN}(\text{SO}_2\text{CF}_3)_2$  which are consistent with those of all known PEO:salt complexes of this nature. These soft constraints allow the constrained values to vary from the pre-set targets but with “penalties” in  $\chi^2$ , increasing in severity as the actual value differs further from the constrained value. Also, in contrast to the simulated annealing method employed to reach this point, constraints of this fashion force distances and angles to vary within a certain limit with all like distances and angles not necessarily being equal. This helps prevent an incorrect model based on possibly incorrect assumptions. Isotropic displacement factors were also constrained to be identical for “equivalent” atoms such as the carbons of the PEO chain, the oxygens of the triflate anion and the fluorines of the anion. Background intensities were introduced manually. This treatment resulted in 67 variables being varied during the refinement process. These include the crystallographic co-ordinates of the 16 atoms, 8 isotropic thermal factors, 4 lattice parameters, the 6 constituent variables of the pseudo-voigt peak shape function and the scale factor.

This refinement achieved a significant increase in quality of fit, fig. 4.13, and resulted in movements of the sodium positions as well as slight

variations in chain and triflate group placements, fig. 4.14. Despite the seemingly good fit, all further attempts to refine this model failed and a best  $\chi^2$  of 6 being achieved, with a significant misfit in the  $2\theta$  region of 35-45°. In addition to the poor match of observed and calculated patterns, there were significant reasons for doubt arising from chemical intuition. These included the fact that the sodium ions approached reasonably close (less than 2.5Å apart) which would incur strong Coulombic repulsion. Furthermore, one would expect the positive sodium ion to be co-ordinated by the most electronegative species, i.e. oxygen. However, the oxygens in both the chain and the triflate group lie away from the sodium with fluorines and electropositive carbons lying in co-ordinating positions with respect to the sodium, fig. 4.15. Additional evidence against this model is supplied by the fact that the amplitudes of the mean-square displacements for the oxygen atom in the polymer chain were imaginary.

An attempt was made to remedy this situation by swapping the positions of the SO<sub>3</sub> and CF<sub>3</sub> sections around on the triflate group and subjecting the model to further refinement. The resulting model, fig. 4.16, has a virtually identical fit, fig. 4.17, to the previous model. However, the neighbouring sodiums now lie further apart and they are co-ordinated by one of the oxygens of the triflate group. Despite this, attempts to further

refine this model failed and the mean-squared displacements also proved to be complex numbers for both the chain oxygen and carbons.

This situation, where there appears to be two solutions of reasonable fit but which both still appear to be imperfect is almost certainly indicative of a target  $\chi^2$  function which contains many local minima in crystallographic space. Thus, attempts to solve this structure using Rietveld refinement of a model estimated from existing, similar polymer salt complexes, even if the starting structure is quite reasonable, will probably end up refining around a false local minimum and thus yield an incorrect, misleading structure which would rule out attempts to solve the structure based on standard Rietveld refinement of a model based on other PEO:salt structures. This is, with hindsight, excellent justification for using the simulated annealing approach to solve this structure. This approach should be able to overcome the many local minima to seek out the global minimum. The reason that the first simulated annealing run failed to find this global minimum is probably due to the fact that there was not enough flexibility allowed in the triflate group, the most likely culprit being the averaging of the triflates internal bonds. This can be demonstrated in fig. 4.18 where the structures don't differ significantly apart from an averaging of bonds but the fit differs radically.

At this stage, it was decided to try a new simulated annealing run with the angles and distances in the triflate being independently varied. This represents a radically different approach to that which had been taken previously<sup>18</sup>. In this case, the number of assumptions used to speed up the simulated annealing process is minimised in order to achieve a better approximation to the global minimum in the figure of merit function. By introducing full flexibility to the triflate anion, the variables used to describe it vary from the first simulated annealing run employed in this work by replacing the unitary C-F bond length by three individual bond lengths C-F1, C-F2 and C-F3 and similarly for the S-O bond length, the C-S-O angle, the S-C-F angle, the O-S-O angle and the F-C-F angle. This run was carried out in similar fashion to the first SA run but with 37 variables being refined and the chain restrained to be continuous as in the second run. The starting model used was the best model from the previous refinement process. The initial temperature used was decreased to 2 in order to retain the gross features of the structural model. The number of moves made at a particular temperature,  $N_{\text{tot}}$  was 5000 and the temperature reduction factor,  $f_1$  was set to 0.1. After further Rietveld refinement the fit improved, fig. 4.19, with a  $\chi^2$  of 3.0, as well as better spacing of the sodium ions and better co-ordination by both chain and triflate oxygens, fig. 4.20. However, this latest model had the sodium ions still co-ordinated by the carbons of the chain rather than the oxygens as might be expected. This was tackled by reversing the order of the

atoms in the chain, i.e. swapping the oxygen and the terminal CH<sub>2</sub> unit, and refining with least-squares methods again. This final refinement gave an excellent fit, fig. 4.21, of  $\chi^2=1.1$  over the  $2\theta$  range of 8-85° with all mean-squared displacements being real numbers and in the relative magnitudes expected. Furthermore, the sodium is co-ordinated by six equidistant oxygens, two from the chain and four from surrounding triflate groups, figs. 4.22 and 4.23. In addition, there are no spurious approaches between atoms and the distances and angles are all reasonable. This excellent result leaves no question marks remaining over the quality of the final model.

#### **Section 4.4: Discussion and Conclusions**

The structure of the novel polymer electrolyte PEO:NaCF<sub>3</sub>SO<sub>3</sub> has been unambiguously found to be that shown in fig. 4.22. The PEO chain in this structure takes up a stretched tg<sub>2</sub>t $\bar{g}$ <sub>2</sub> conformation in which all C-C bonds take the gauche or anti-gauche conformation and all C-O bonds are either gauche, anti-gauche or trans. Similar conformations are adopted by the PEO chains of PEO:HgCl<sub>2</sub> and PEO:NaSCN, thus, the chain conformation appears to be a property of this salt concentration. This conformation is contrary to the case in complexes with a PEO:salt ratio of 3:1 or 4:1, where the polymer chain forms a helical arrangement.

This crystalline complex also exhibits six co-ordination of the sodium ions by oxygens, two from the same PEO chain and four from the triflate groups. The sodium ions are located in each turn of the zig-zag and share each ether oxygen with one other neighbour. There is some variation as to the co-ordination of sodium cations in PEO:salt complexes. The six co-ordination in this case is the same as that found in PEO:NaSCN and similar to PEO<sub>3</sub>:NaSCN except for the fact that in this case, co-ordination is achieved via four co-ordinating sites on the PEO chain and two from the salt species. In contrast, the Sodium cation in PEO<sub>3</sub>:NaClO<sub>4</sub> and PEO<sub>3</sub>:NaI is only five co-ordinated, with three co-ordinating sites belonging to the chain and two to the anion. The sodium co-ordination would therefore appear to be influenced by the anion species.

The reduced co-ordination of the positive ion by chain oxygens relative to the more dilute complexes could have some significance in the cationic conductivity. Likewise, the close proximity of the cation to the anion could represent an unfavourable situation for conductivity of the sodium ion, which could play a part in the poor conductance of these more concentrated materials at room temperature. Another factor in the poor conductance could be the extensive ionic cross-linking of the polymer chains. Whilst each cation is directly associated with only one PEO chain, each triflate anion is involved in the co-ordination of four sodium

ions, three of which are associated with one PEO chain whilst the fourth is associated with another chain. This provides  $\text{O}_{\text{PEO}}\text{-Na-O}_{\text{triflate}}\text{-S-O}_{\text{triflate}}\text{-Na-O}_{\text{PEO}2}$  linkages bridging two PEO chains. The most marked effect of this could be the increased melting temperature of this complex which is around 100-200°C higher than typical values<sup>20</sup> for complexes which have a PEO:salt ratio of 3 or 4:1.

This structure exhibits several local minima in its  $\chi^2$  function over crystallographic space. Such a situation can yield many misleading models with reasonable fits of calculated to experimental data. Thus, the structural solution of this compound represents a significant test for the simulated annealing algorithm. The structure was solved through taking a marked departure from previous attempts by allowing greater freedom and flexibility in the solution process instead of simplifying it. Attempts at solution of this structure by simple Rietveld refinement of a starting model based on previous structures are likely to be inadequate in this case. However, the simulated annealing approach used here still has its limitations that have been largely addressed with the independent varying of intra-triflate bond distances and angles. Despite this, the simulated annealing technique, while powerful and capable of solving structures from a completely ab-initio starting position, should not be regarded as a “turn the handle” technique. It has been shown that in this case, chemical

knowledge and intuition was still crucial in arriving at a sensible solution and in optimisation of the MC process.

#### Section 4.5: References

- [1] R.Frech, S.Chintapalli, P.G.Bruce, C.A.Vincent, *Chem. Commun.*, **2** (1997) 157
- [2] L.J.M.Sawers, D.P.Tunstall, P.G.Bruce, *Solid State Ionics*, **107** (1998) 13
- [3] R.Iwamoto, Y.Saito, H.Ishihara, H.Tadokoro, *J. Pol. Sci.*, **6** (1968) 1509
- [4] Y.G.Andreev, P.Lightfoot, P.G.Bruce, *J. Appl. Cryst.*, **30** (1997) 294
- [5] Y.Chatani, S.Okamura, *Polymer*, **28** (1987) 1815
- [6] Y.Chatani, Y.Fujii, T.Takayanagi, A.Honma, *Polymer*, **31** (1990) 2238
- [7] P.Lightfoot, M.A.Mehta, P.G.Bruce, *J. Mater. Chem.*, **2(4)** (1992) 379
- [8] P.Lightfoot, M.A.Mehta, P.G.Bruce, *Science*, **262** (1993) 883
- [9] P.Lightfoot, J.L.Nowinski, P.G.Bruce, *J. Am. Chem. Soc.*, **116** (1994) 7469
- [10] J.B.Thompson, P.Lightfoot, P.G.Bruce, *Solid State Ionics*, **85** (1996) 203
- [11] M.Yokoyama, H.Ishihara, R.Iwamoto, H.Tadokoro, *Macromolecules*, **2** (1969) 203
- [12] T.Hibma, *Solid State Ionics*, **9/10** (1983) 1101

- [13] S.Besner, A.Valeé, G.Bouchard, J.Prud'homme, *Macromolecules*, **25**, (1992) 6480
- [14] P-E.Werner, *Z. Kristallogr.*, **120** (1964) 375
- [15] P.M.DeWolff, *J. Appl. Cryst.*, **1** (1968) 108
- [16] A.LeBail, H.Duroy, J.L.Fourquet, *Mater. Res. Bull.*, **23** (1988) 447
- [17] Y.G.Andreev, T.Lundström, N.I.Sorokin, *Nucl. Instrum. Methods, Phys. Res. A*, **354** (1995) 134
- [18] W.H.Press, S.A.Teukolsky, W.T.Vetterling, B.P.Flannery, *Numerical Recipes in C: The Art of Scientific Computing*, Cambridge University Press (1992)
- [19] A.Larson, R.Von.Dreele, Los Alamos National Laboratory, LA-UR-86-748 (1987)
- [20] F.M.Gray, *Solid Polymer electrolytes – Fundamentals and Technological Applications*, VCH, New York (1991)

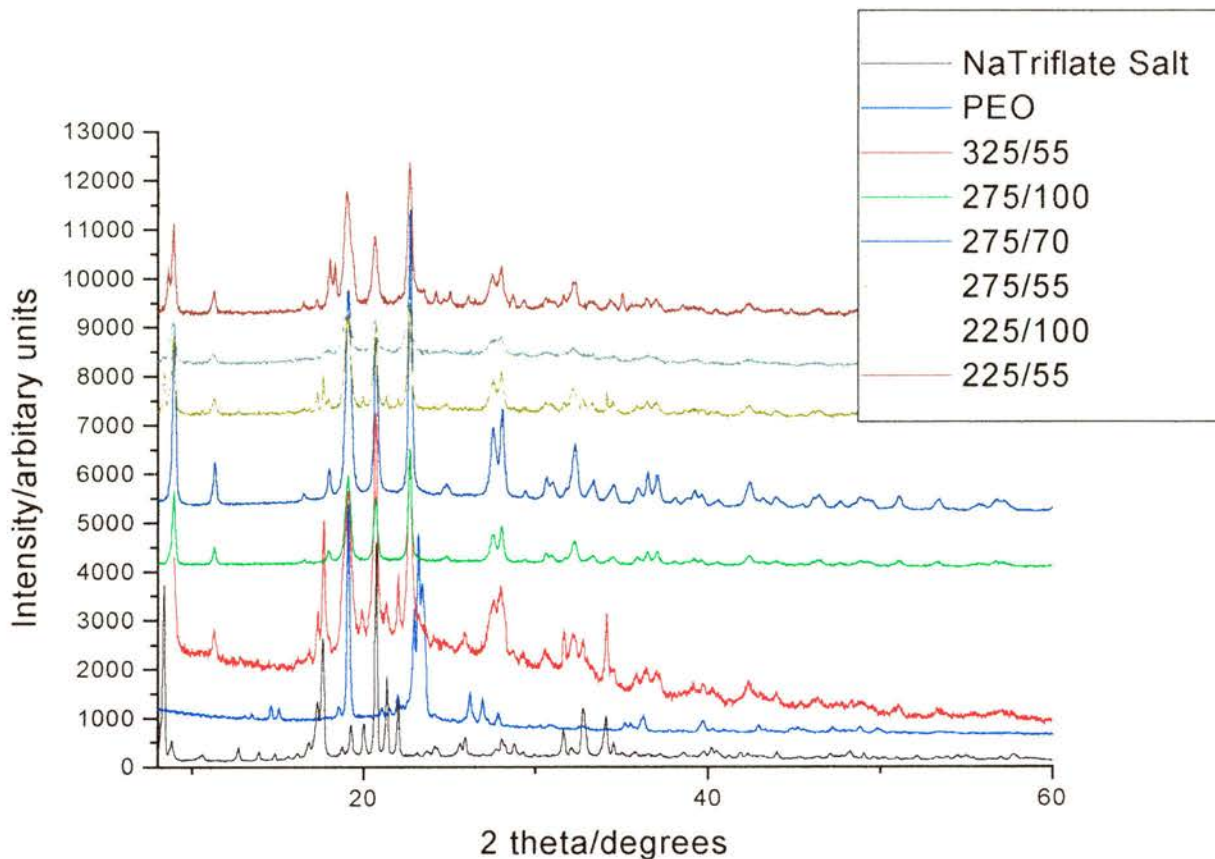


Fig. 4.1. Powder x-ray diffraction patterns taken of PEO:NaCF<sub>3</sub>SO<sub>3</sub> under varying thermal treatments. The first figure in the legend refers to the temperature of initial heating step, which was maintained for three hours. The second figure refers to the temperature of the second heating step, which was held for three days.

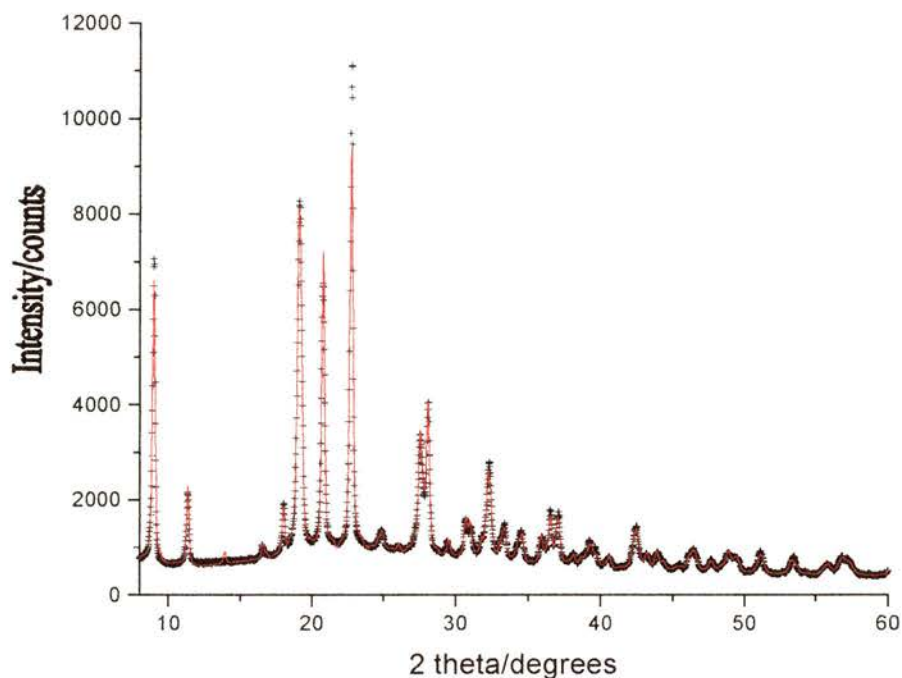


Fig. 4.2: A LeBail fit of the PEO:NaCF<sub>3</sub>SO<sub>3</sub> powder x-ray diffraction pattern based on the P2<sub>1</sub>/c spacegroup. The observed pattern is represented by the black crosses and the calculated pattern by the red line.

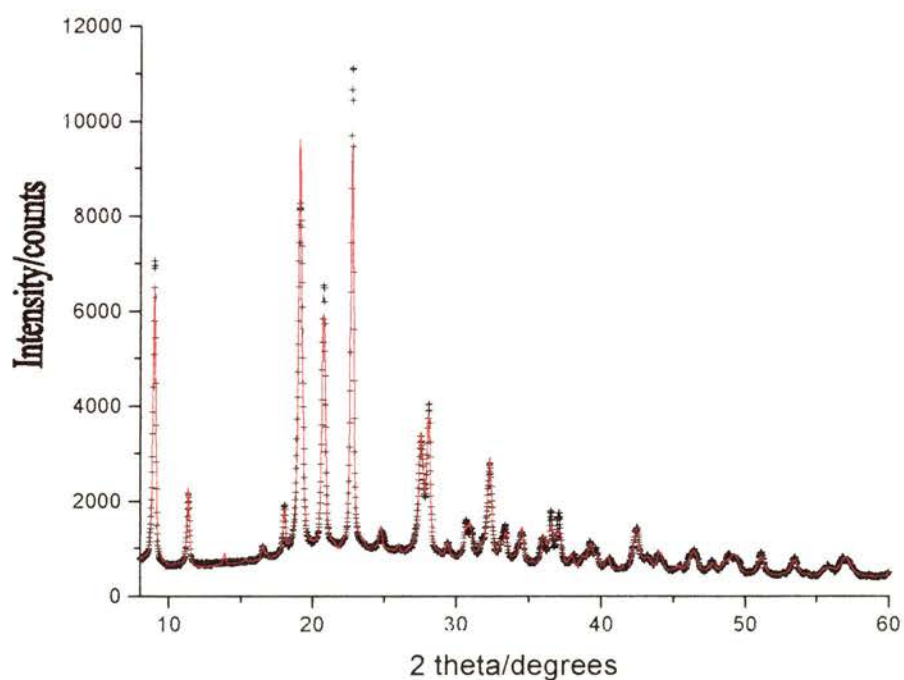


Fig.4.3: A LeBail fit of the PEO:NaCF<sub>3</sub>SO<sub>3</sub> powder x-ray diffraction pattern based on the P2mm spacegroup.

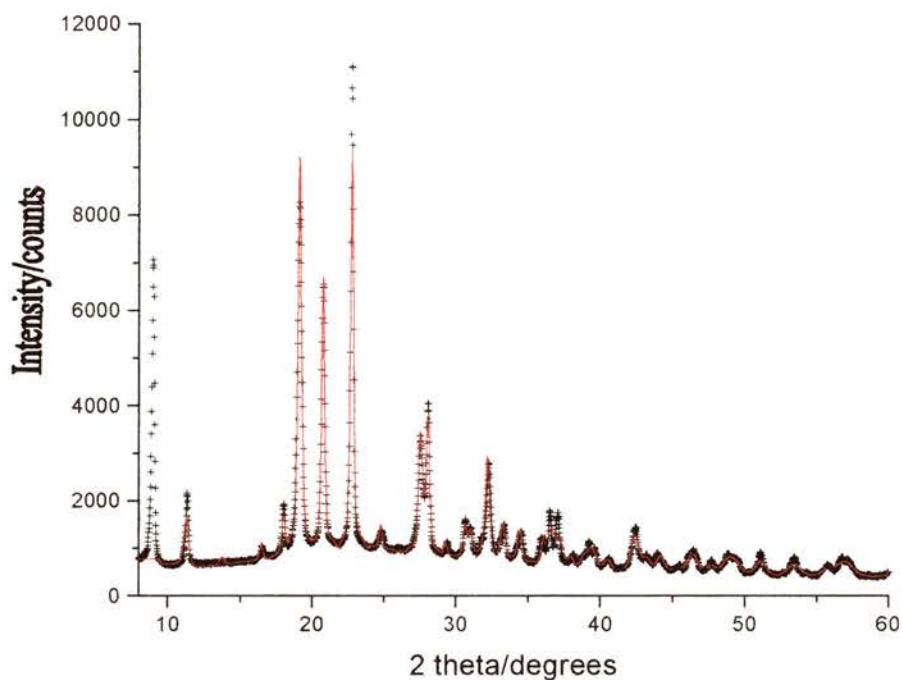


Fig. 4.4: A LeBial fit of the PEO:NaCF<sub>3</sub>SO<sub>3</sub> powder x-ray diffraction pattern based on the Pca2<sub>1</sub> spacegroup proposed for PEO:HgCl<sub>2</sub>.

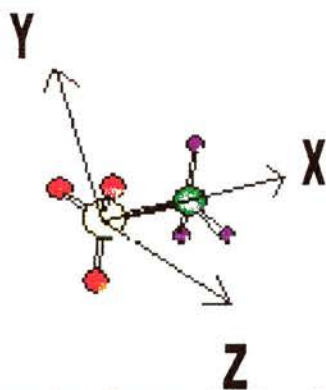


Fig. 4.5: Choice of Cartesian Frame for the Triflate Anion (Yellow: Sulphur, Green: Carbon, Red: Oxygen, Purple: Fluorine)

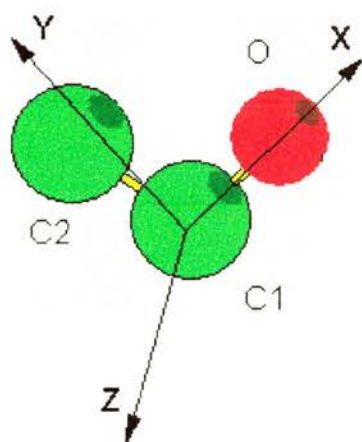


Fig.4.6: Choice of Local Cartesian Frame for the PEO Chain.

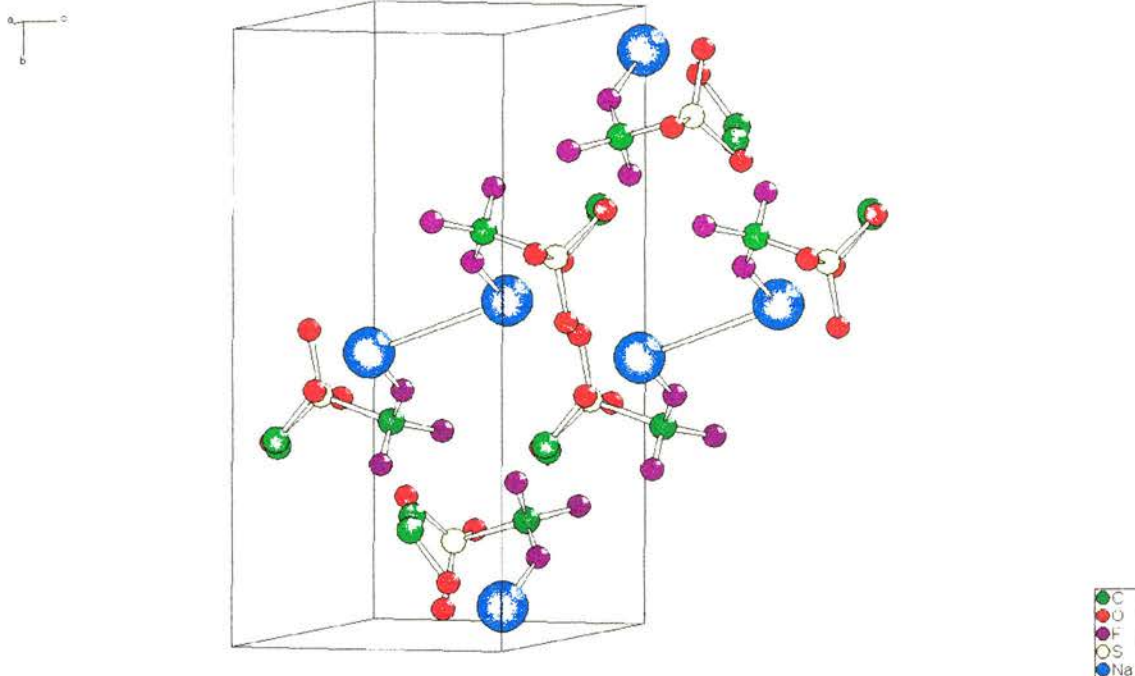


Fig.4.7: Randomised starting model for the first simulated annealing run.

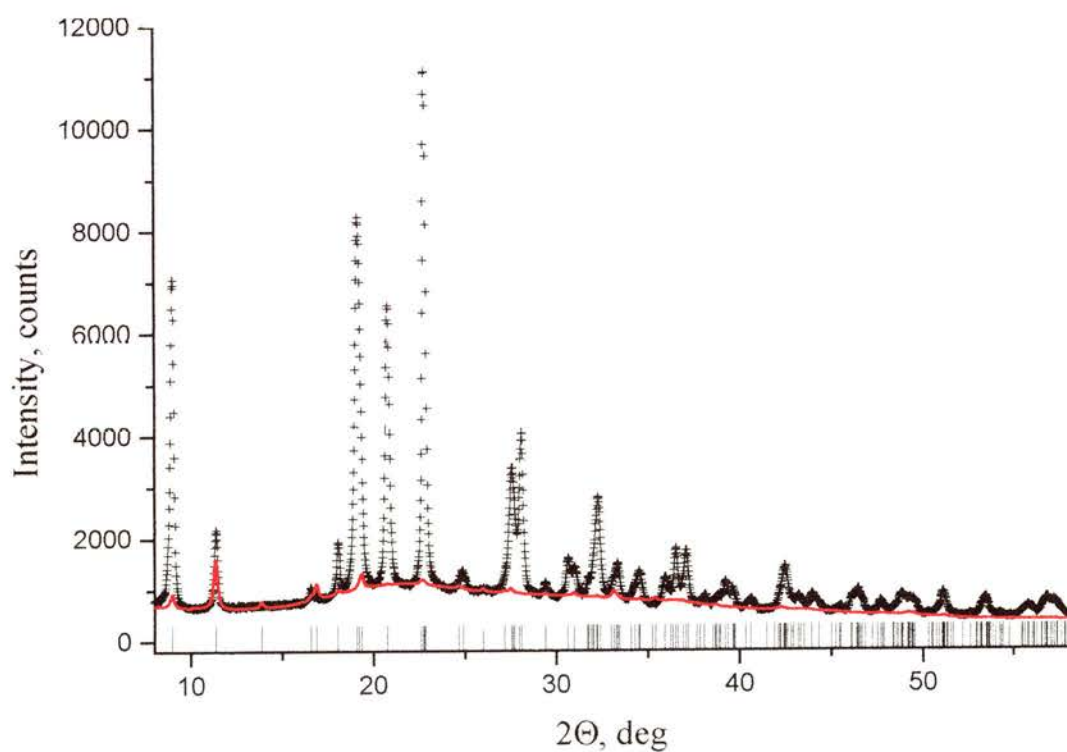


Fig.4.8: Fit of calculated diffraction pattern (red line) to experimental (black crosses) for the starting model for the first simulated annealing run.

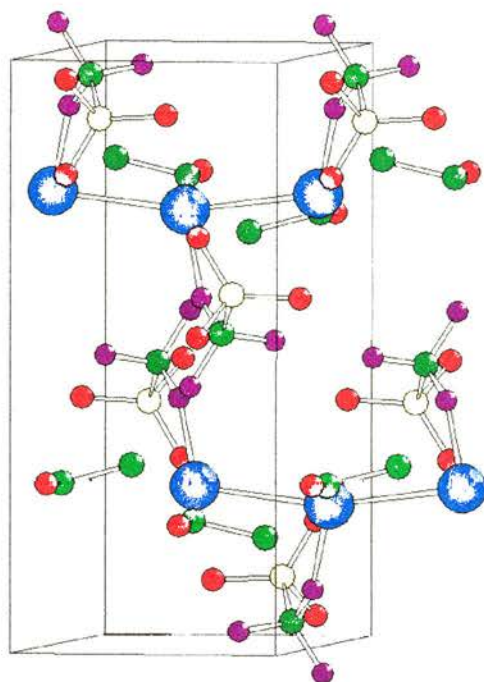


Fig.4.9: Final model from first simulated annealing run.

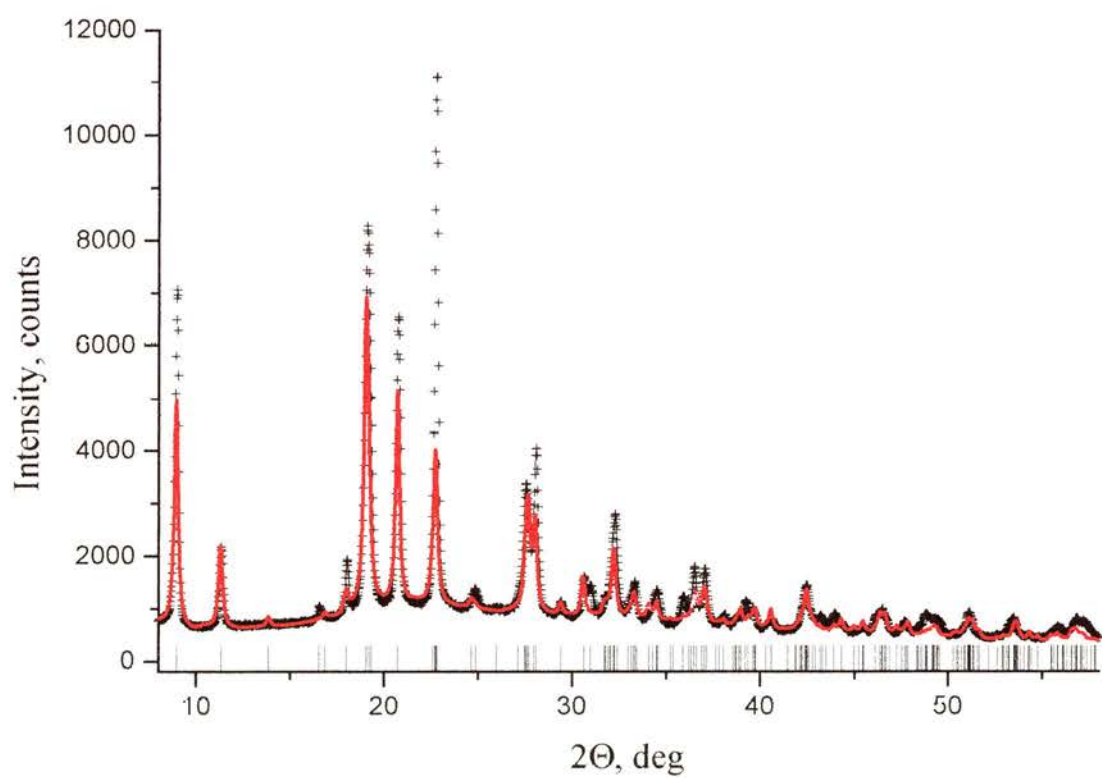


Fig.4.10: Final fit from the first simulated annealing run.

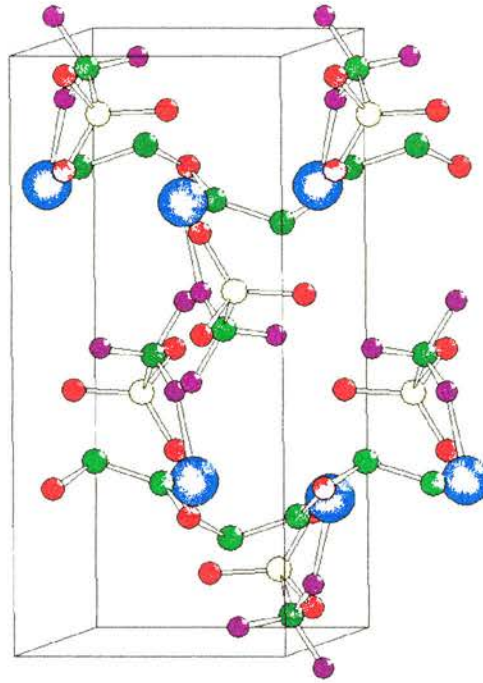


Fig.4.12: Final structural model from the second simulated annealing run.

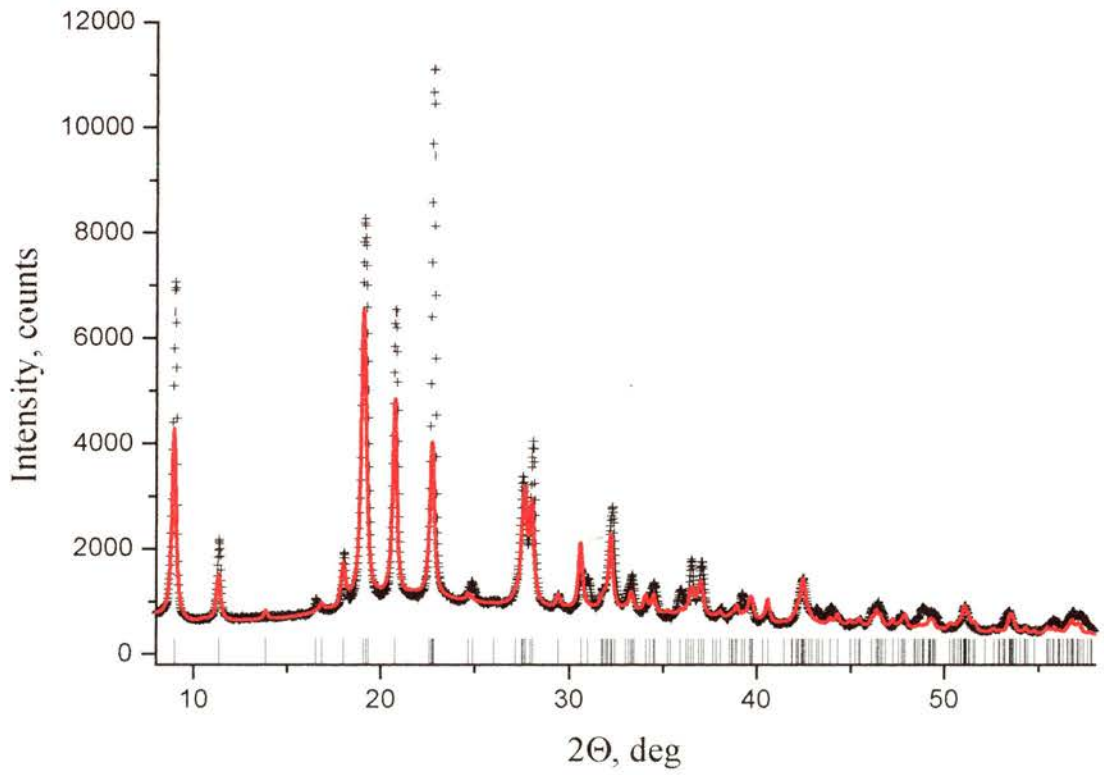


Fig.4.11: Final fit from the second simulated annealing run.

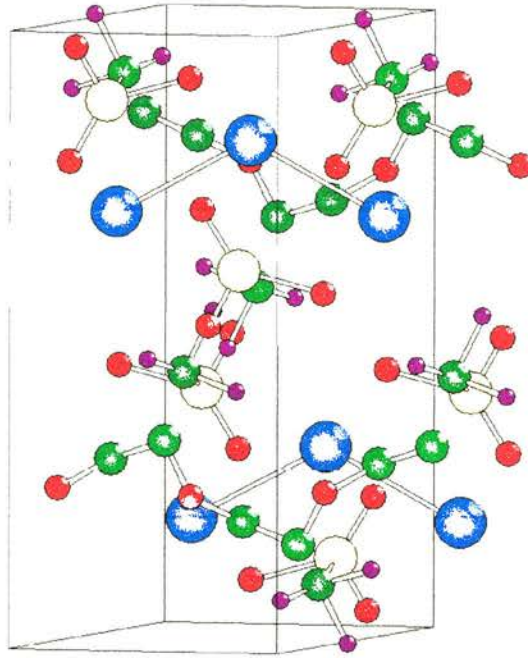


Fig.4.14: Final structural model after Rietveld refinement of the second simulated annealing model.

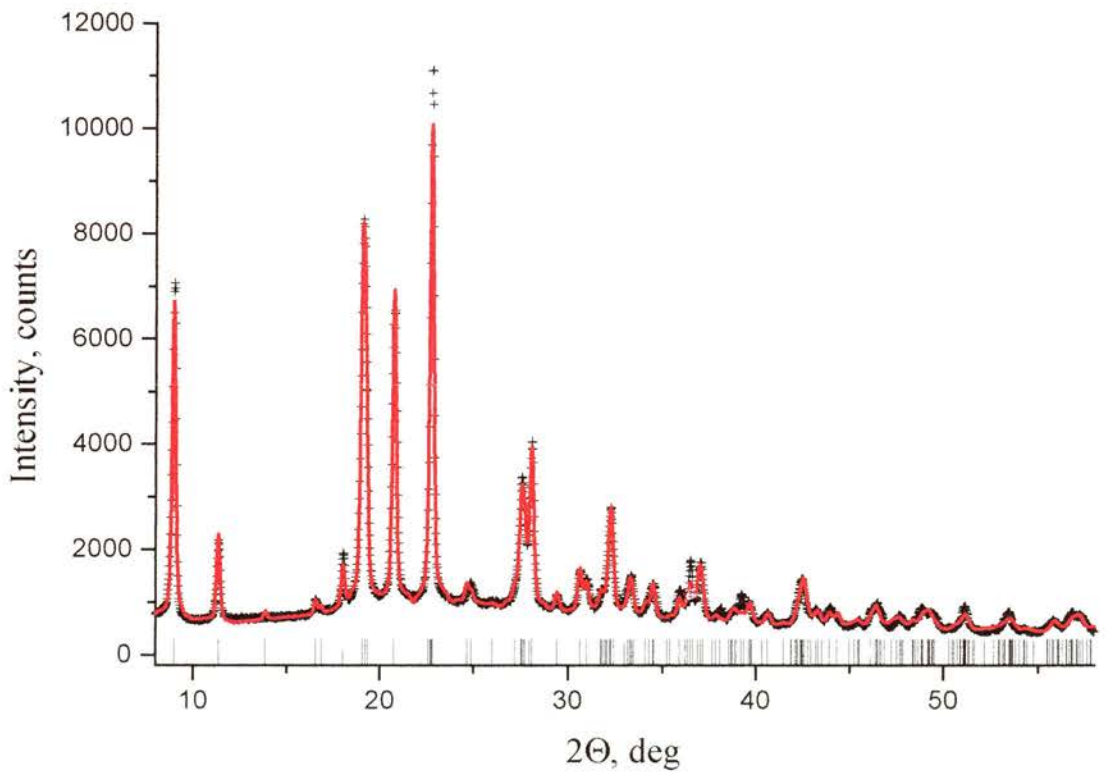


Fig.4.13: Fit after Rietveld refinement of the second simulated annealing model.

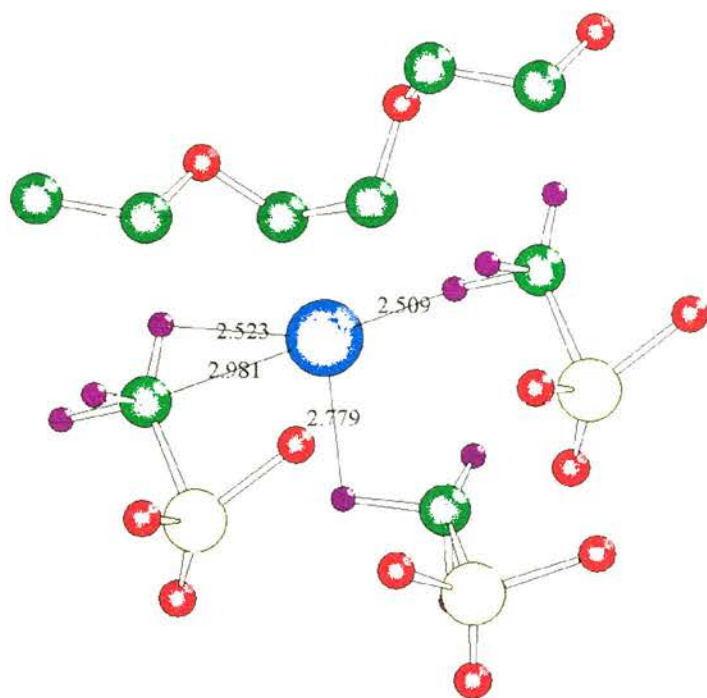


Fig.4.15: Coordination of the sodium ion after Rietveld refinement of the second simulated annealing model.

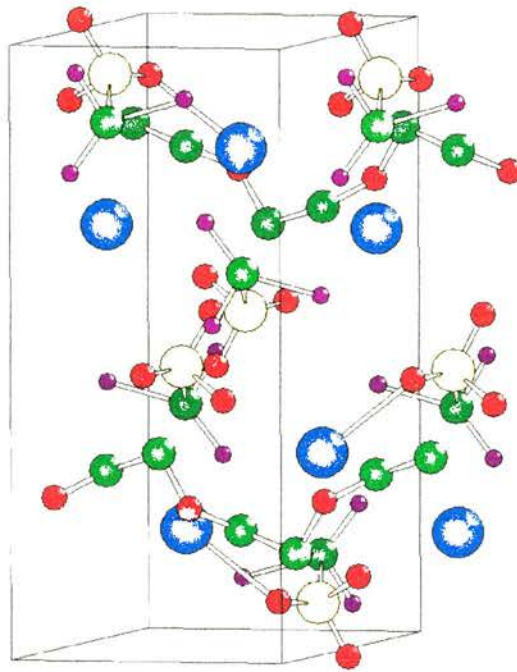


Fig 4.16: Structure after Rietveld refinement of a model with triflate anion inverted.

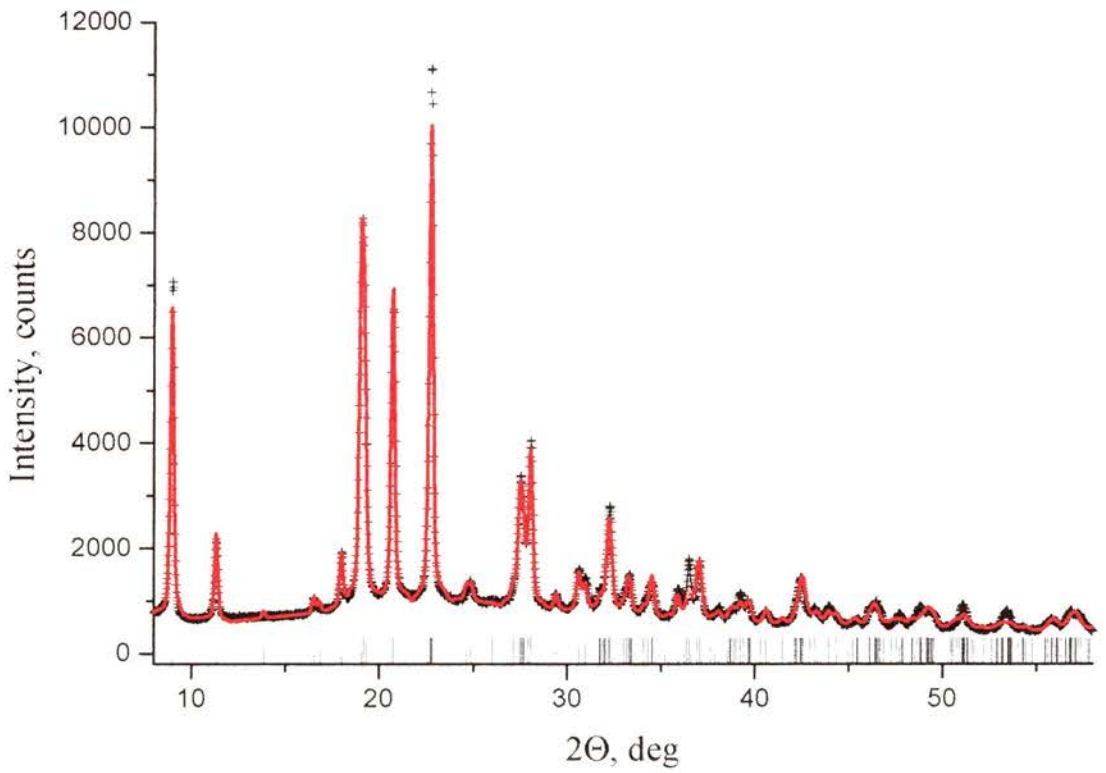


Fig.4.17: Fit after Rietveld refinement of a model with triflate anion inverted.

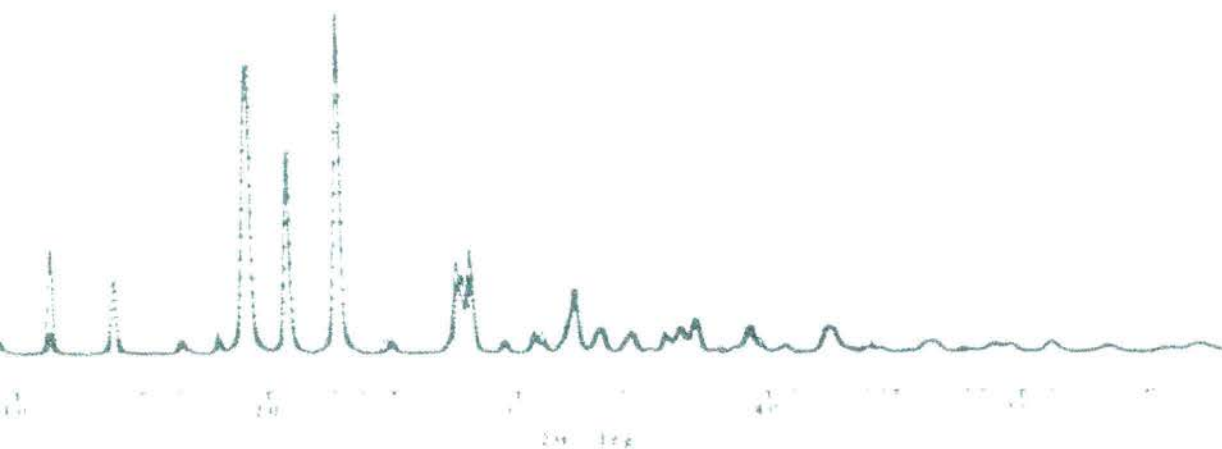


Fig. 4.18: Solid line – calculated pattern of the true structure of PEO:NaCF<sub>3</sub>SO<sub>3</sub>. Crosses – calculated pattern of PEO:NaCF<sub>3</sub>SO<sub>3</sub> structure modified by averaging all like bond lengths and angles in the triflate anion.

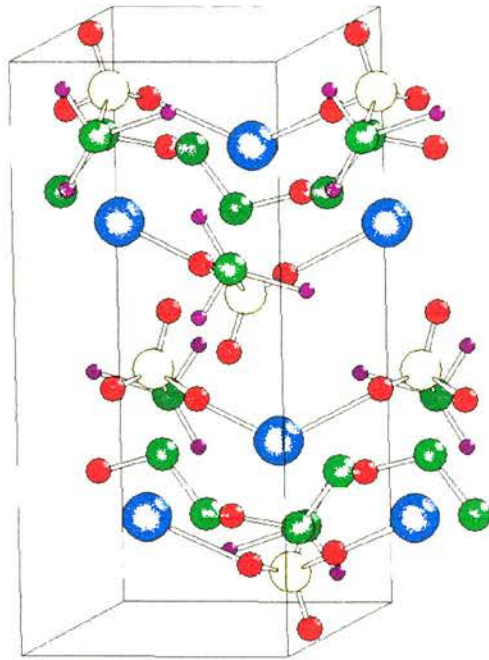


Fig. 4.20: Structure after Rietveld refinement of the model from the third simulated annealing run.

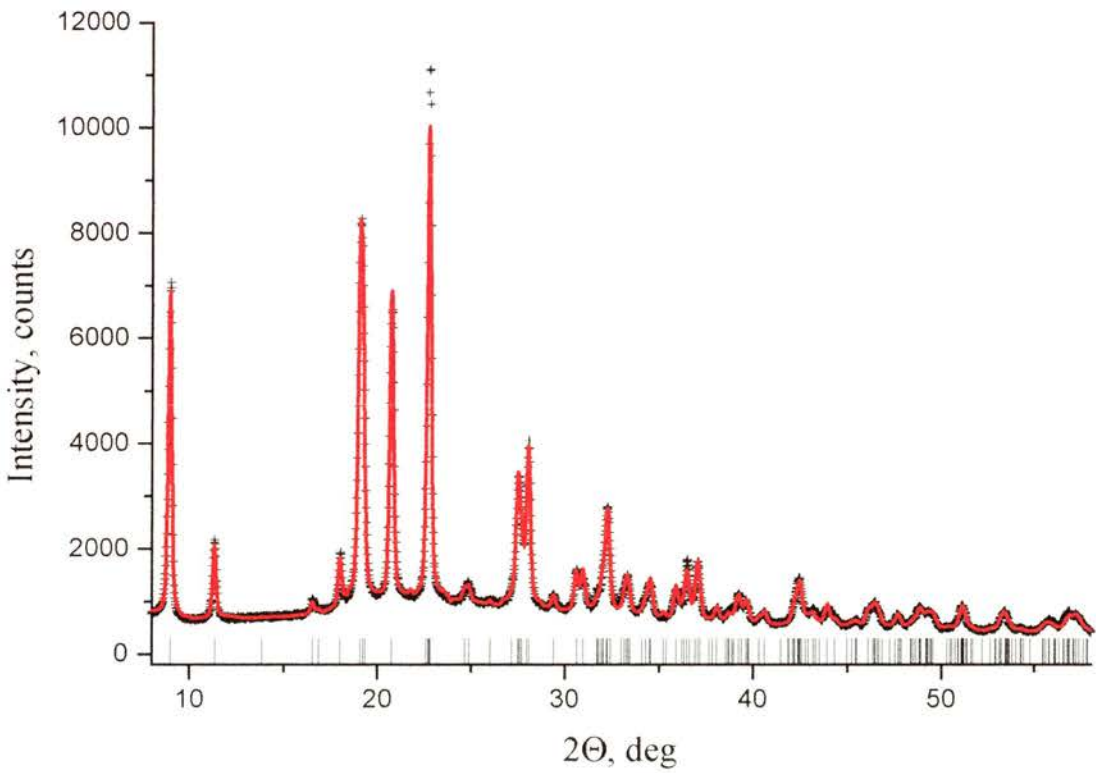


Fig. 4.19: Fit after Rietveld refinement of the model from the third simulated annealing run.

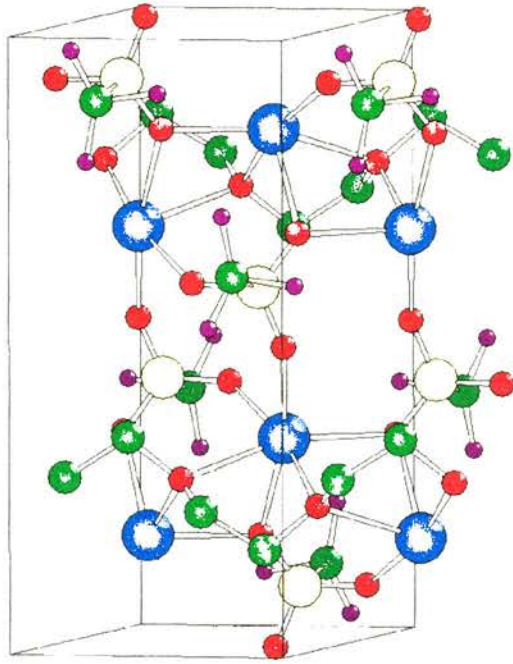


Fig. 4.22: Final Structure, obtained after Reitveld refinement of model with re-ordered chain.

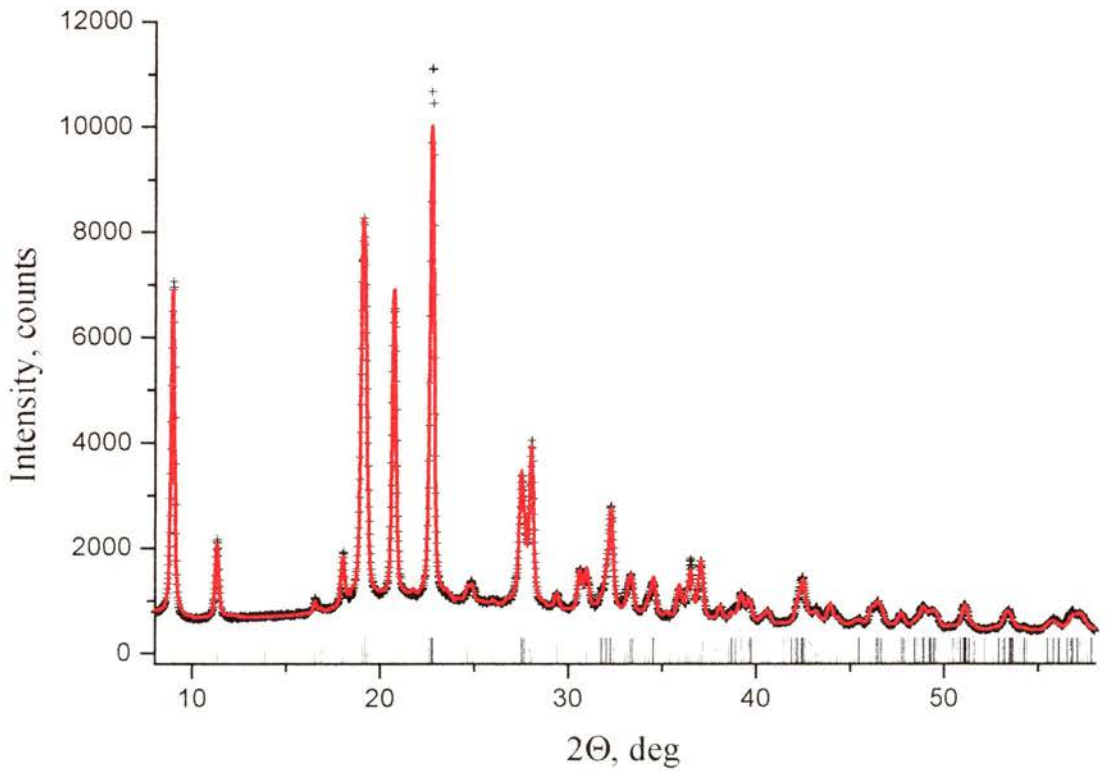


Fig. 4.21: The final fit.

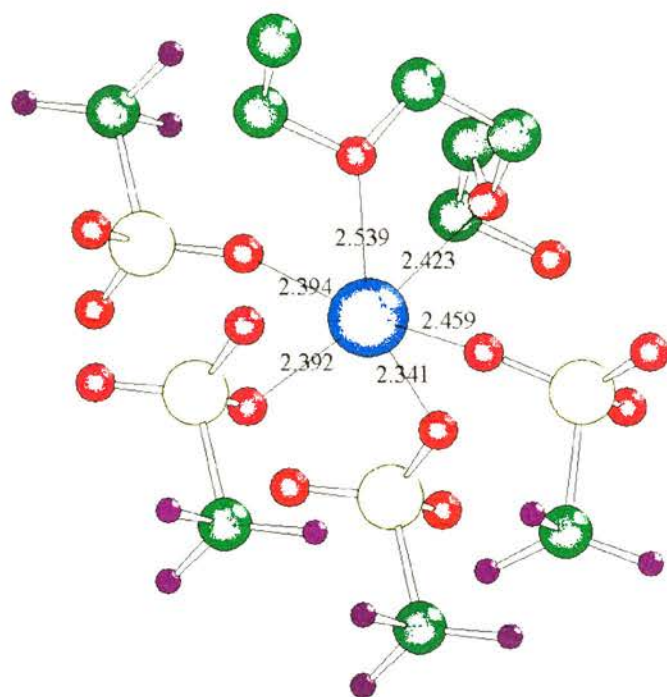


Fig. 4.23: Coordination of the sodium ions in the final structure.

**Table 4.1: Structural information for NaCF<sub>3</sub>SO<sub>3</sub>(C<sub>2</sub>H<sub>4</sub>O).**

Spacegroup: P21/c

a=9.8315(3)Å b=12.7526(4)Å c=5.7625(3)Å

 $\alpha=90^\circ$   $\beta=90.604(4)^\circ$   $\gamma=90^\circ$ Reduced  $\chi^2=2.636$  wRp=0.0504 Rp=0.0380R<sub>expected</sub>=0.031 No. of reflections to 60°=131

No. of structural parameters varied in least squares=60

No. of parameters varied in Monte-Carlo=37

Atom	x	Y	z	U
TRIFLATE				
S(1)	0.6624(8)	0.0824(7)	0.253(2)	0.040(3)
C(1)	0.856(2)	0.109(2)	0.251(4)	0.06(1)
F(1)	0.910(1)	0.026(1)	0.187(3)	0.058(3)
F(2)	0.886(1)	0.207(1)	0.227(3)	0.058(3)
F(3)	0.868(1)	0.095(1)	0.484(2)	0.058(3)
O(1)	0.638(1)	-0.016(1)	0.332(2)	0.067(4)
O(2)	0.603(1)	0.167(1)	0.370(3)	0.067(4)
O(3)	0.646(1)	0.086(1)	0.003(3)	0.067(4)
Na(1)	0.4966(8)	0.3298(7)	0.2313(2)	0.056(4)
CHAIN				
O(4)	0.3235(8)	0.230(1)	0.027(3)	0.017(6)
C(2)	0.2703(8)	0.1597(1)	0.196(3)	0.018(6)
C(3)	0.2134(8)	0.223(1)	0.400(2)	0.018(6)
H(1)	0.200(5)	0.118(3)	0.123(7)	0.088
H(2)	0.336(5)	0.113(4)	0.246(8)	0.088
H(3)	0.165(5)	0.280(3)	0.346(8)	0.088
H(4)	0.173(5)	0.176(4)	0.504(7)	0.088

**SELECTED DISTANCES**

S1 - C1	1.933(6)	Triflate Oxygens	O4 - C2	1.429(4)	
		Na - O1'	2.392(6)	O4 - C3'	1.429(5)
S1 - O1	1.360(4)	Na - O2	2.458(7)		
S1 - O2	1.401(4)	Na - O2'	2.34(1)	C2 - H1	0.96(3)
S1 - O3	1.446(7)	Na - O3'	2.390(9)	C2 - H2	0.92(3)
				C3 - H3	0.92(2)
C1 - F1	1.240(3)	Chain Oxygens	C3 - H4	0.94(3)	
C1 - F2	1.289(4)	Na - O4	2.420(9)		
C1 - F3	1.361(6)	Na - O5'	2.54(1)	C2 - C3	1.539(5)

**SELECTED BOND ANGLES**

C1 - S1 - O1	109.90(1)	F1 - C1 - F2	133.89(2)	C2 - C1 - H1	110.85(3)
C1 - S1 - O2	109.36(2)	F1 - C1 - F3	98.68(2)	C2 - C1 - H2	110.69(3)
C1 - S1 - O3	095.12(4)	F2 - C1 - F3	102.17(1)	C1 - C2 - H3	110.05(3)
				C1 - C2 - H4	107.95(3)
O1 - S1 - O2	118.37(3)	O4 - C2 - C3	109.25(3)		
O1 - S1 - O3	110.04(1)	O4 - C3' - C2'	109.31(3)	H1 - C2 - H2	106.38(3)
O2 - S1 - O3	114.37(2)	C3' - O4 - C2	109.29(3)	H3 - C3 - H4	120.03(2)
S1 - C1 - F1	106.07(2)	O4 - C2 - H1	108.53(3)		
S1 - C1 - F2	113.42(0)	O4 - C2 - H2	111.10(3)		
S1 - C1 - F3	092.76(4)	O4 - C3' - H3'	103.31(3)		
		O4 - C3' - H4'	105.69(3)		

**TORSION ANGLES**

O4 - C2 - C3 - O4'	69.99376	g
C2 - C3 - O4' - C2'	-171.97985	t
C3 - O4' - C2' - C3'	-75.82929	-g
O4' - C2' - C3' - O4''	-69.99376	-g
C2' - C3' - O4'' - C2''	171.97985	t
C3' - O4'' - C2'' - C3''	75.82929	g

## Chapter 5: The Structure Determination of PEO:KCF<sub>3</sub>SO<sub>3</sub> From Powder X-ray Diffraction Data

### Section 5.1: Introduction

It is clear that salt concentration plays a large part in determining the conformation of the polymer chain in PEO:salt complexes<sup>1-3</sup>. This has been extensively studied in complexes with a PEO repeat salt ratio of 3:1<sup>1,4-7</sup> and 4:1<sup>8,9</sup>. Of special interest is the study of the effect of varying only the cationic species<sup>8,9</sup>. It was found that in the case of several compounds of the type PEO<sub>4</sub>:MSCN, where M is the variable cationic species, the gross features of the structure, such as chain conformation, remain similar but that subtle features such as the cationic co-ordination change. In addition, it has been found that the co-ordination of sodium ions in PEO:salt compounds can vary depending on the salt concentration and anionic species<sup>1,2,4,6</sup>. It is in this spirit that structural solution of PEO:KCF<sub>3</sub>SO<sub>3</sub> was undertaken. This work expands on the previous structural solution of PEO:NaCF<sub>3</sub>SO<sub>3</sub> in that it can provide further insight into the relatively understudied compounds with an EO to salt ration of 1:1, providing the first solution of a compound of this type with a potassium cation and only the second PEO:salt crystal structure solved containing potassium. This allows comparison with other 1:1 compounds and also comparison of the potassium co-ordination with that of PEO<sub>4</sub>:KSCN.

## Section 5.2: Phase Corroboration

For the structure determination process to be successful, it is necessary to accurately know the contents of the asymmetric unit. In PEO:salt complexes, this includes knowing the PEO to salt ratio. Some doubt has been expressed as to the phase diagram<sup>10</sup> of PEO:KCF<sub>3</sub>SO<sub>3</sub>. For PEO:salt complexes more dilute in salt, in general those involving smaller cations such as sodium and lithium form complexes of a 3:1 ratio whereas larger cations such as potassium, ammonia and rubidium form 4:1 complexes. One of the driving forces for this is the need to impose the number of ether oxygens around these large cations in order to satisfy their co-ordination requirements. This demands a change in the PEO chain conformation compared with the 3:1 complexes to produce a wider, fatter helix. It is possible that the larger potassium ion could have a similar effect of forcing changes in the PEO chain conformation relative to sodium in these more concentrated systems. In order to check the composition of the PEO<sub>x</sub>:KCF<sub>3</sub>SO<sub>3</sub> complex, samples with PEO:salt ratios of 0.5:1, 1:1, 2:1, 3:1, 4:1, 5:1 and 6:1 were prepared in similar fashion to the preparation of PEO:NaCF<sub>3</sub>SO<sub>3</sub> described in chapter 4.2. Powder x-ray diffraction patterns were taken for each composition, fig. 5.1.

From these, it is clear that there is only one complex present. This complex is clearly responsible for the major peaks present in the diffraction patterns arising from the complexes with a PEO:salt ratio of

0.5:1, 1:1 and 2:1. Thus, the complex must lie in this range of compositions, which does not contradict the findings of Besner et al.<sup>10</sup> that the complex has a PEO:salt ration of 1:1. Thus it was assumed that the complex does indeed have this composition and that this would be vindicated by the structural solution of the complex. The samples containing a higher PEO concentration, i.e. 3:1 to 6:1 contained peaks belonging to the complex in addition to peaks characteristic of pure PEO.

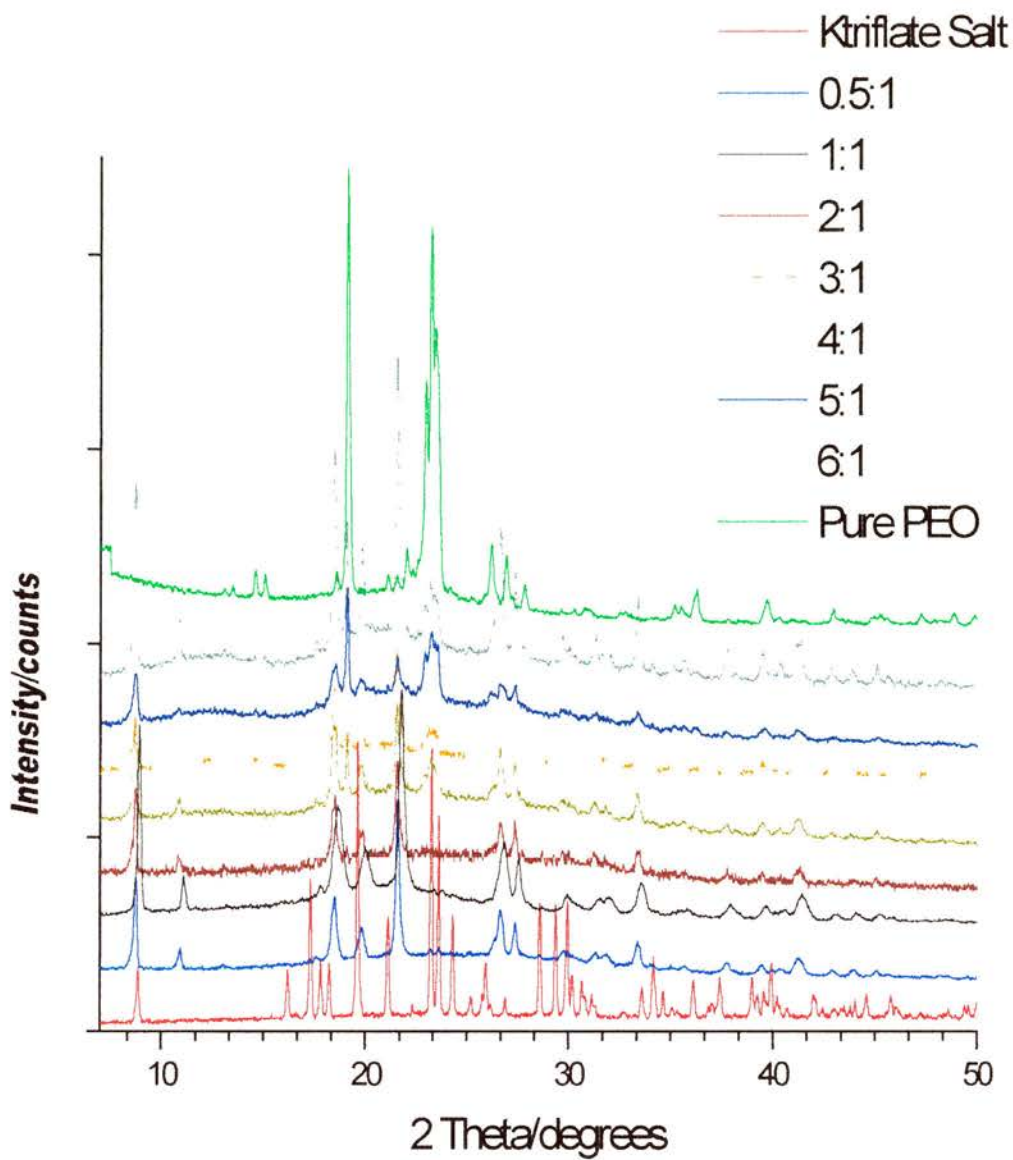


Fig.5.1. Powder x-ray diffraction patterns taken from a series of PEO:KCF<sub>3</sub>SO<sub>3</sub> complexes with PEO:salt ratio as indicated.

### Section 5.3: Experimental details

The PEO:KCF<sub>3</sub>SO<sub>3</sub> complex was synthesised in a similar fashion to PEO:NaCF<sub>3</sub>SO<sub>3</sub> as discussed in section 4.2. The only difference being a slightly lower melting temperature of 240°C for 4 hours. The powder x-ray diffraction pattern, fig. 5.2, was collected on a STOE stadi/p powder diffractometer in transmission mode with Cu-K $\alpha$ <sub>1</sub> radiation. The data was collected at room temperature in the data range 5° < 2 $\theta$  < 60° in 0.02° steps over a period of 16 hours.

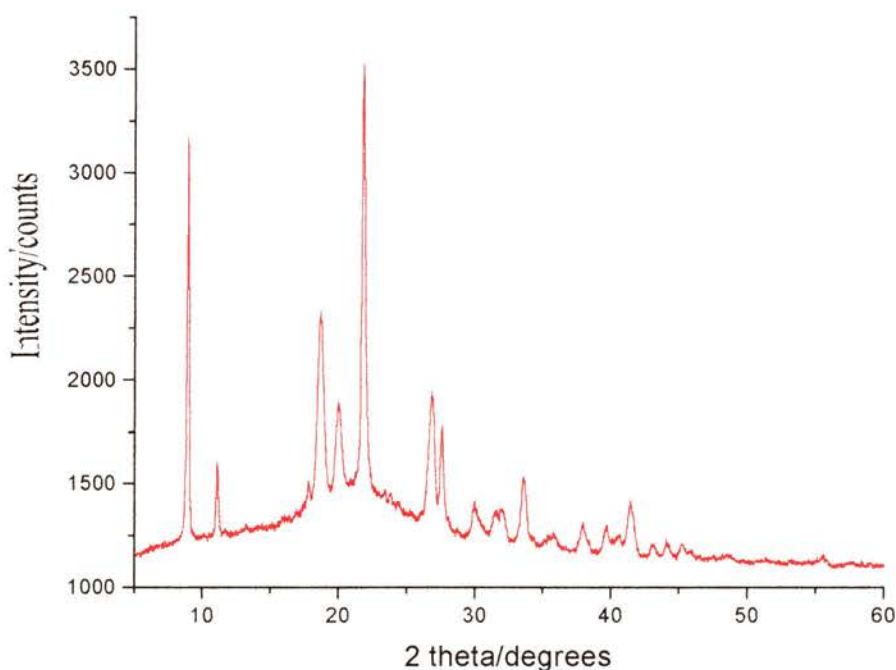


Fig. 5.2: The Powder X-ray diffraction pattern of PEO:KCF<sub>3</sub>SO<sub>3</sub>.

Preliminary inspection of the powder x-ray diffraction pattern suggested a close resemblance to that of PEO:NaCF<sub>3</sub>SO<sub>3</sub><sup>2</sup> and so the CPSR<sup>11</sup> package was used to adjust the PEO:NaCF<sub>3</sub>SO<sub>3</sub> cell to fit the new data.

This yielded a slightly larger cell than in the case of PEO:NaCF<sub>3</sub>SO<sub>3</sub> with dimensions of  $a=9.981(1)$ ,  $b=13.436(2)$ ,  $c=5.933(1)$  and  $\beta=89.28(1)$ . This was corroborated using the indexing program TREOR<sup>12</sup>. This cell is reasonable given the greater size of the potassium ion, with an ionic radius of 1.38Å against that of 1.02Å for sodium. The space group was determined to be P2<sub>1</sub>/c on the basis of systematic absences. Given that the two compounds have identical space groups, similar unit cells and similar diffraction patterns, it was decided to carry out the structural determination of PEO:KCF<sub>3</sub>SO<sub>3</sub> by Rietveld refinement using the structure of PEO:NaCF<sub>3</sub>SO<sub>3</sub> but placed into the larger unit cell as the starting model.

Soft restraints were employed during the refinement. This involved placing soft restraints based on values obtained from PEO:NaCF<sub>3</sub>SO<sub>3</sub> on such parameters as the bond lengths and angles in the PEO chain and the CF<sub>3</sub>SO<sub>3</sub><sup>-</sup> moiety, giving a total of 39 soft restraints. No torsion angles were restrained. Thermal factors were constrained to be identical for similar atoms such as the oxygens of triflate anion, the triflate fluorines as well as the carbons and hydrogens of the PEO chain. A total of 66 parameters were varied in the refinement process including the crystallographic co-ordinates of the 16 atoms, thermal factors, scale factor, lattice parameters and profile parameters.

The refinement converged in a straightforward fashion, producing a final structure, fig. 5.3 and table 5.1, which gave a good fit to the experimental diffraction pattern, fig. 5.4, having a  $\chi^2=1.94$ . All the bond lengths and angles were within reasonable limits based on those found in other PEO:salt complexes, table 5.1.

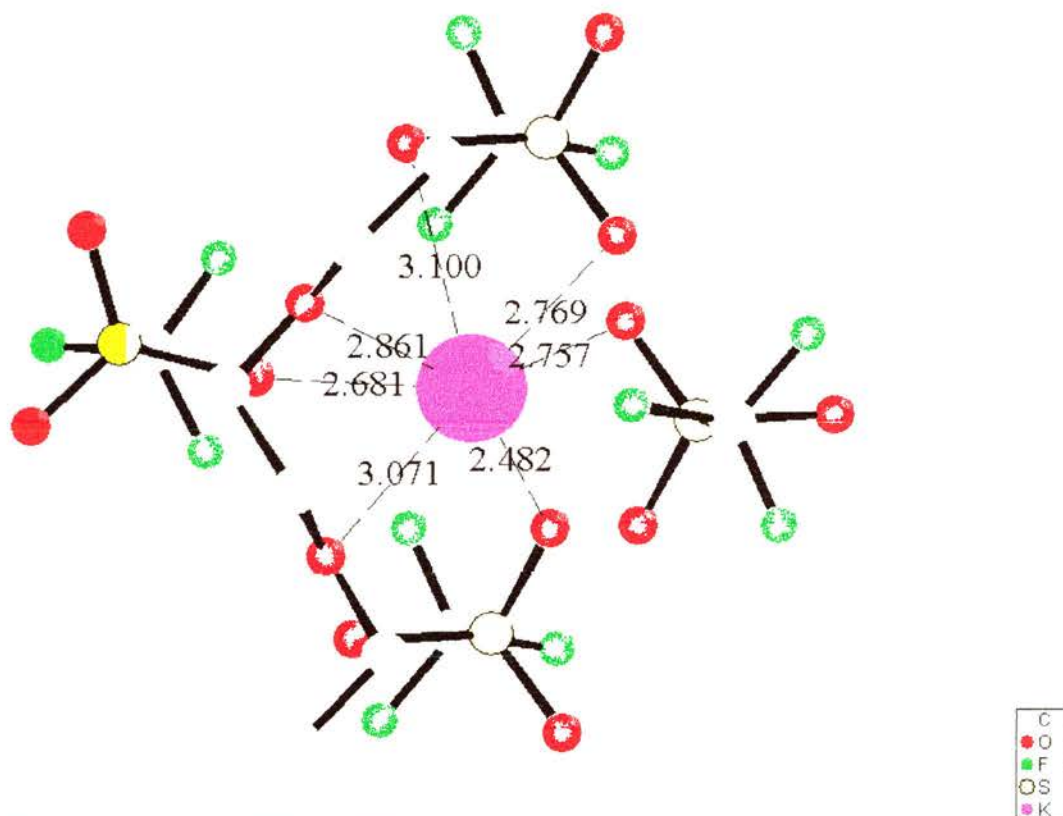


Fig.5.3: Final structure of PEO:KCF<sub>3</sub>SO<sub>3</sub> after refinement with bond lengths to coordinating atoms shown.

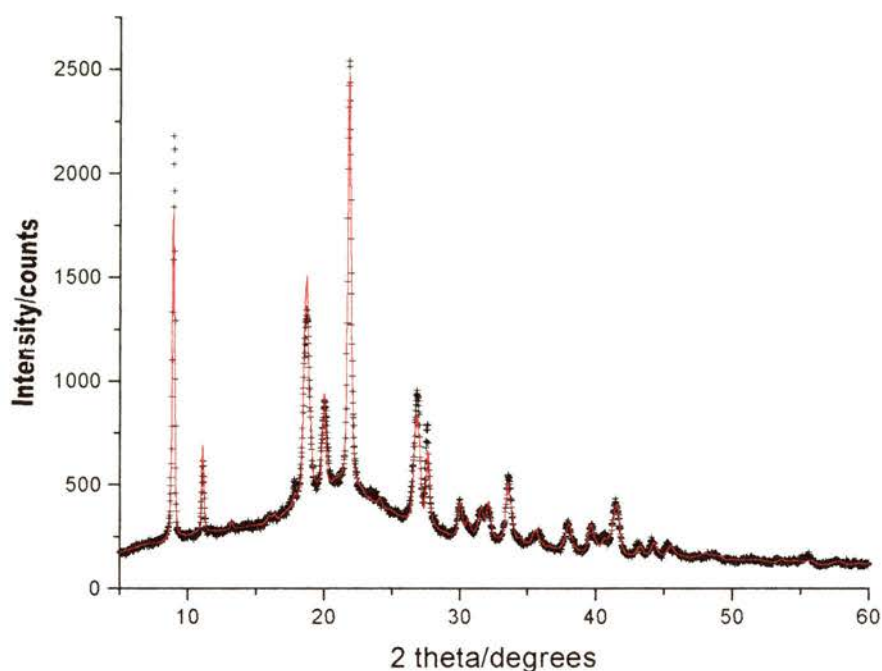


Figure 5.4: Final fit after refinement. The experimental pattern is represented by black crosses, the calculated patterns is represented by the red line.

#### Section 5.4: Discussion

As can be seen from fig.5.5, the chain adopts a stretched  $t_2gt_2\bar{g}$  zigzag conformation which is typical of PEO:salt compounds with an EO to salt ratio of 1:1<sup>1-2,13</sup>. Similarly, the cations are located in each turn of the zigzag and are directly associated with one PEO chain only.

Each potassium cation is seven coordinated by oxygens, two ether oxygens from the PEO chain and five oxygens from four separate triflate groups. This differs from the cation coordination in PEO:NaCF<sub>3</sub>SO<sub>3</sub> in which the smaller sodium ion is coordinated by six oxygens. The greater coordination in the potassium analogue is achieved via a slight rotation of

of a triflate anion such that one of the four anions co-ordinating the  $\text{Na}^+$  ion is associated via two oxygens in the case of  $\text{K}^+$  instead of just one. The co-ordination number of seven is consistent with the potassium co-ordination in the only other potassium:polymer compound solved to date, namely  $\text{PEO}_4:\text{KSCN}^8$ . However, in the 4:1 compound, the co-ordination is achieved through five ether oxygens and two nitrogens from the thiocyanate group. The greater co-ordination by the PEO chain in  $\text{PEO}_4:\text{KSCN}$  is possible due to its helical conformation and it is interesting that the space in the potassium ions co-ordination sphere vacated by the PEO chain is filled by anions such that the total co-ordination is unchanged.

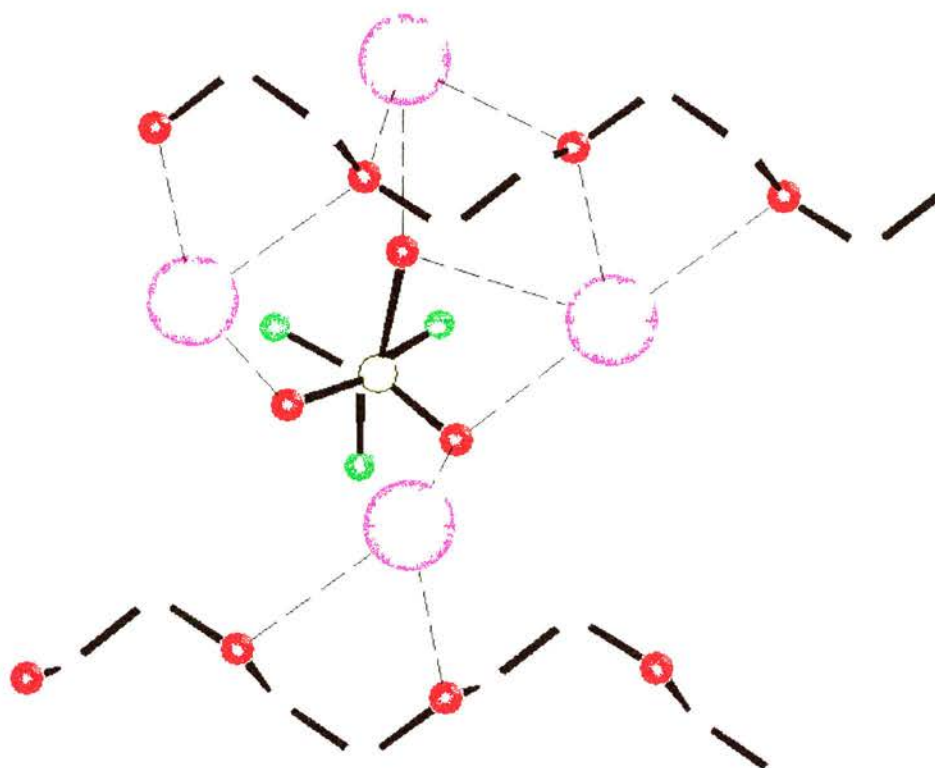


Figure 5.5: Final structure of PEO:KCF<sub>3</sub>SO<sub>3</sub> showing the zig-zag conformation of the PEO chain. Atom colourings as in Fig. 5.3, coordination bonds are shown as hatched lines.

This greater concentration of anions in the cationic coordination sphere of the 1:1 complex has the consequence that there is necessarily increased coordination of anions by cations. This in turn leads to ionic cross-links between PEO chains caused by one triflate coordinating two cations, each associated with a different polymer chain. Thus, the compound can be considered to be a three dimensional interlinked material as opposed to the one dimensional tunnels formed by more dilute PEO:salt compounds. The ionic cross linking could be one reason for the relatively high melting point of this compound, 275°C<sup>10</sup>, compared with PEO<sub>4</sub>:KSCN, 95°C. In addition, it could be hypothesized that the increased cross-linking via ionic bridges will retard the conduction of the

cations due to reduction in the segmental motion of the chains in the amorphous state.

The triflate anions are each co-ordinated by four potassium ions. Three of the co-ordinating cations are associated with the same polymer chain whilst the other completes the ionic cross-link by being associated with another PEO chain. Of the three oxygens belonging to the  $-\text{SO}_3$  moiety of the triflate anion, one co-ordinates two cations, one co-ordinates the same cation twice and the third singly co-ordinates one cation. This formation of two co-ordination bonds from the one triflate ion to the same cation is a feature not found in other PEO:triflate salt compounds whose structures have been solved so far<sup>3,5</sup>. This is probably due to the increased size of the potassium ion compared with that of sodium or lithium.

To summarise, the chain conformation appears to be typical for compounds with a PEO:salt ratio of 1:1. However, the cation co-ordination appears to differ depending on the cation species and in the case of potassium appears to be consistent throughout the PEO:potassium salt compounds solved so far, regardless of salt concentration. This is in contrast to the co-ordination of the sodium ion, which varies between five and six. In addition, this co-ordination is achieved largely through the triflate anions. This is a consequence of the

chain conformation, which is such that it does not envelop the cation and sterically cannot bring sufficient oxygens into the cation's co-ordinating sphere. A feature of this compound, in common with the other 1:1 compounds is the ionic cross-links between PEO chains. This could be a factor in the increased melting point and lower conductivity of this class of compound relative to those in which the salt is more dilute.

## Section 5.5: References

- [1] Y.Chatani, Y.Fujii, T.Takayanagi, A.Honma, *Polymer*, **21** (1990) 2238
- [2] Y.G.Andreev, G.S.MacGlashan, P.G.Bruce, *Phys. Rev. B*, **55** (1997) 12011
- [3] P.G.Bruce, S.A.Campbell, P.Lightfoot, M.A.Mehta, *Solid State Ionics*, **78** (1995) 191
- [4] Y.Chatani, S.Okamura, *Polymer*, **28** (1987) 1815
- [5] P.Lightfoot, M.A.Mehta, P.G.Bruce, *Science*, **262** (1993) 883
- [6] P.Lightfoot, M.A.Mehta, P.G.Bruce, *J. Mater. Chem.*, **2(4)** (1992) 379
- [7] Y.G.Andreev, P.Lightfoot, P.G.Bruce, *Chem. Commun.*, (1996) 2169
- [8] P.Lightfoot, J.L.Nowinski, P.G.Bruce, *J. Am. Chem. Soc.*, **116** (1994) 7469
- [9] J.B.Thomson, P.Lightfoot, P.G.Bruce, *Solid State Ionics*, **85** (1996) 203
- [10] S.Besner, A.Valeé, G.Bouchard, J.Prud'homme, *Macromolecules*, **25** (1992) 134
- [11] Y.G.Andreev, T.Lundström, N.I.Sorokin, *Nucl. Instr. And Meth. In Phys. Res.*, **A354** (1995) 134
- [12] P.-E. Werner, L.Eriksson, M.Westdahl, *J. Appl. Cryst.*, **18** (1985) 367

- [13] M.Yokoyama, H.Ishihara, R.Iwamoto, H.Tadokoro,  
*Macromolecules*, **2** (1969) 184

**Table 5.1. Structural and Refinement Data for KCF<sub>3</sub>SO<sub>3</sub>(C<sub>2</sub>H<sub>4</sub>O)**Spacegroup: P2<sub>1</sub>/c

a=9.981(1)Å, b=13.436(2)Å, c=5.933(1)Å, β=89.28(1)°

Reduced χ<sup>2</sup>=1.94

Weighted R profile = 0.079, R profile = 0.060

No. of structural parameters varied in least squares=60

No. of variables in refinement=66

No. of reflections=250

No. of soft constraints=39

Atom	x	y	z	U
TRIFLATE				
K(1)	0.527(1)	0.382(1)	0.252(3)	0.066(4)
S(1)	0.6930(9)	0.0760(8)	0.252(3)	0.20(1)
C(1)	0.879(1)	0.106(1)	0.277(3)	0.04(2)
F(1)	0.939(2)	0.016(1)	0.295(5)	0.142(8)
F(2)	0.910(2)	0.155(2)	0.083(3)	0.142(8)
F(3)	0.885(2)	0.162(2)	0.468(3)	0.142(8)
O(1)	0.663(2)	0.006(3)	0.431(5)	0.16(1)
O(2)	0.622(2)	0.169(1)	0.285(8)	0.16(1)
O(3)	0.675(2)	0.036(3)	0.029(4)	0.16(1)
CHAIN				
O(4)	0.351(2)	0.229(3)	0.098(5)	0.06(2)
C(2)	0.298(2)	0.1686(5)	0.277(9)	0.04(2)
C(3)	0.242(2)	0.237(3)	0.464(5)	0.04(2)
H(1)	0.227(3)	0.130(2)	0.22(1)	0.088*
H(2)	0.366(3)	0.128(2)	0.33(1)	0.088*
H(3)	0.182(3)	0.203(6)	0.559(7)	0.088*
H(4)	0.202(4)	0.294(3)	0.398(7)	0.088*

\*Fixed During refinement

**SELECTED DISTANCES**

S1 - C1	1.909(8)	Triflate Oxygens	O4 - C2	1.429(7)
		K - O1	O4 - C3	1.430(5)
S1 - O1	1.444(9)	K - O1		
S1 - O2	1.450(9)	K - O2	C2 - H1	0.95(1)
S1 - O3	1.442(9)	K - O2	C2 - H2	0.94(1)
		K - O3		
			C3 - H3	0.94(1)
C1 - F1	1.361(8)	Chain Oxygens	C3 - H4	0.95(1)
C1 - F2	1.353(8)	K - O4		
C1 - F3	1.357(8)	K - O4	C2 - C3	1.538(7)

**SELECTED BOND ANGLES**

C1 - S1 - O1 106.1(7)	F1 - C1 - F2 113.3(9)	C2 - C1 - H1 109.7(13)
C1 - S1 - O2 106.1(7)	F1 - C1 - F3 113.5(9)	C2 - C1 - H2 111.1(13)
C1 - S1 - O3 106.5(7)	F2 - C1 - F3 115.9(9)	C1 - C2 - H3 111.3(13)
		C1 - C2 - H4 109.5(13)
O1 - S1 - O2 111.1(8)	O4 - C2 - C3 109.0(6)	
O1 - S1 - O3 114.0(8)	O4 - C3' - C2' 109.0(6)	H1 - C2 - H2 111.0(15)
O2 - S1 - O3 112.4(9)	C3' - O4 - C2 108.6(6)	H3 - C3 - H4 111.4(15)
S1 - C1 - F1 104.1(7)	O4 - C2 - H1 107.4(13)	
S1 - C1 - F2 104.4(7)	O4 - C2 - H2 108.6(13)	
S1 - C1 - F3 103.9(7)	O4 - C3' - H3' 107.5(13)	
	O4 - C3' - H4' 111.3(13)	

**TORSION ANGLES**

O4 -C2 -C3 -O4'	-80.24	-g
C2 -C3 -O4' -C2'	-177.72	t
C3 -O4' -C2' -C3'	79.44	g
O4' -C2' -C3' -O4''	80.24	g
C2' -C3' -O4'' -C2''	177.72	t
C3' -O4'' -C2'' -C3''	-79.44	-g

## Chapter 6: The Ab-Initio Structure Solution of $\text{PEO}_6\text{:LiAsF}_6$ from Powder X-Ray and Neutron Diffraction Data

### Section 6.1: Introduction

As described in chapter 2, the PEO chain conformation is greatly influenced by the salt concentration. The PEO chain of compounds with a PEO:salt ratio of 1:1 has a zig-zag conformation whilst the polymer chain of the more dilute 3:1 and 4:1 compounds is helical. In addition to the formation of crystalline structures with PEO:salt ratios of 1:1, 3:1 and 4:1, another relatively common salt concentration for PEO:salt crystalline phases is 6:1. A structural study of this class of PEO:salt compound could be interesting in that it will answer the question of whether there is further variation of PEO chain conformation with salt concentration. In addition, PEO:salt compounds have maximum conductivity<sup>1</sup> when the PEO:salt ratio is in the region of 6:1 to 16:1. Thus, it is of great interest to see if this change in conductivity is accompanied or influenced in some way by structural variations.

Structural solution of  $\text{PEO}_6\text{:LiAsF}_6$  would provide this insight into the structural behaviour of these 6:1 systems and allow a comparison of structural variation with salt concentration, being the most dilute structure to have been solved to date. It would also be the first structural solution of a PEO complex with a hexafluoroarsenate salt.

However, the field of ab-initio structure solution from powder diffraction is still in its infancy relative to single crystal techniques, as detailed in chapter 2. The use of powder diffraction data is still difficult and most solutions of molecular structures involving similar large numbers of atoms from powder data tend to involve a significant use of rigid bodies, which adopt well-documented conformations such as aromatic rings. The complexity of the structural solution of PEO<sub>6</sub>:LiAsF<sub>6</sub> arises not only from the number of atoms, in this case 26 in the solution stage, but also from the large degree of flexibility, with a fully flexible polymer chain, involving 15 torsion angles in the refinement process, leading to a total of 79 parameters being varied. This complexity is compounded by the fact that no structure of a PEO<sub>6</sub>:salt complex has ever been determined before, so few pre-suppositions can be made in order to aid the solution process. With this in mind, it was decided to employ the simulated annealing method<sup>2,3</sup> for the structural solution process since this technique has been successfully used to solve the structures of other PEO:salt systems<sup>4,5</sup>.

## **Section 6.2: Experimental Details**

The presence of water in the sample can have significant effects on the crystallinity of PEO:salt compounds<sup>6</sup>, especially when the salt is water sensitive, as is the case with Lithium hexafluoroarsenate. To prevent this,

PEO (Aldrich) was dried under dynamic vacuum at 60°C and lithium hexafluoroarsenate (Aldrich) was dried under dynamic vacuum at 120°C, both for three days, before being transferred to an argon filled glove box. The dried PEO and lithium hexafluoroarsenate were mixed together in the appropriate quantities and sealed into a cryogrinding pot, along with a selection of metal ball bearings. This was then placed in a bath of liquid nitrogen in order to transfer the sample into a frozen, brittle state before being shaken vigorously for 30 minutes. The resulting finely ground mixture was then used to fill 0.7mm diameter, special glass Lindemann tubes whilst in an argon atmosphere. These were sealed using silicone sealant. For the best crystallisation, as long as there is no degenerative effect on either the salt or polymer, it is best to heat samples in the region of the melting point before annealing below the melting point<sup>7</sup>. After consulting the phase diagram<sup>8,9</sup>, it was decided to heat the sample at 120°C for four hours before annealing at 65°C for 7 days in order to promote crystallisation.

The sample used for the neutron diffraction experiment was prepared in a similar way, except that deuterated PEO (Polymer Source) was used and a 5mm-diameter vanadium can was used in place of the glass Lindemann tube. The vanadium can was sealed using a bolt on cap made airtight with poly(tetrafluoroethylene) washers and tape. The can was pre-dried by heating under vacuum at 70°C for 3 days. To further protect the

sample whilst outside the glovebox, the can/sample was stored whenever possible in a pre-dried, argon filled, screw top jar which had been sealed using PTFE film.

The powder x-ray diffraction data were collected in the data range  $5^\circ < 2\theta < 60^\circ$  in  $0.02^\circ$  steps over a period of sixteen hours on a Stoe Darmstadt Stadi/p high-resolution x-ray laboratory powder diffractometer, using  $\text{Cu K}\alpha_1$  radiation and a small angle, position sensitive detector.

The powder neutron diffraction data were collected on the OSIRIS diffractometer of the ISIS pulsed neutron source at the Rutherford Appleton Laboratory with the help of instrument scientists David Martin and Dennis Engberg. The data were collected at room temperature in the range of 1.34 - 9.17Å in d-space over a period of eighteen hours. The data were binned and analysed using the openGENIE package.

### **Section 6.3: The Structure Solution Process**

Indexing of the powder x-ray diffraction pattern was carried out using the TREOR90 package<sup>10</sup> which yielded only one choice of unit cell, with  $a=11.871(4)\text{Å}$ ,  $b=17.5373(3)\text{Å}$ ,  $c=9.228(3)\text{Å}$  and  $\beta=108.21(1)^\circ$ . This cell had a De-Wolff figure of merit<sup>11</sup> of 12. The space group was determined on the basis of systematic absences to be  $P2_1/a$ . This cell was checked to be plausible through use of a LeBail fit<sup>12</sup>, which fitted well with a  $\chi^2$  of

1.59. In addition, with the assumption that there are four formula units in the unit cell, the density would be  $1.67\text{gcm}^{-3}$ , which is consistent with other, similar compounds. Thus, it is probable that all the atoms in the unit cell occupy  $4e$  general positions.

The customised simulated annealing program specifically for  $\text{PEO}_6:\text{LiAsF}_6$  was written using Microsoft Visual C++ on a dual 100MHz Pentium PC. The calculated diffraction intensities and pattern-profile calculation were carried out using code modified from the public domain software package CPSR<sup>13</sup>. The routines<sup>14</sup> RAN3 and IRBIT1 were used to generate random numbers and random bits respectively.

The simulated annealing procedure used was very similar to that employed in the solution of  $\text{PEO}:\text{NaCF}_3\text{SO}_3$  detailed in chapter 4. Using the lessons learned from this previous structure solution in which the final structure could not be obtained until full flexibility of the molecular fragments was introduced, all bond lengths and angles were allowed to vary independently. In this structural solution, the contents of the asymmetric unit were partitioned into three fragments, namely, the lithium cation, the  $\text{AsF}_6^-$  anion and the PEO chain,  $(-\text{CCO}-)_6$ , the last two being defined using their own Cartesian frames. Whilst the lithium could be adequately described using its crystallographic co-ordinates, the other fragments required the use of geometric descriptions.

The anion was placed using the crystallographic co-ordinates of the arsenic atom, whose current position also served as the origin of the Cartesian frame. The x-axis of the Cartesian frame was described as lying along the bond between the arsenic atom and the first fluorine. The y-axis of the Cartesian frame was defined as lying at right angles to the x-axis and in the plane formed by the arsenic and the first and second fluorines. The z-axis was placed so as to make up a right handed orthogonal set, fig. 6.1. The remaining fluorines were placed using the rotation operator, ch.3.2, on the second fluorine. Thus, the  $\text{AsF}_6^-$  fragment can be described using 21 parameters, namely the three crystallographic co-ordinates of the arsenic atom, the 3 Euler angles, 6 As-F bond lengths and 9 F-As-F bond angles.

The origin atom of the PEO chain was chosen to be the last but one atom in the chain, i.e. carbon number eleven. The Cartesian frame for the PEO chain was defined as having its x-axis along the direction of the bond between the origin atom and the adjacent oxygen, i.e. the  $\text{C}^{11}\text{-O}^6$  bond. The y-axis was defined as being at right angles to the x-axis and in the plane of the last three atoms in the chain, i.e.  $\text{O}^6$ ,  $\text{C}^{11}$  and  $\text{C}^{12}$ . The z-axis was placed so as to form a right handed orthogonal set, fig. 6.2. Using this formulation, the  $\text{O}^6$  atom can be placed trivially using the  $\text{C}^{11}\text{-O}^6$  bond length and the  $\text{C}^{12}$  atom through simple geometry involving the  $\text{C}^{11}\text{-C}^{12}$

bond length and the C<sup>12</sup>-C<sup>11</sup>-O<sup>6</sup> bond angle. The rest of the atoms in the chain can then be placed through the chain formula, ch.3.2. This leads to a geometrical description involving 54 variables, including, 17 bond lengths, 16 bond angles, 15 torsion angles, the 3 crystallographic coordinates of the penultimate carbon and the three Euler angles which describe the orientation of the fragment in space.

In order to consider only chemically plausible structural models, a system of hard constraints was employed. These only allowed the bond lengths and angles to vary within a range that was determined from examination of typical values of the parameters from a database of solved structures. In addition, the origin of each local Cartesian frame was kept within the limits of the asymmetric unit. Furthermore, checks were made in order to prevent two AsF<sub>6</sub><sup>-</sup> groups approaching to a distance that was less than 80% of the sum of the Van der Waals radii of the appropriate atoms.

The starting model, fig. 6.3, was chosen randomly and the fit to the experimental pattern (3,650 data points and 1,130 reflections) was clearly poor, fig. 6.4 with a  $\chi^2$  of 184. The total number of moves at a particular temperature,  $N_{\text{tot}}$ , was set to 5000; the initial "temperature" ( $\Delta\chi^2_{\text{cur}}$ ) set to 5 and the temperature reduction factor,  $f_1$ , was 0.1. These settings allow a significant number of uphill steps in the  $\chi^2$  function at the early stages of minimisation with a slow reduction in the temperature. This is in order to

ensure the greatest probability of the simulated annealing algorithm finishing in the region of the global minimum. A total of 79 parameters were varied using the simulated annealing method, including 25 bond angles, 23 bond lengths, 15 torsion angles, 9 crystallographic coordinates, 6 Eulerian angles and the overall displacement.

Application of the simulated annealing algorithm resulted in a rapid drop in  $\chi^2$ , fig. 6.5, finally converging to a reasonable fit, fig. 6.6, with a  $\chi^2$  of 16. As can be seen from fig. 6.7, there was a considerable change in the structure from the random starting model. At this stage of the solution process, the polymer chains are very close to being continuous and the most striking observation is that the final model appears to have two PEO chains in close proximity. The two chains are mirror images of each other as a consequence of the  $x,y,z$  and  $-x,-y,-z$  operators of the  $P2_1/a$  spacegroup and they would appear to form a tunnel structure down the  $a$ -axis. The  $AsF_6$  anions align themselves linearly parallel to the polymer tunnels in the interchain space.

It is obvious that this arrangement, with discontinuous polymer chains is not chemically plausible. To remedy this, another S.A. run was carried out in similar fashion to the previous run but instead of starting from a random starting configuration, the final model from the previous run was used. To maintain the gross structural features, the initial temperature

was reduced to 1.5 to lessen the probability of large uphill steps in the  $\chi^2$  function, leading to excessive alterations of the structural model. In addition, the crucial new feature was that a continuity check was made on the PEO chain. This continuity check involved only accepting models whose C<sup>12</sup> to O<sup>1'</sup> gap was less than a certain distance. O<sup>1'</sup> was obtained by translating O<sup>1</sup> along the a-axis. This distance was initially set to be larger than required to allow acceptance of the initial model with the discontinuous chain from the previous S.A. run. However, to ensure continuity, this allowed distance was slowly reduced until it reached a sensible value. This S.A. run rapidly gave a final model that provided a similar fit to the previous run, fig. 6.8, with a slightly higher  $\chi^2$  of 18.45. The model was also largely similar to the model from the previous S.A. run but with a continuous chain, fig. 6.9. This model, with a continuous PEO chain is a far more realistic starting model for Rietveld refinement.

Rietveld refinement was carried out on the final model obtained from the S.A. process using the GSAS<sup>15</sup> suite of programs. Hydrogen atoms were added to the PEO chain to form idealised tetrahedral co-ordination around the carbon atoms and their positions were included in the refinement, which brought the total number of refined atoms to 50. Soft restraints were employed to keep all bond lengths and angles within reasonable ranges. This form of restraint allows a degree of variation in the value of the parameter being restrained as long as it is justified in

terms of the improvement in the fit. As in the case of the preceding structure solution by S.A., the target values of the bond lengths and angles were taken from a variety of previously solved structures.

Unlike the solution stage, crystallographic co-ordinates of all constituent atoms served as variables during the refinement. In order to reduce the number of variables, displacement factors were taken to be identical for similar atoms, adding 6 variables to the total. This, along with the 5 parameters of the pseudo-Voigt profile function, the 4 lattice parameters, scale factor and asymmetry, gave a total of 168 parameters that were varied during the refinement process.

The refinement process resulted in a considerably improved fit, fig.6.10, with a  $\chi^2$  of 2.63. In terms of variation in the structural model, fig. 6.11, some slight rearrangement of the chains can be observed. A tunnel consisting of two interlocked saw tooth PEO chains is formed. The cations are located in the cavity formed by the polymer chains and are five co-ordinated by ether oxygens, fig. 6.12. The  $\text{AsF}_6^-$  anions are octahedral and aligned in a row parallel to the polymer cylinders with no interaction with either the lithium cation or the polymer.

This model would appear to be sensible in that the cations provide the attractive forces required to hold the two PEO chains in proximity which

would otherwise be sterically unfavourable. In addition, the lithium ion is five co-ordinated as might be expected from other PEO:lithium salt structures<sup>4,16</sup>. However, the co-ordination of the lithium ion entirely through the ether oxygens is to date unique. Despite the unusualness of this situation, it does fit in with the trend of cationic co-ordination by PEO. In compounds with a PEO:salt ratio of 1:1, the cation is co-ordinated by two ether oxygens with the remaining co-ordination being via the anions. In the more dilute 3:1 compounds, either three or four ether oxygens are involved in cation co-ordination whilst in the even more dilute 4:1 compounds, cations are co-ordinated by five ether oxygens. Thus, following this trend, it is not unreasonable to assume that the PEO chain is involved in co-ordination of the cation to an even greater extent in this 6:1 compound.

Despite the chemically sensible positioning of the  $\text{Li}^+$  cations, the fact remains that their co-ordinates, although crucial to the understanding of the properties of the compound, can't be determined reliably by x-ray diffraction. Whilst the amplitude of x-rays scattered by lithium is negligible in comparison with the rest of the atoms in the asymmetric unit, this is not the case for the scattering of neutrons. Thus, it was decided to verify the structure using powder neutron diffraction.

The diffraction pattern collected on OSIRIS containing 3,899 data points and spanned 1,370 reflections, fig. 6.13, was similar in many respects to the diffraction pattern collected from the laboratory x-ray diffractometer, fig. 6.14. The main four peaks at 3.92, 4.05, 4.38 and 8.77Å still being prominent but with the ratios of intensity differing.

Rietveld refinement was undertaken using these data starting from the final model obtained from x-ray data but with the hydrogens being replaced by deuteriums.

The refinement converged to a model, fig. 6.15 and table 6.1, with a reasonable fit, fig. 6.16, which after further refinement using the much better quality x-ray data gave a  $\chi^2$  of 3.2,  $R_p$  of 4.9% and  $R_{wp}$  of 6.6%. This model is very similar to the final model obtained from x-ray data alone with the lithium inside the chain with slight rearrangement of the PEO chain. This rearrangement results in a PEO tunnel with a more circular cross section. The lithium remains five co-ordinated, fig. 6.17, with reasonable Li-O distances.

#### **Section 6.4: Discussion and Conclusions**

The structure of  $\text{PEO}_6\text{:LiAsF}_6$  has been shown to be that in fig. 6.15. This structure is the first PEO:salt structure solved with a PEO:salt ratio greater than four and is quite exceptional in many ways. The first

remarkable feature is the way that two PEO chains interlock to form tunnels. Six ethylene oxide units are used to describe the chain with all C-C and C-O bond lengths as well as C-C-O and C-O-C bond angles being typical of those found in other PEO complexes. Each PEO chain takes a conformation of  $ctg\bar{g}tg\bar{c}\bar{g}tctt\bar{g}t\bar{g}cgt$ , starting with the first C-O bond (cis defined as  $0\pm 45^\circ$ , trans defined as  $180\pm 45^\circ$  and the rest gauche or anti-gauche). This describes a saw-tooth style chain that is arranged into a hemi-cylinder, fig. 6.18. The second PEO chain then completes the cylinder by interlocking on both sides with the first chain. The cylinders are aligned along the a-axis and are centred on each corner of the unit cell and also at the midpoint of the b-axis, fig. 6.15.

The lithium cations are located inside the polymer tunnels, being linearly aligned close to the tunnel axes. The lithium ions are spaced  $5.4(1)\text{\AA}$  and  $9.2(1)\text{\AA}$  apart. The lithium ion is co-ordinated by five ether oxygens of the polymer chains. One polymer chain provides three co-ordinating oxygens, whilst the other provides two in what could be described as a distorted square pyramid arrangement. The sixth oxygen in the PEO chain repeat unit is not involved in co-ordination.

The  $\text{AsF}_6^-$  anions are arranged in rows parallel to the PEO cylinders. The anions are located in a cavity bordered by four PEO cylinders. In this position, the anions are far removed from the cations, with a closest

approach of 5.11Å. This is a novel structural feature, since in every other polymer complex solved to date, the anions are involved to a varying degree in the co-ordination process.

It is believed that polymer-salt complexes almost exclusively conduct in the amorphous phase. At the same time, there are indications that local order is retained in the transition from the crystalline to the amorphous phase<sup>17</sup>. If that was the case in this structure, then there are several structural features that would support many of the long held beliefs of the features necessary for good conduction.

The first of these is the fact that the cations and anions are separated in this compound with minimal interactions or ion pairing. Ion pairing has been shown to be unfavourable in terms of conduction. The pairing of ions can lead to a situation where ionic bonds have to be broken in order for a species to migrate. In addition, most conduction theories specify that ionic conduction is lessened for larger mobile species. Thus, it would be reasonable to assume that formation of ion pairs or ionic aggregates of any kind would retard conductivity.

In addition, the presence of polymer tunnels could be an important feature in allowing higher conductivities. It has been postulated<sup>18-20</sup> that, in addition to local chain mobility, which promotes ion transport, it is

essential to have pathways that allow easy transport of ions. It had been suggested that these should take the form of either helices<sup>21</sup> or double helices<sup>22</sup>. However, the double chain PEO tunnels present here would also allow easy transport of the cationic species along the length of the cylinder. In addition, the sixth oxygen, unused in the co-ordination process in the static, crystalline phases would be available to assist in transport of the mobile cation. Furthermore, if the loss of ordering of the PEO cylinders in the amorphous state is slight compared to the crystalline phase, then the regular arrangement would provide a simple route for transport of cations from one tunnel to the next.

The structure is arranged in a way that is not only beneficial to cationic conduction but possibly also to anionic conduction. Although the PEO chains do not envelop the anions, they are corralled into channel like cavities by the PEO tunnels. Thus, anionic conduction might be increased, at least in the chain direction.

Despite the presence of these features that could be construed as beneficial to conduction, an 'unfavourable' feature can also be found. The sharing of cations between two chains would constitute a severe case of cross-linking. This is usually considered to have a detrimental effect on conduction by impeding segmental motion of the PEO chain. However, unlike compounds, such as those with a PEO:salt ratio of 1:1, which form

extensive three dimensional networks, this form of cross-linking only serves to twin pairs of PEO chains. A method of conduction involving co-operative motions of the PEO chains in order to conduct cations along the tunnels can be envisaged which would not be significantly hindered by this form of cationic cross-linking.

Thus, to summarise, this structure contains many structural features that have not been seen in the structures of other PEO:salt compounds. The generally higher conductivity of materials with a PEO:salt ratio of 6:1 over those with ratios of 1:1, 3:1 or 4:1 can be explained by some of these features as long as the local crystalline order is retained in the amorphous state. In addition the determined structure provides new insight into the microscopic conduction mechanism of these materials. The double chain tunnel structures would indicate some conduction of cations down the cylinders by means of co-operative motion of the PEO chains and the further conduction of cations via a inter-cylinder hopping process. Clearly to investigate these implications further, a study of the crystalline into amorphous phase transition, similar to that carried out in ref. 19 is appropriate. In addition, conductivity studies on the material would confirm some of the mechanistic deductions.

## Section 6.5: References

- [1] C.A.Angell, *Solid State Ionics*, **9/10** (1983) 3
- [2] S.Kirkpatrick, C.D.Gelatt Jr., M.P.Vecchi, *Science* **220** (1983) 671.
- [3] Y.G.Andreev, P.Lightfoot, P.G.Bruce, *J.Appl. Crystallogr.* **30** (1997) 294.
- [4] Y.G.Andreev, P.Lightfoot, P.G.Bruce, *Chem. Commun.*, (1996) 2169
- [5] Y.G.Andreev, G.S.MacGlashan, P.G.Bruce, *Phys. Rev. B*, **55** (1997) 12011
- [6] A.Lauenstein, A.Johansson, J.Tegenfeldt, *J. Electrochem. Soc.*, **141** (1994) 1819
- [7] J.M.G.Cowie in *Polymers: Chemistry and Physics of Modern Materials 2<sup>nd</sup> ed.*, Blackie, New York
- [8] C.D.Robitaille, D.Fauteux, *J. Electrochem. Soc.*, **133** (1986) 315
- [9] M.Z.A.Munshi, B.B.Owens, *Appl. Phys. Commun.*, **6** (1987) 279
- [10] P-E.Werner, L.Eriksson, M.Westdahl, *J. Appl. Crystallogr.*, **18** (1985) 367
- [11] P.M.DeWolff, *J. Appl. Crystallogr.*, **1**(1968) 108
- [12] A.LeBail, H.Duroy, J.L.Fourquet, *Mat. Res. Bull.*, **23** (1988) 447
- [13] Y.G.Andreev, T.Lundström, N.I.Sorokin, *Nucl. Instr. And Meth. In Phys. Res.*, **A354** (1995) 134

- [14] W.H.Press, S.A.Teukolsky, W.T.Vetterling, B.P.Flannery, *Numerical Recipes in C: The Art of Scientific Computing*, Cambridge University Press (1992)
- [15] A.Larson, R.Von.Dreele, Los Alamos National Laboratory, LA-UR-86-748 (1987)
- [16] P.Lightfoot, M.A.Mehta, P.G.Bruce, *Science*, **262** (1993) 883
- [17] R.Frech, S.Chintapalli, P.G.Bruce, C.A.Vincent, *J. Chem. Soc. Chem. Commun.*, **2** (1997) 157
- [18] P.G. Bruce, *Phil. Trans. R. Soc. Lond. A*, **354** (1996) 415
- [19] P.G.Bruce, G.S.MacGlashan, Y.G.Andreev, *Implications of Molecular and Materials Structure for New Technologies*, ed. J.A.Howard and F.H.Allen, Nato Science Series E: Applied Sciences, Kluwer, Dordrecht, 1999-05-16
- [20] F.B.Dias et al, *Electrochim. Acta*, **43** (1998) 1217
- [21] M.B.Armand, J.M.Chabagno, M.J.Duclot, *Fast-ion Transport in Solids*, ed. P.Vashishta, J.N.Mundy, G.Shenog, North-Holland, Amsterdam (1979) 131
- [22] J.M.Parker, P.V.Wright, C.C.Lee, *Polymer*, **22** (1981) 1305

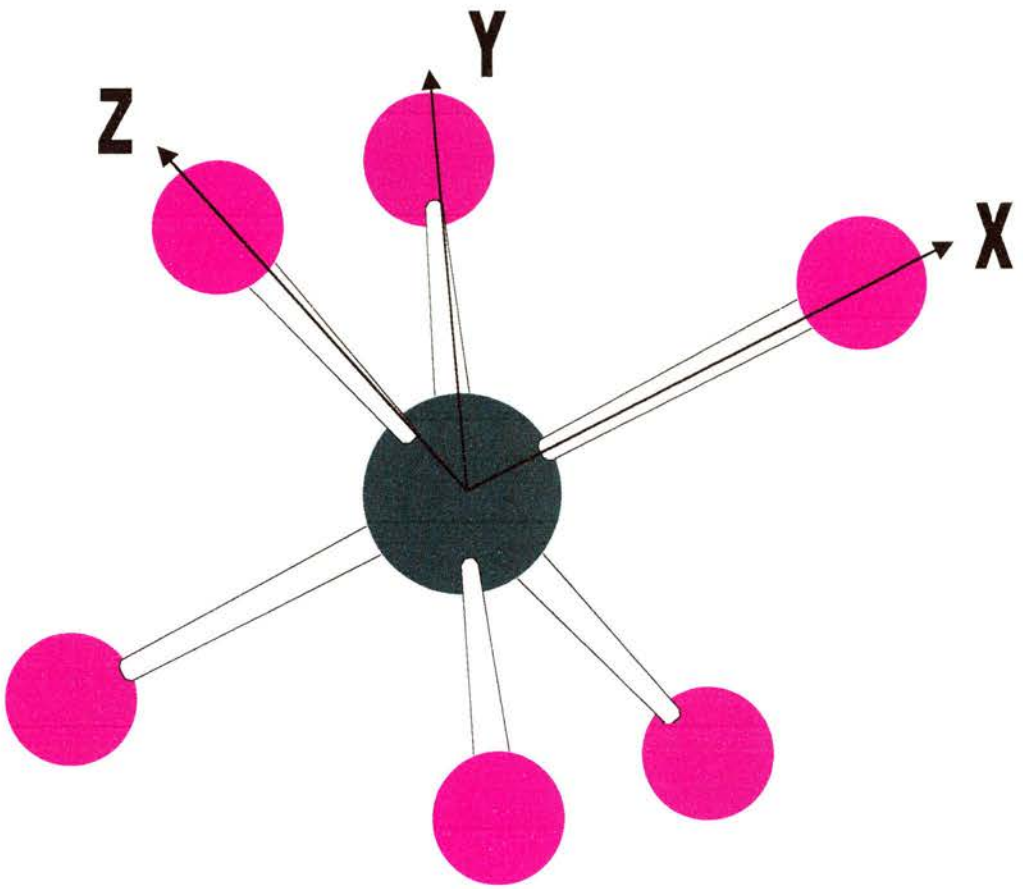


Fig. 6.1: Local Frame of Reference for the  $\text{AsF}_6^-$  molecule

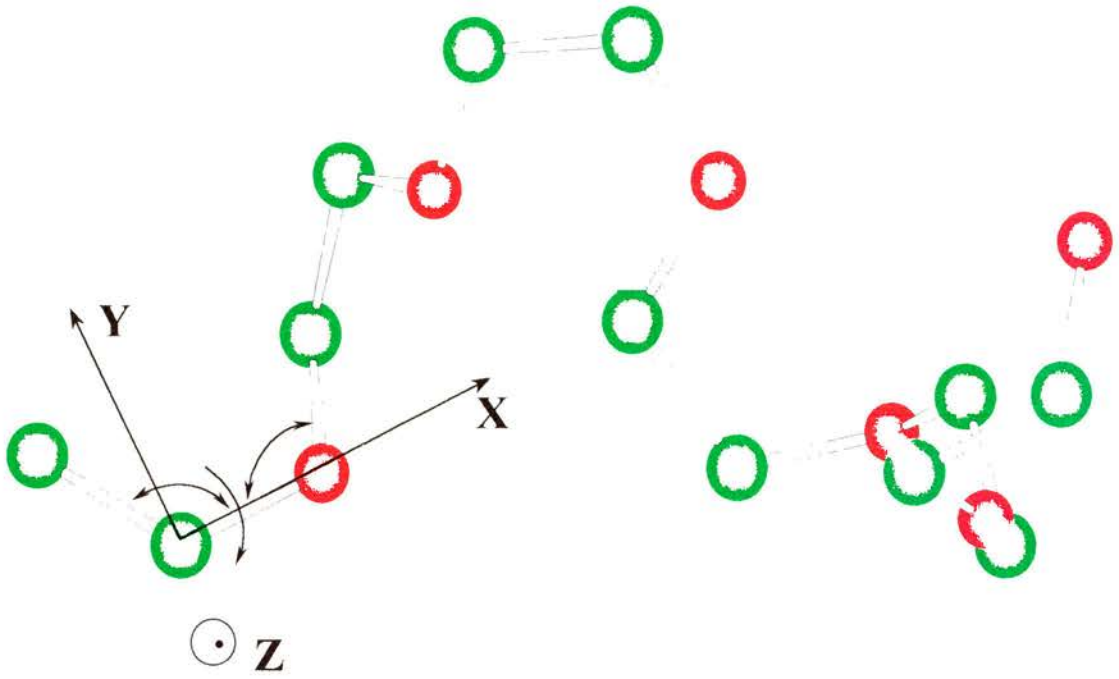


Fig. 6.2: Local Frame for the PEO Chain

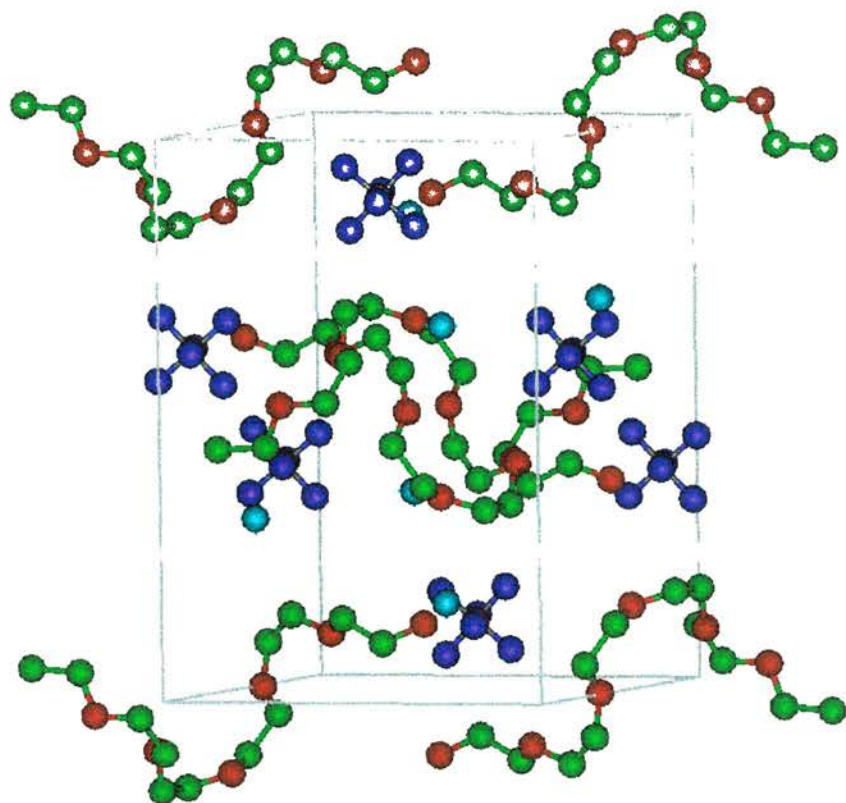


Fig. 6.3: Structure of Starting Model for the First S.A. Run. Green atoms - carbon, red atoms - oxygen, purple atoms - fluorine, grey atoms - arsenic and light blue atoms - lithium.

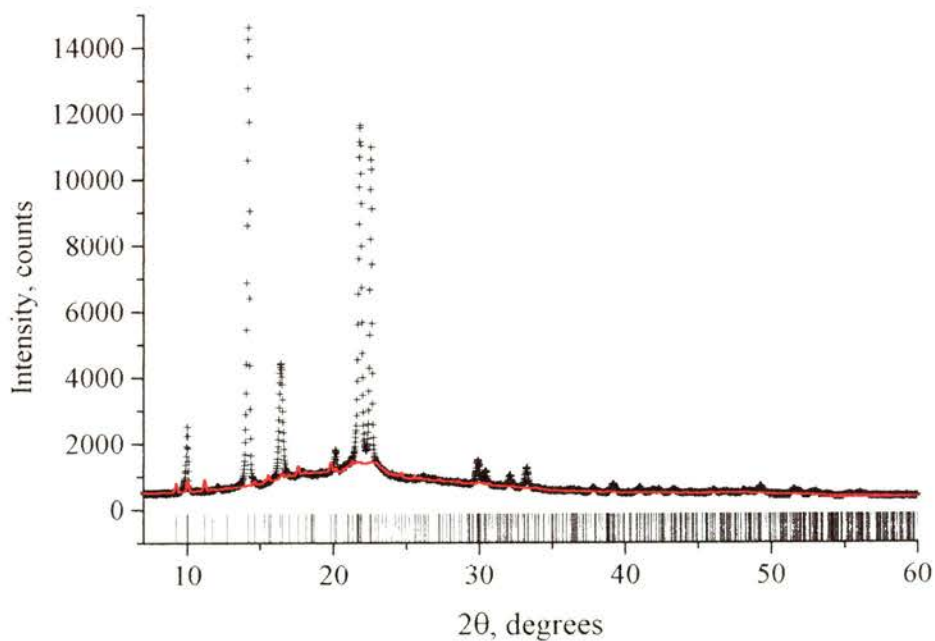


Fig. 6.4: Fit of the diffraction pattern obtained from the starting model (red line) to the experimental pattern (black crosses)

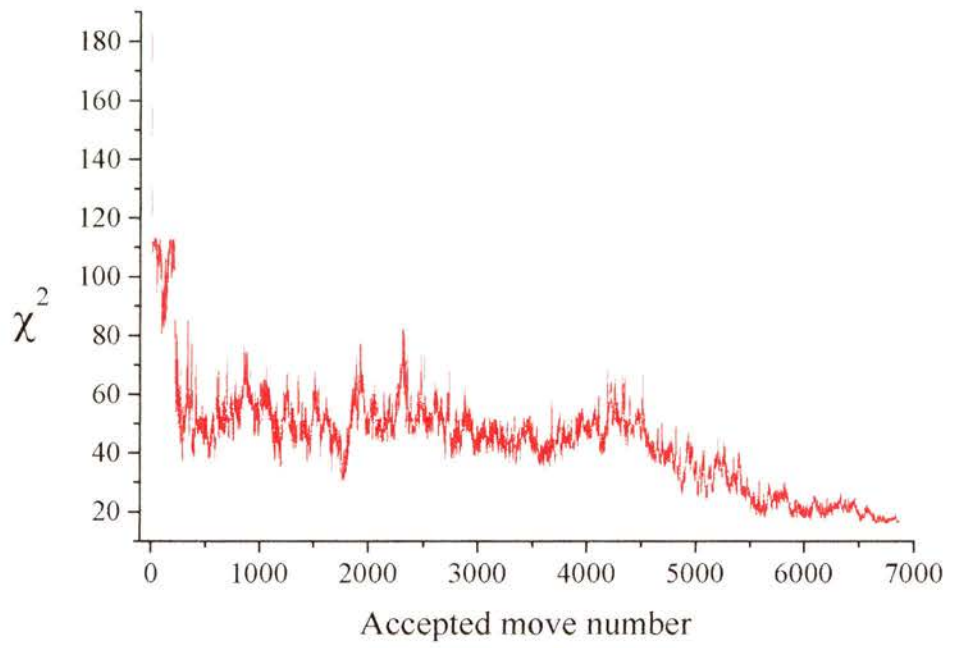


Fig. 6.5:  $\chi^2$  variation with accepted move for the first simulated annealing run.

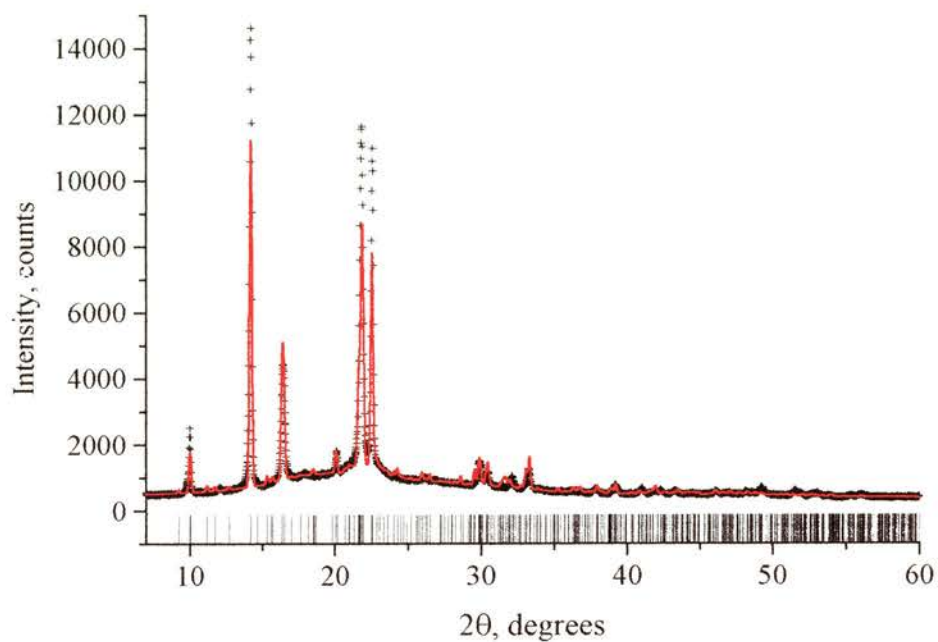


Fig. 6.6: Final fit of calculated to experimental pattern for the first S.A. run.

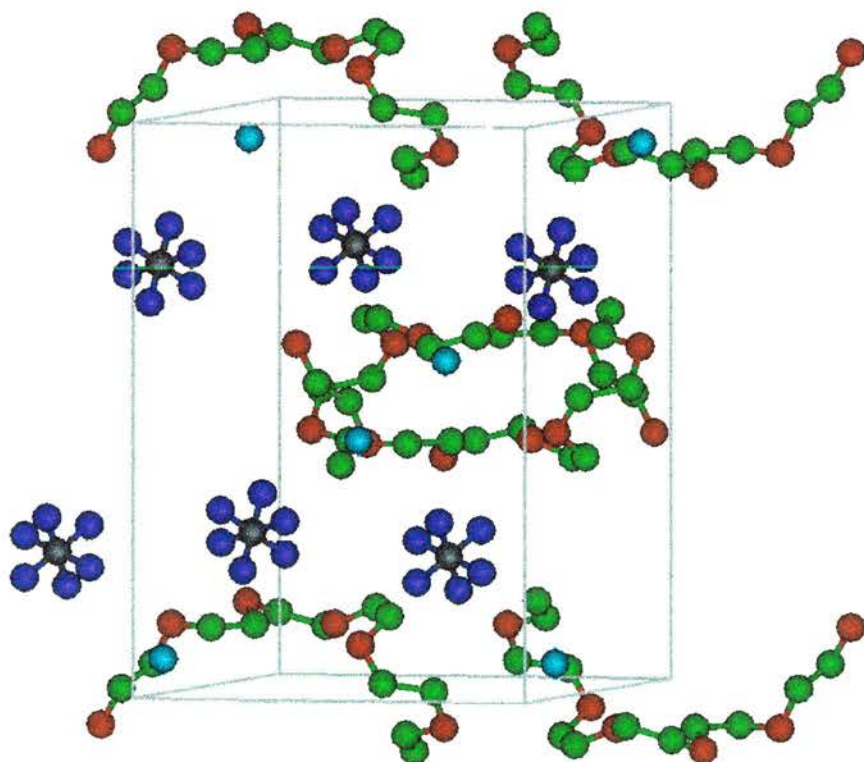


Fig.6.7: Final structural model obtained from the first S.A. run.

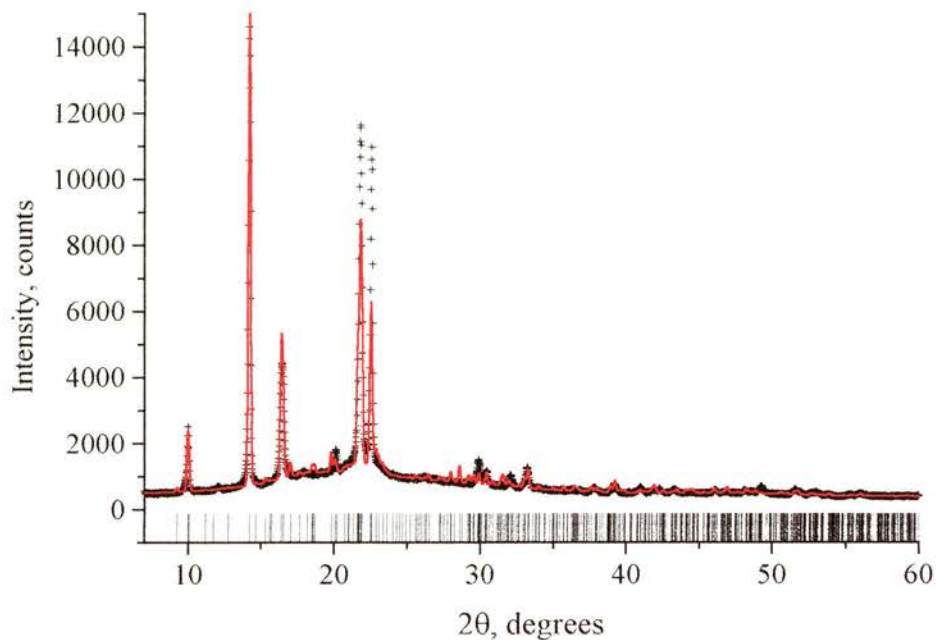


Fig. 6.8: Fit of the diffraction pattern of the final model obtained from the second S.A. run plotted to the experimental pattern.

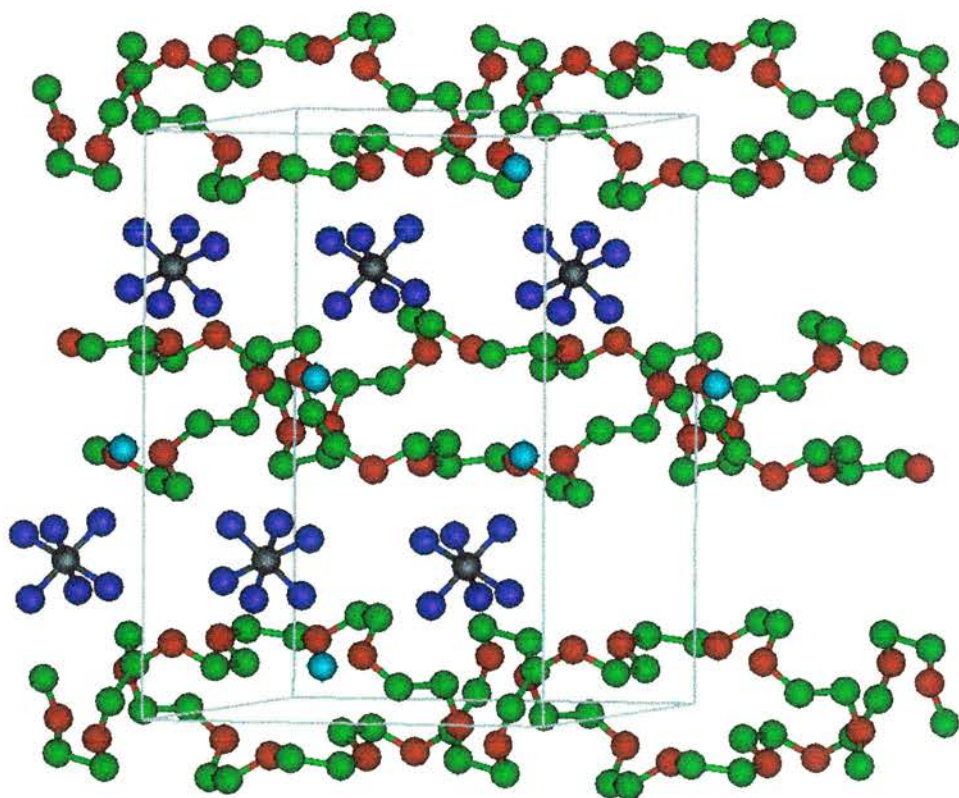


Fig. 6.9: The final structural model obtained from the second S.A. run.

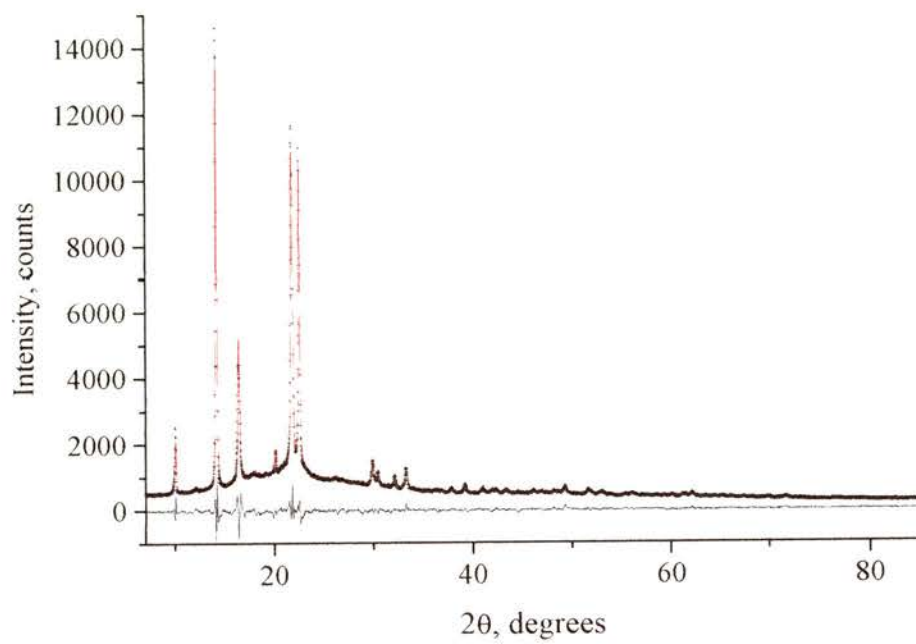


Fig. 6.10: Fit after the refinement.

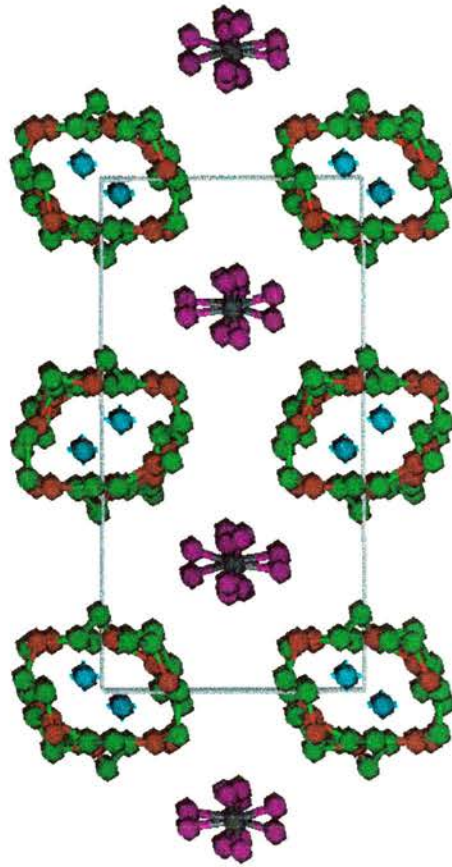


Fig 6.11: Structural model after refinement.

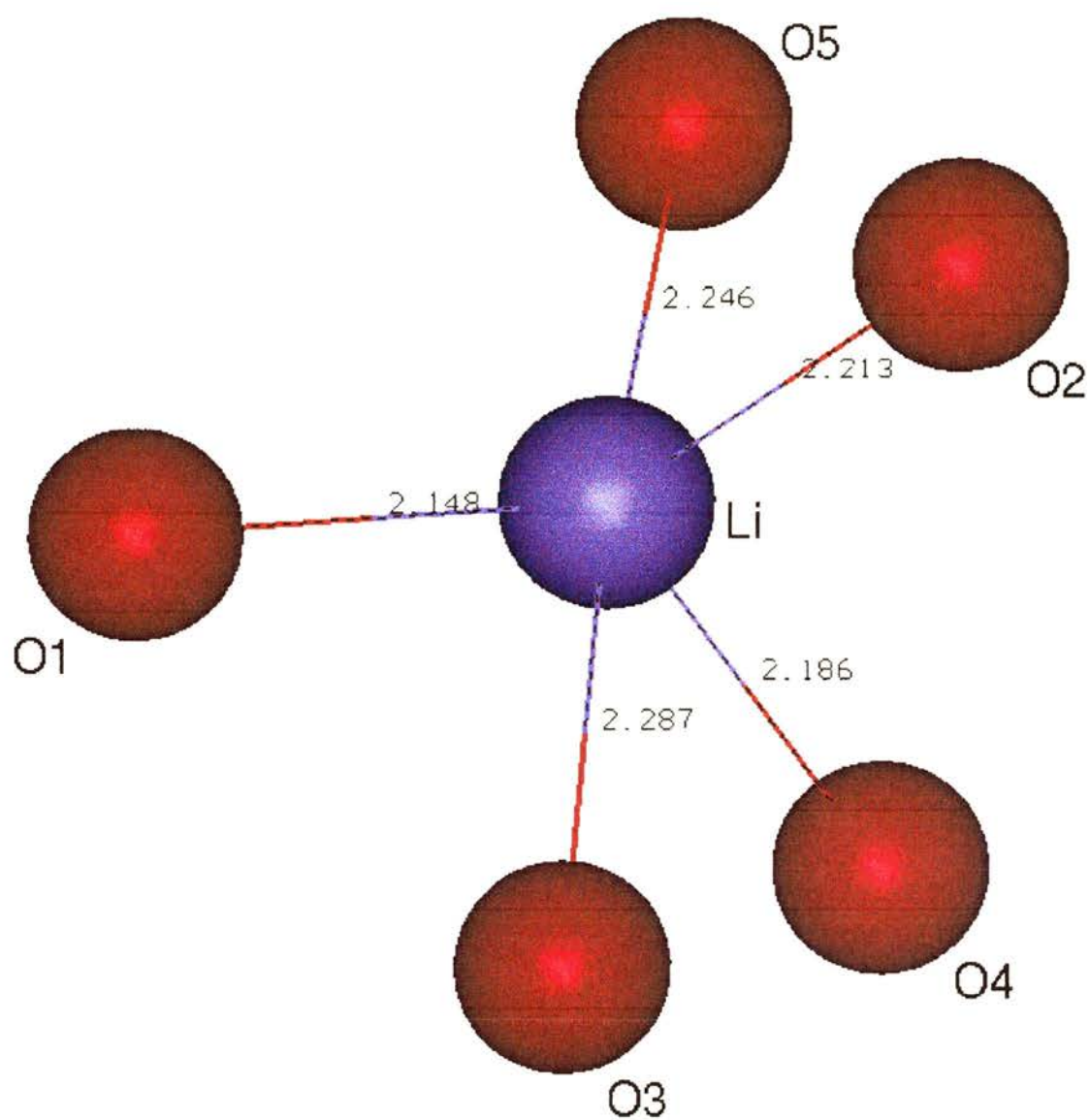


Fig. 6.12: Coordination of the lithium ion after refinement of x-ray data.

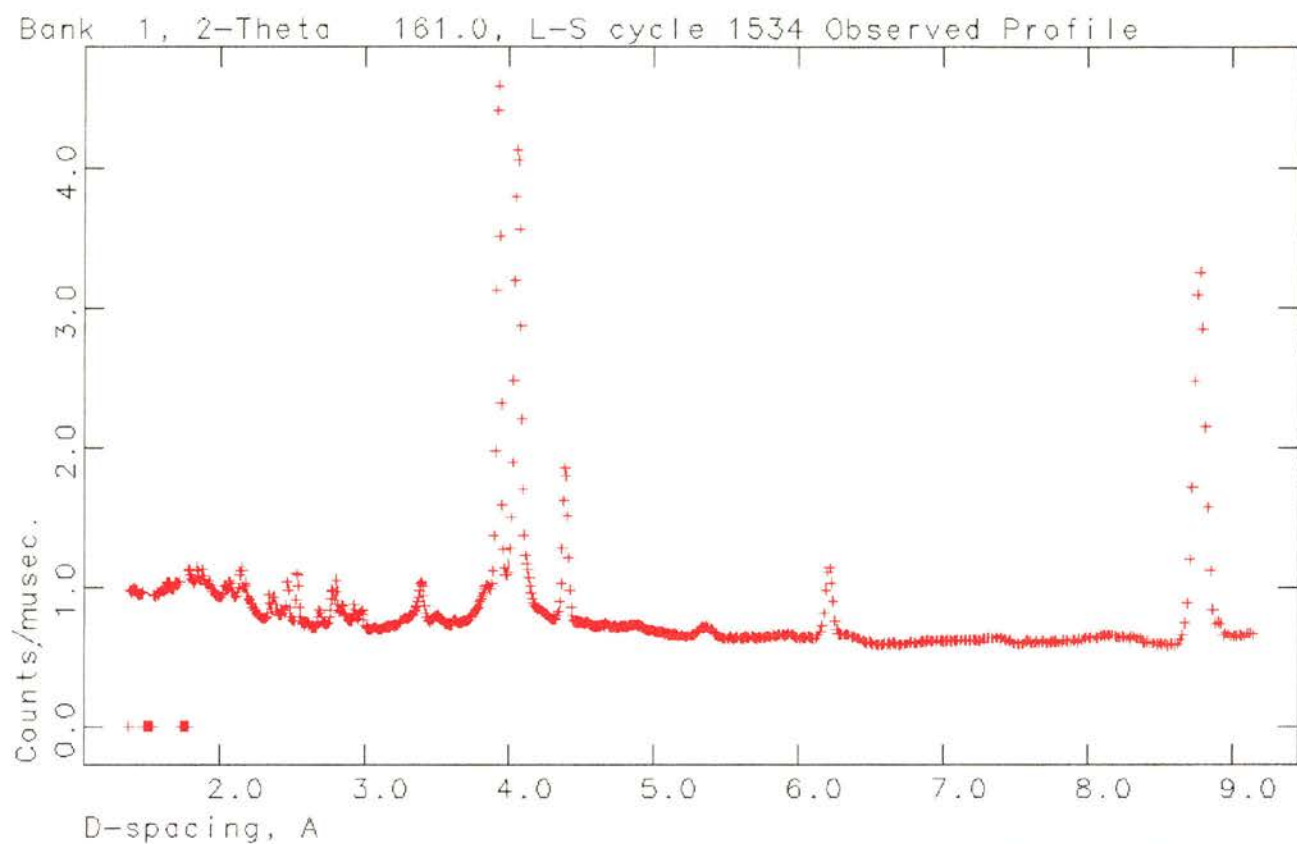


Fig. 6.13: The neutron diffraction pattern of deuterated  $\text{PEO}_6:\text{LiAsF}_6$  collected on the OSIRIS instrument at Rutherford Appleton Laboratory.

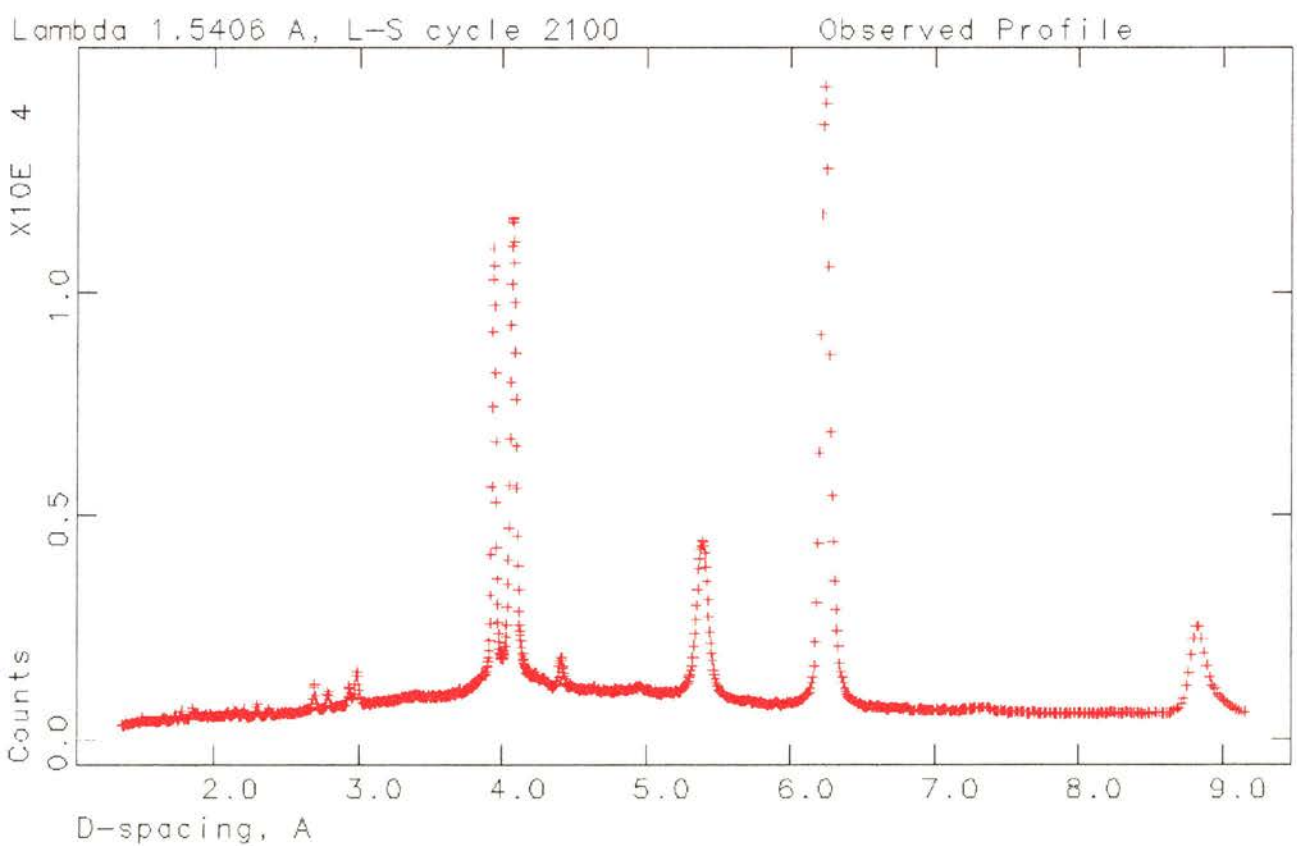


Fig. 6.14 The x-ray diffraction pattern of  $\text{PEO}_6:\text{LiAsF}_6$  collected on a laboratory diffractometer.

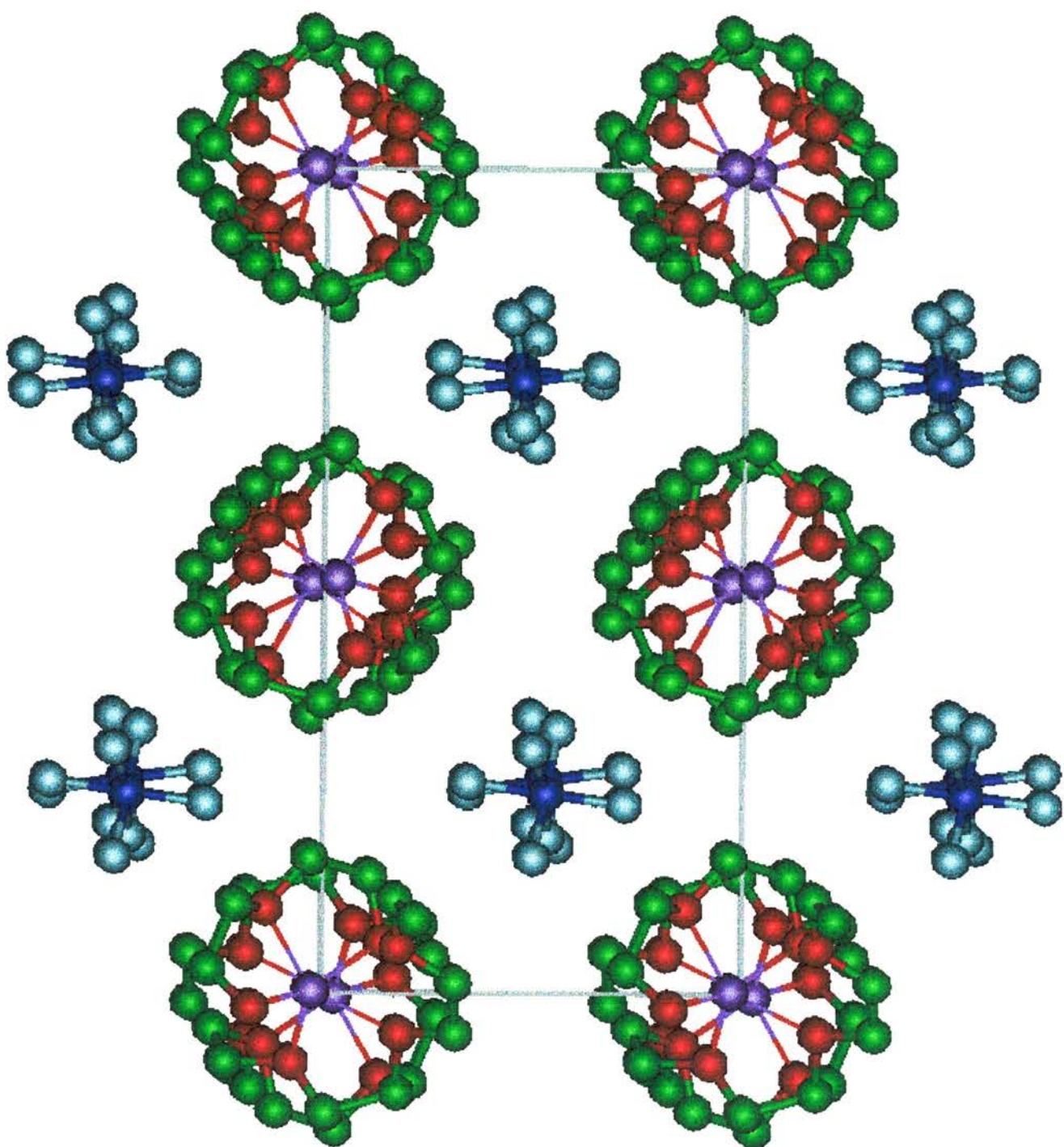


Fig. 6.15a: The final structure of  $\text{PEO}_6:\text{LiAsF}_6$  (after refinement using neutron diffraction data); Lithium: purple, oxygen:red, carbon: green, arsenic: blue, fluorine: grey.

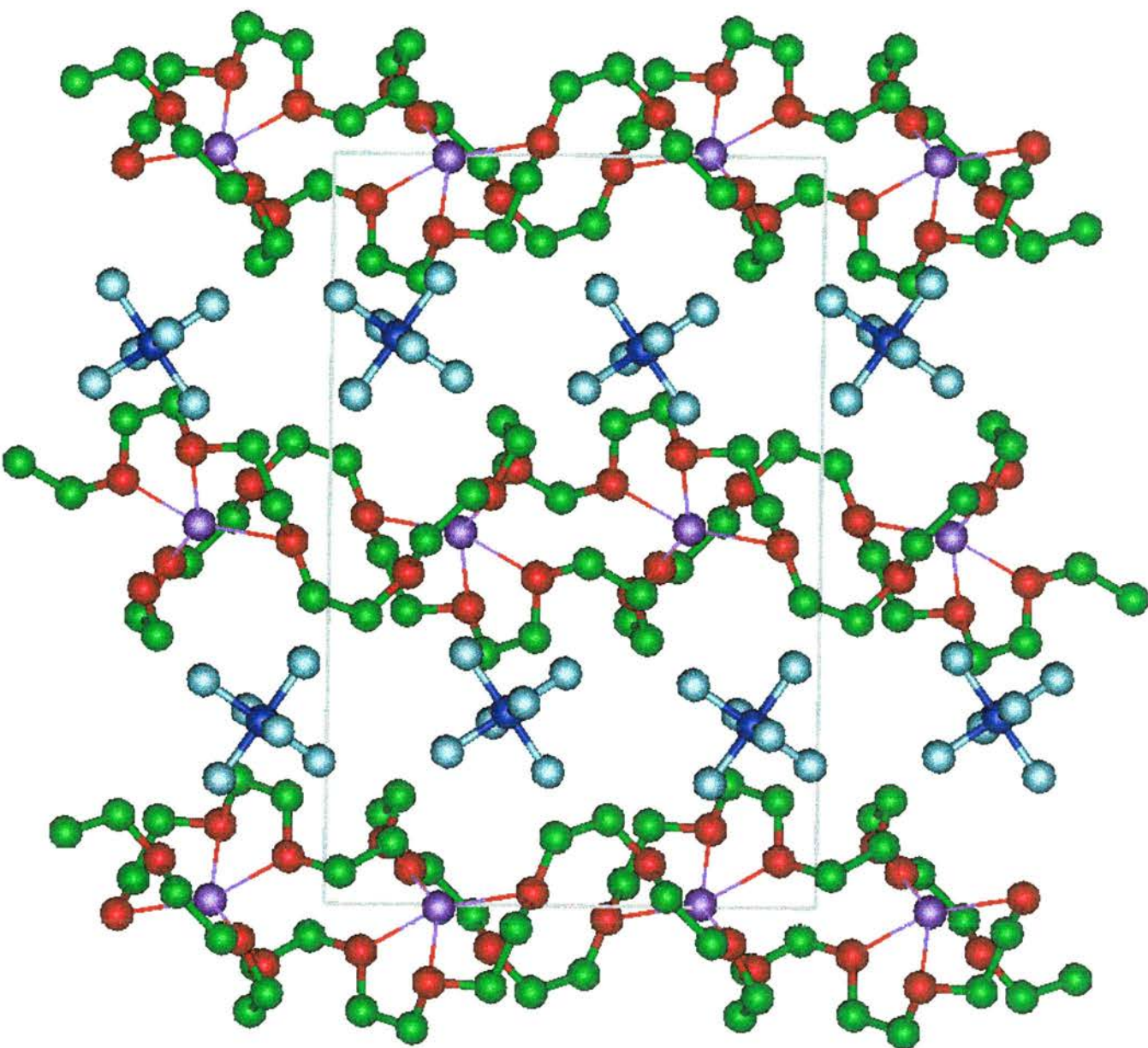


Fig.6.15b: The final structure of  $\text{PEO}_6:\text{LiAsF}_6$  (after refinement using neutron diffraction data)

Bank 1, 2-Theta 161.0, L-S cycle 2261 Obsd. and Diff. Profiles

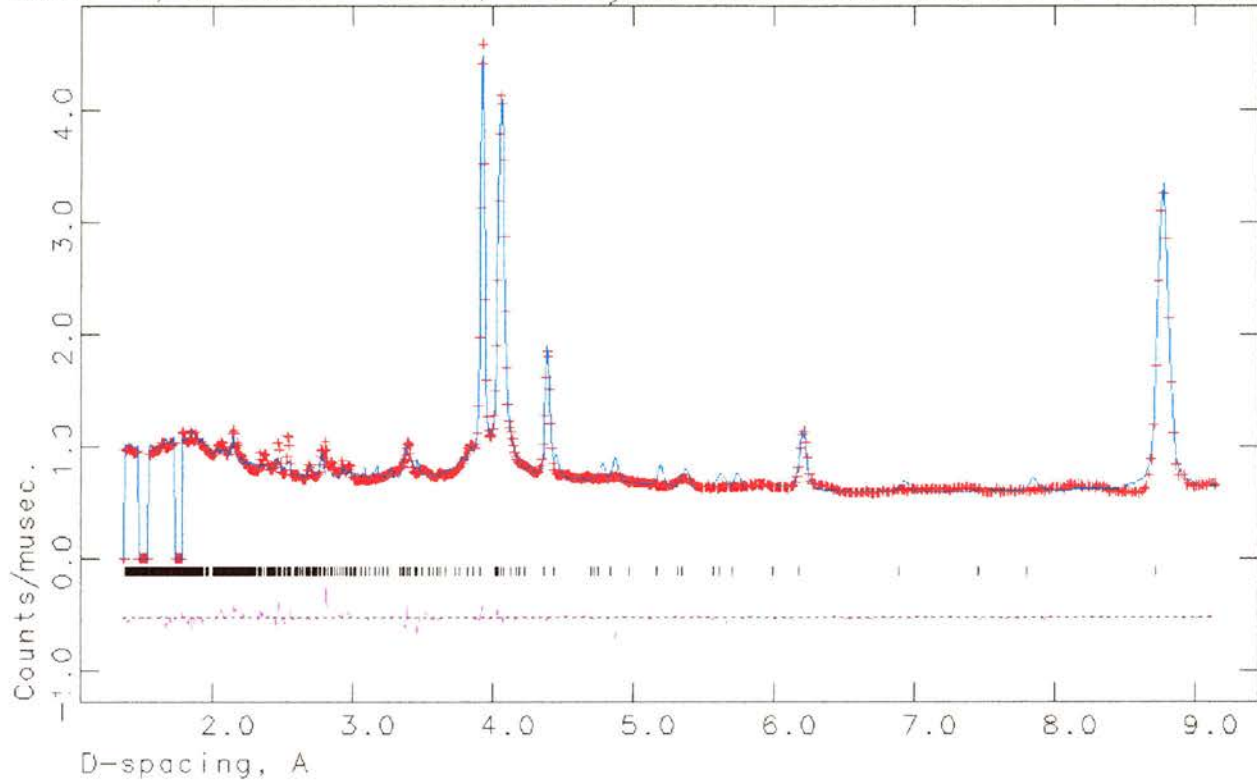


Fig. 6.16: The final fit using the neutron diffraction data.

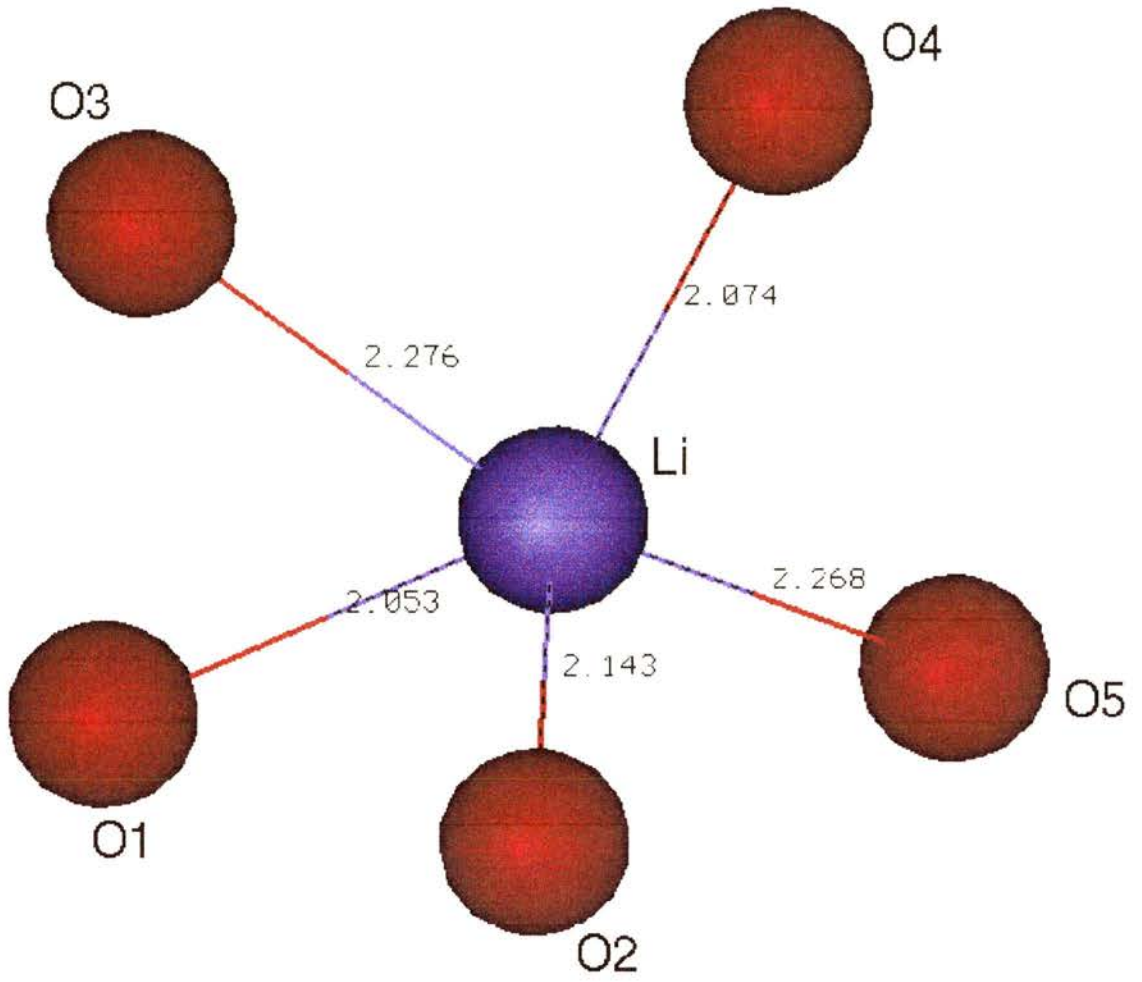


Fig. 6.17: Coordination of Lithium in the final model after refinement of neutron data.

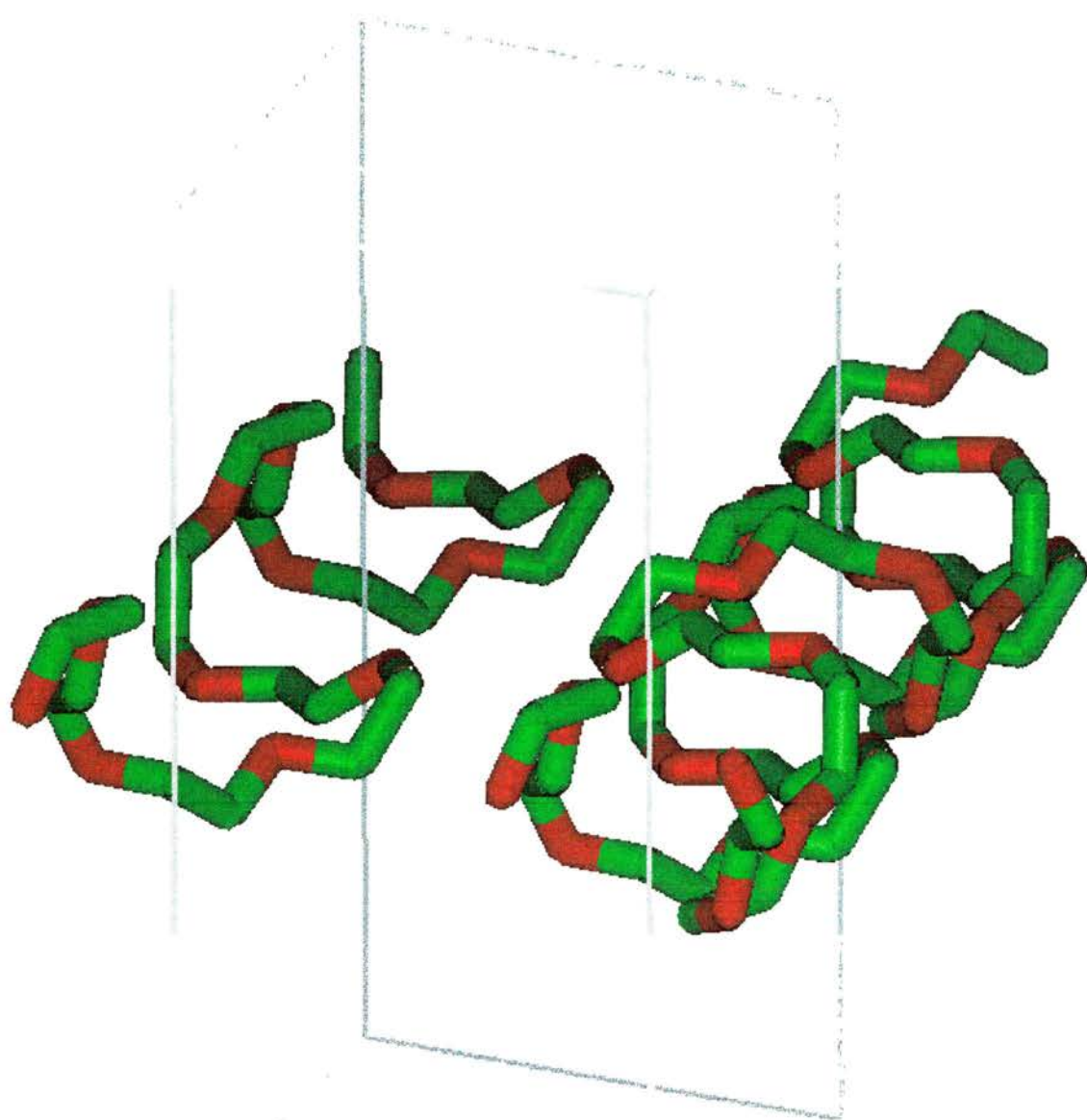


Fig. 6.18: Representation of the PEO chains from  $\text{PEO}_6:\text{LiAsF}_6$ , showing the saw-tooth conformation of one chain and two interlocking chains, forming a PEO tunnel.

**Table 6.1: TOF neutron and X-ray coordinates for PEO<sub>6</sub>:  
LiAsF<sub>6</sub>**

Atom	x		y		z		U	
Li	0.767(4)	0.780(3)	-0.004(3)	-0.010(2)	-0.028(6)	-0.007(4)	0.019(9)	0.12(6)
As	0.633(5)	0.625(1)	0.257(2)	0.259(1)	0.470(4)	0.487(1)	0.02(3)	0.031(1)
F1	0.515(6)	0.518(3)	0.310(3)	0.305(1)	0.467(9)	0.516(4)	0.02(1)	0.016(3)
F2	0.718(6)	0.723(2)	0.335(3)	0.319(1)	0.502(9)	0.528(4)		
F3	0.663(8)	0.638(3)	0.243(4)	0.219(1)	0.656(5)	0.640(3)		
F4	0.600(8)	0.571(3)	0.270(4)	0.277(2)	0.283(4)	0.312(2)		
F5	0.549(6)	0.539(2)	0.179(3)	0.190(1)	0.441(9)	0.472(4)		
F6	0.754(5)	0.743(2)	0.204(3)	0.212(2)	0.504(1)	0.522(4)		
C1	1.303(3)	1.362(3)	0.013(2)	0.001(2)	0.688(3)	0.728(4)	0.40(3)	0.009(5)
C2	1.210(3)	1.248(3)	-0.048(2)	-0.045(2)	0.685(3)	0.693(4)		
O1	1.174(6)	1.171(3)	-0.048(2)	-0.028(2)	0.818(5)	0.775(4)	0.11(8)	0.14(1)
C3	1.116(4)	1.164(4)	-0.120(2)	-0.102(2)	0.823(3)	0.835(3)		
C4	1.150(3)	1.216(3)	-0.145(1)	-0.098(2)	0.993(3)	1.009(3)		
O2	1.122(3)	1.127(2)	-0.083(2)	-0.083(2)	1.075(1)	1.082(2)		
C5	1.137(3)	1.161(3)	-0.083(2)	-0.073(3)	1.232(1)	1.244(2)		
C6	1.030(3)	1.066(3)	-0.043(2)	-0.024(2)	1.261(3)	1.278(3)		
O3	0.924(4)	0.964(3)	-0.063(2)	-0.038(2)	1.141(6)	1.152(4)		
C7	0.920(3)	0.949(3)	-0.142(2)	-0.119(2)	1.110(3)	1.115(4)		
C8	0.818(2)	0.816(3)	-0.165(1)	-0.139(2)	0.968(3)	1.037(3)		
O4	0.785(1)	0.780(2)	-0.103(2)	-0.119(2)	0.861(3)	0.881(3)		
C9	0.659(1)	0.666(2)	-0.109(2)	-0.125(2)	0.789(4)	0.779(3)		
C10	0.610(3)	0.644(3)	-0.030(2)	-0.043(2)	0.723(3)	0.717(3)		
O5	0.576(5)	0.598(4)	0.017(3)	-0.005(2)	0.827(4)	0.823(3)		
C11	0.531(3)	0.514(3)	0.091(2)	0.052(2)	0.785(4)	0.749(3)		
C12	0.423(2)	0.476(3)	0.115(1)	0.101(2)	0.832(4)	0.863(4)		
O6	0.339(3)	0.360(3)	0.057(2)	0.069(2)	0.824(2)	0.821(4)		
H1	1.139(4)	1.376(5)	-0.040(4)	0.021(7)	0.604(5)	0.640(3)	0.076(8)	0.08(f)
H2	1.241(6)	1.429(7)	-0.097(2)	-0.027(2)	0.682(8)	0.78(1)		
H3	1.280(4)	1.202(5)	-0.135(4)	-0.040(6)	0.885(9)	0.589(9)		
H4	1.150(6)	1.265(8)	-0.153(2)	-0.098(3)	0.768(5)	0.713(6)		
H5	1.101(6)	1.317(7)	-0.187(2)	-0.082(4)	1.000(5)	0.870(6)		
H6	1.233(4)	1.210(5)	-0.154(4)	-0.133(5)	1.025(5)	0.793(6)		
H7	1.146(6)	1.254(9)	-0.133(2)	-0.145(3)	1.274(5)	1.047(6)		
H8	1.203(3)	1.271(3)	-0.053(4)	-0.057(6)	1.289(4)	1.032(6)		
H9	1.042(4)	1.161(6)	0.010(2)	-0.122(2)	1.269(8)	1.29(1)		
H10	1.020(4)	1.235(6)	-0.059(4)	-0.047(6)	1.354(4)	1.277(4)		
H11	0.841(6)	1.085(6)	-0.205(2)	0.028(3)	0.915(5)	1.282(8)		
H12	0.748(3)	1.050(4)	-0.176(4)	-0.042(5)	0.992(6)	1.366(6)		
H13	0.626(3)	0.992(3)	-0.129(3)	-0.127(4)	0.860(7)	1.047(7)		
H14	0.650(4)	0.981(6)	-0.145(2)	-0.145(3)	0.709(6)	1.209(5)		
H15	0.671(5)	0.805(5)	-0.007(3)	-0.192(4)	0.693(7)	1.05(1)		
H16	0.541(5)	0.767(7)	-0.039(3)	-0.111(4)	0.638(5)	1.082(3)		
H17	0.591(3)	0.611(8)	0.127(3)	-0.138(4)	0.834(9)	0.830(9)		
H18	0.516(6)	0.665(4)	0.100(3)	-0.158(5)	0.679(5)	0.698(8)		
H19	0.449(4)	0.716(5)	0.137(3)	-0.019(5)	0.932(5)	0.718(4)		
H20	0.384(4)	0.586(7)	0.159(2)	-0.042(2)	0.778(8)	0.62(1)		
H21	1.273(7)	0.546(8)	0.048(3)	0.083(4)	0.605(3)	0.689(6)		
H22	1.373(4)	0.447(4)	-0.013(3)	0.025(3)	0.684(8)	0.69(1)		
H23	0.994(3)	0.515(5)	-0.157(3)	0.092(5)	1.101(8)	0.967(9)		

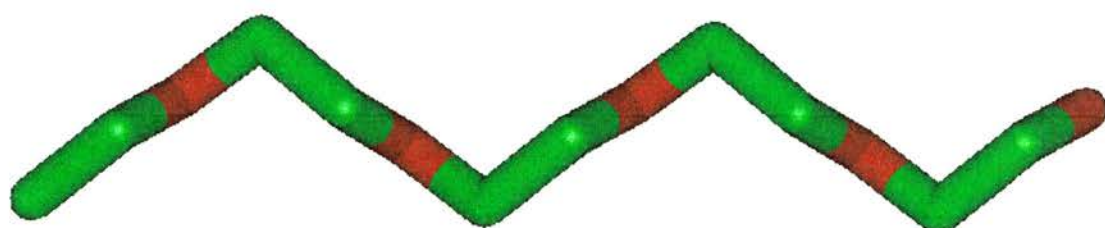
H24	0.914(7)	0.468(6)	-0.168(3)	0.153(3)	1.198(4)	0.835(8)		
-----	----------	----------	-----------	----------	----------	----------	--	--

Parameter	Neutron	X-rays
a	11.871(4)	11.9287(9)
b	17.537(3)	17.594(2)
c	9.227(3)	9.2652(6)
$\beta$	108.21(1)	108.245(5)
$\chi^2$	6.6	3.2
Rwp	0.054	0.066
Rp	0.042	0.049
Npoints	950	3899
Nref	795	1370
Nvar	168	168
Nconstr	135	135

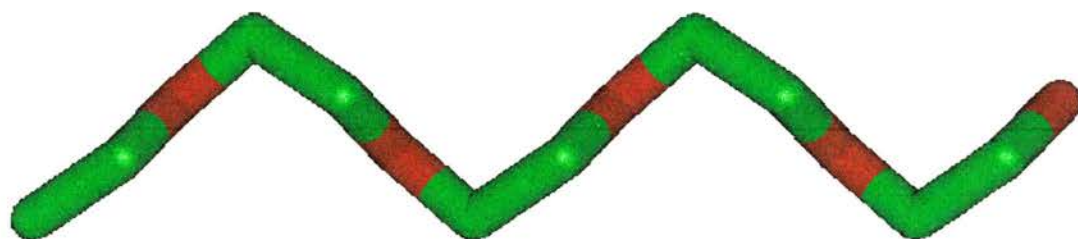
Bond length	Neutron	X-ray	Bond angle	Neutron	X-ray
LI_O1	2.05(5)	2.15	C1_C2_O1	113.81(1)	117.50(1)
LI_O4	2.07(5)	2.19	O1_C3_C4	107.46(1)	108.43(1)
LI_O2	2.14(6)	2.21	C3_C4_O2	107.16(2)	112.67(1)
LI_O5	2.26(4)	2.25	O2_C5_C6	109.44(1)	107.13(1)
LI_O3	2.28(4)	2.21	C5_C6_O3	109.21(2)	103.32(1)
LI_H15	2.46(5)	1.99(H17)	O3_C7_C8	112.97(1)	111.56(1)
LI_C10	2.51(4)		C7_C8_O4	112.08(2)	110.70(1)
LI_C9	2.55(4)		O4_C9_C10	110.10(1)	101.52(1)
LI_H8	2.73(6)	1.32(H9)	C9_C10_O5	114.35(2)	103.76(1)
LI_O6	2.74(6)		O5_C11_C12	117.14(1)	112.04(1)
LI_C4	2.76(5)	1.90	C11_C12_O6	115.05(2)	93.39(1)
			O6_C1_C2	113.88(1)	112.08(1)
AS_F1	1.67(1)	1.61(2)			
AS_F2	1.67(1)	1.53(2)	C2_O1_C3	108.15(1)	98.63(1)
AS_F3	1.66(1)	1.55(2)	C4_O2_C5	125.35(1)	120.02(1)
AS_F4	1.67(1)	1.58(2)	C6_O3_C7	110.86(1)	112.05(1)
AS_F5	1.66(1)	1.57(2)	C8_O4_C9	107.21(1)	126.29(4)
AS_F6	1.67(1)	1.57(2)	C10_O5_C11	120.88(2)	111.23(1)
			C12_O6_C1	116.54(1)	106.46(1)
C1_C2	1.54(3)	1.53(1)			
C3_C4	1.55(5)	1.54(1)			
C5_C6	1.54(4)	1.53(1)			
C7_C8	1.53(4)	1.57(1)			
C9_C10	1.54(3)	1.54(1)			
C11_C12	1.53(4)	1.53(1)			
C2_O1	1.42(4)	1.40(1)			
O1_C3	1.44(2)	1.42(1)			
C4_O2	1.42(2)	1.45(1)			
O2_C5	1.41(5)	1.43(1)			
C6_O3	1.42(4)	1.42(1)			
O3_C7	1.43(3)	1.45(1)			
C8_O4	1.43(3)	1.42(1)			
O4_C9	1.43(4)	1.40(1)			

C10_O5	1.42(3)	1.44(1)		
O5_C11	1.42(2)	1.43(1)		
C12_O6	1.41(3)	1.43(1)		
O6_C1	1.42(4)	1.47(1)		

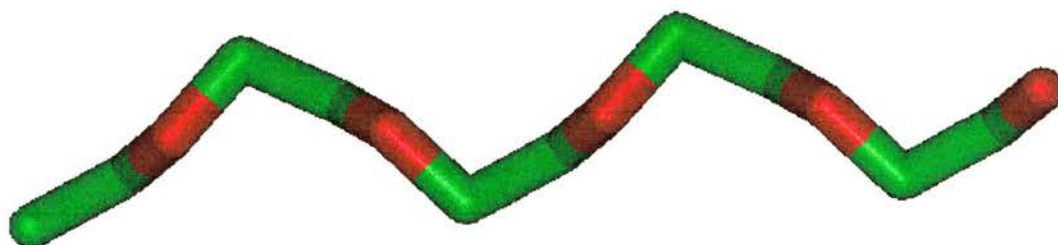
Torsion angle	Neutrons	X-rays
O6-C1-C2-O1	1.17	-12.95
C1-C2-O1-C3	-163.19	-124.15
C2-O1-C3-C4	143.28	116.17
O1-C3-C4-O2	-53.6	92.52
C3-C4-O2-C5	-178.25	-176.15
C4-O2-C5-C6	139.58	154.42
O2-C5-C6-O3	-37.76	25.35
C5-C6-O3-C7	-45.69	45.43
C6-O3-C7-C8	171.91	152.59
O3-C7-C8-O4	-27.17	79.83
C7-C8-O4-C9	145.79	-175.49
C8-O4-C9-C10	-157.15	124.75
O4-C9-C10-O5	88.28	-87.54
C9-C10-O5-C11	-179.04	-146.43
C10-O5-C11-C12	-136.57	-172.25
O5-C11-C12-O6	37.92	-109.37
C11-C12-O6-C1	47.49	-12.67
C12-O6-C1-C2	178.80	-172.19



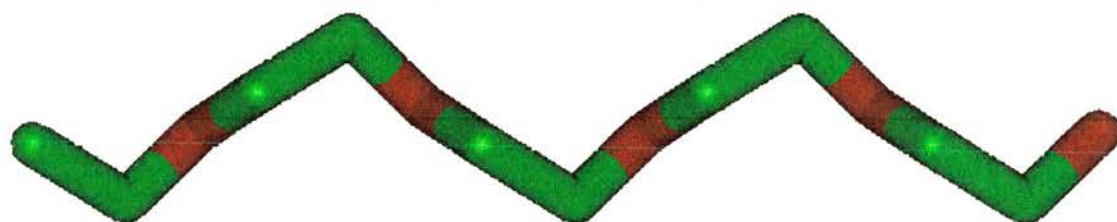
PEO chain from PEO:KTriflate



PEO chain from PEO:NaTriflate



PEO chain from PEO:NaSCN



PEO chain from PEO:HgCl<sub>2</sub>

Fig. 7.1: A representation of the PEO chains from all the PEO:salt 1:1 compounds known to date.

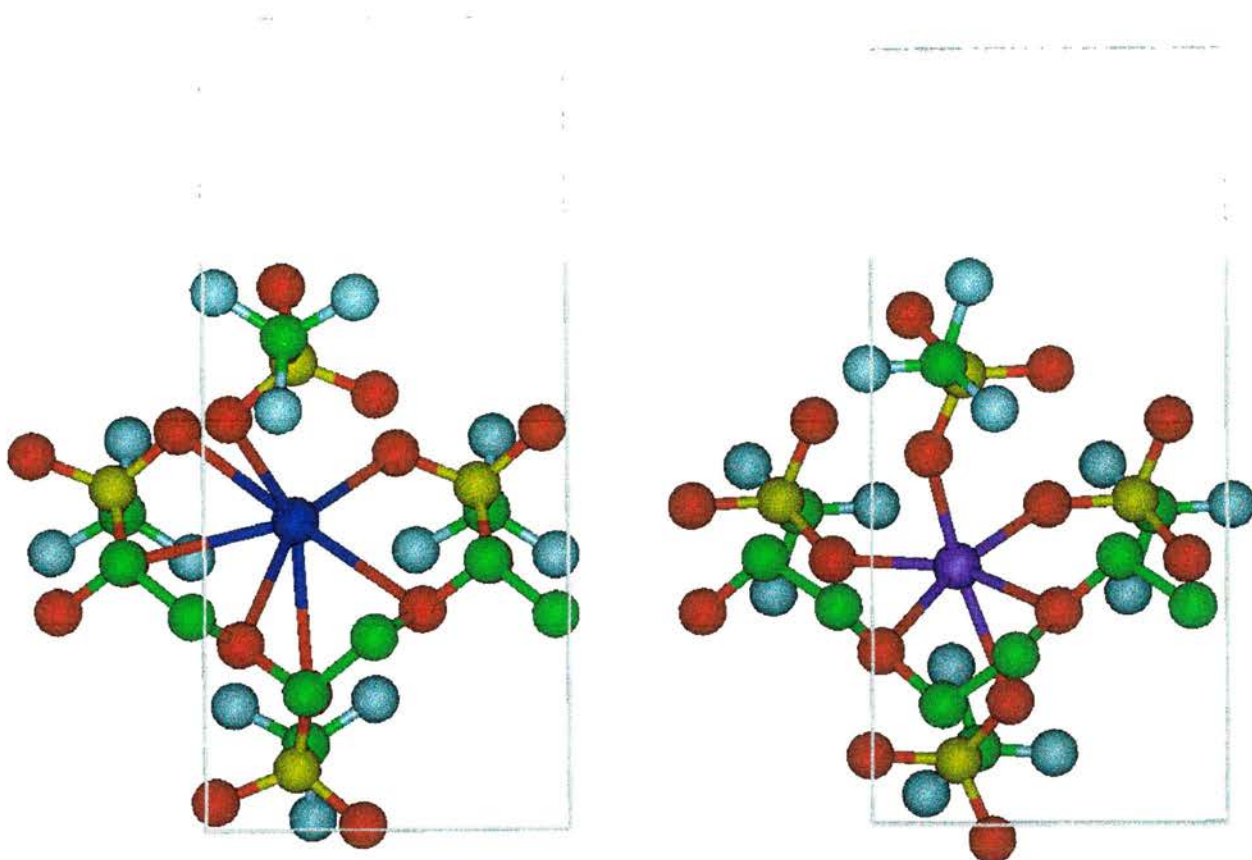


Fig. 7.2: A comparison of the structures of PEO:KCF<sub>3</sub>SO<sub>3</sub>, left, with that of PEO:NaCF<sub>3</sub>SO<sub>3</sub>, right. Green – carbon, red – oxygen, grey – fluorine, yellow – sulphur, blue – potassium, purple – sodium.

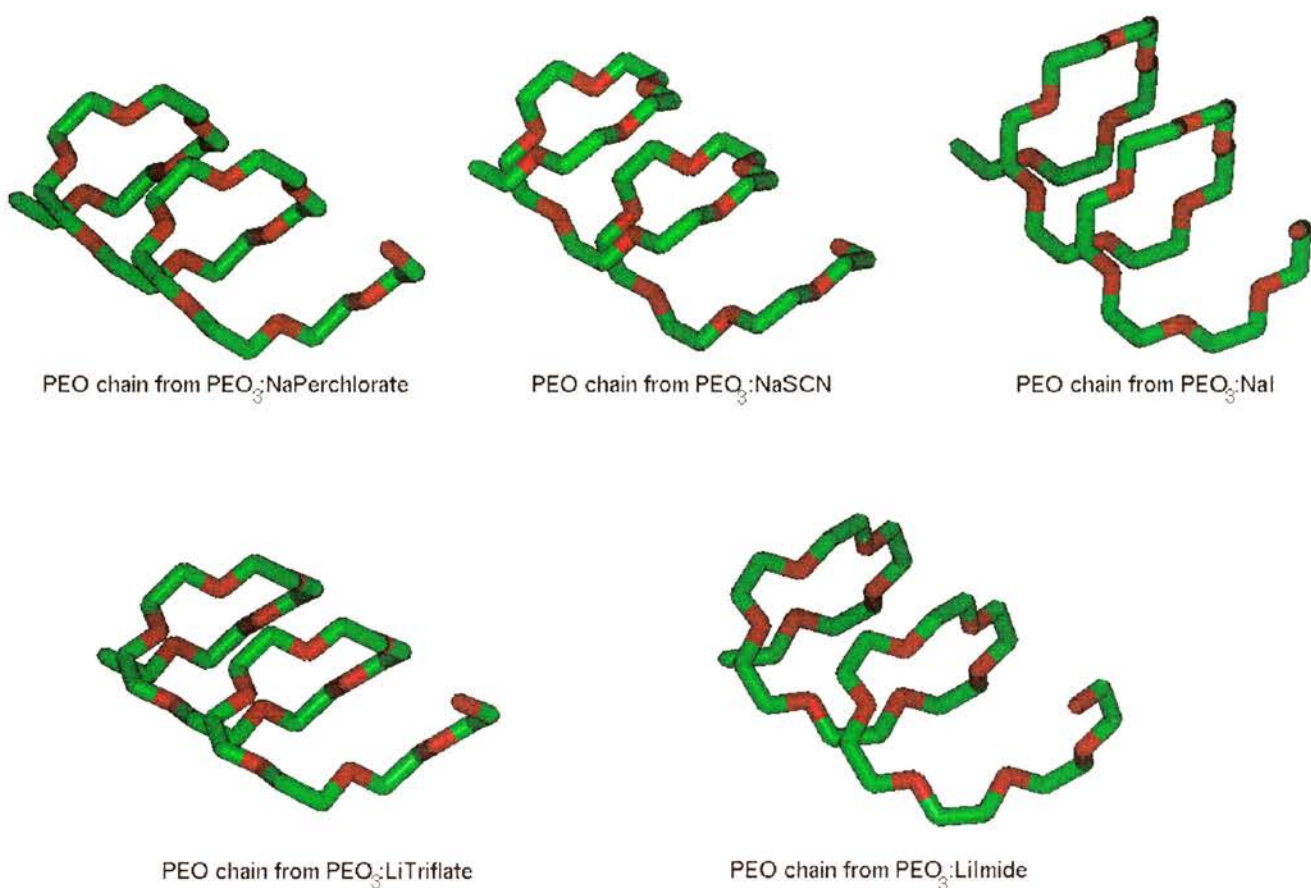


Fig. 7.3: A comparison of the chains from all of the  $\text{PEO}_3$ :salt 3:1 compounds solved to date.

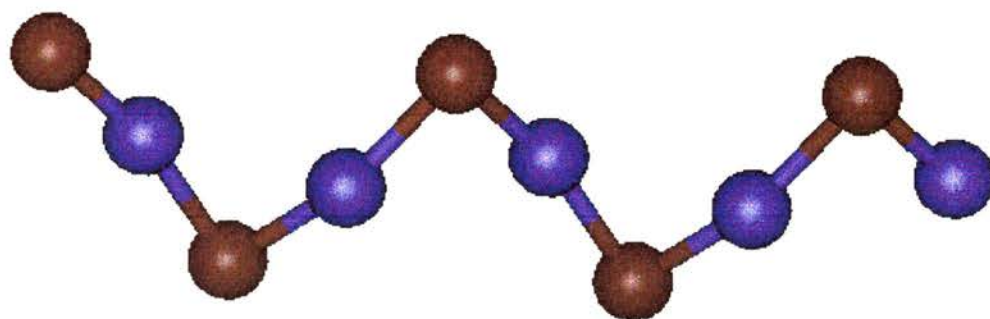


Fig. 7.4: Ion pairing in  $\text{PEO}_3:\text{NaI}$ .

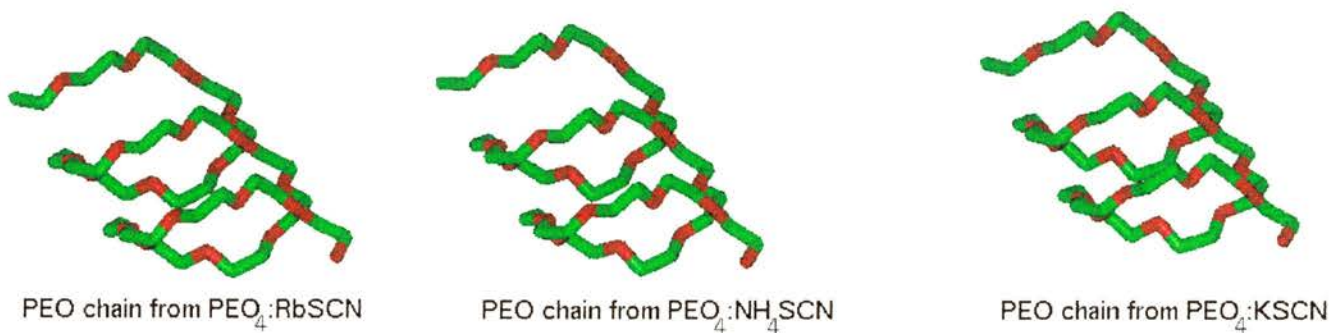
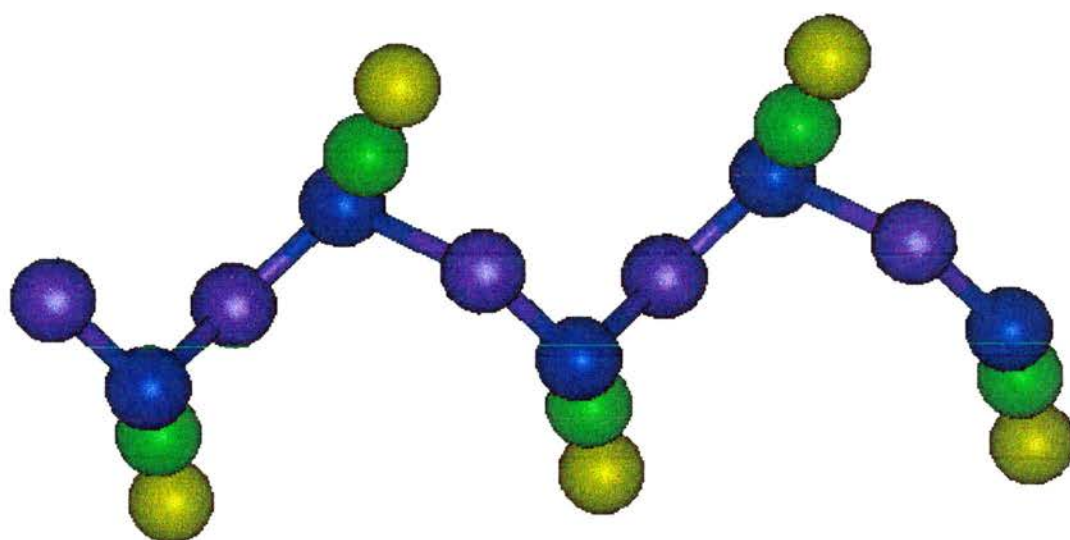


Fig. 7.5: A comparison of the PEO chains from all the PEO:salt 4:1 compounds solved to date.



Cation/anion pairing in  $\text{PEO}_4:\text{KSCN}$

Fig. 7.6: An example of ion clustering in PEO:salt 4:1 compounds.

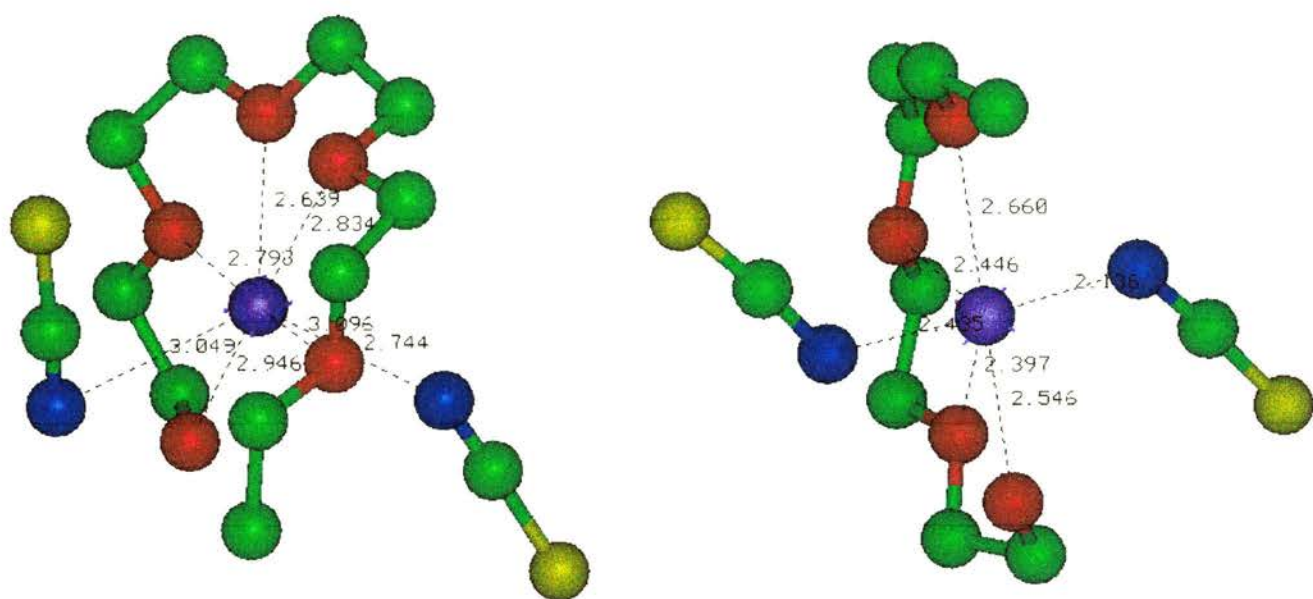


Fig. 7.7: A comparison of the cationic coordination in a 4:1 compound (PEO<sub>4</sub>:KSCN, left) with that of a 3:1 compound (PEO<sub>3</sub>:NaSCN, right).

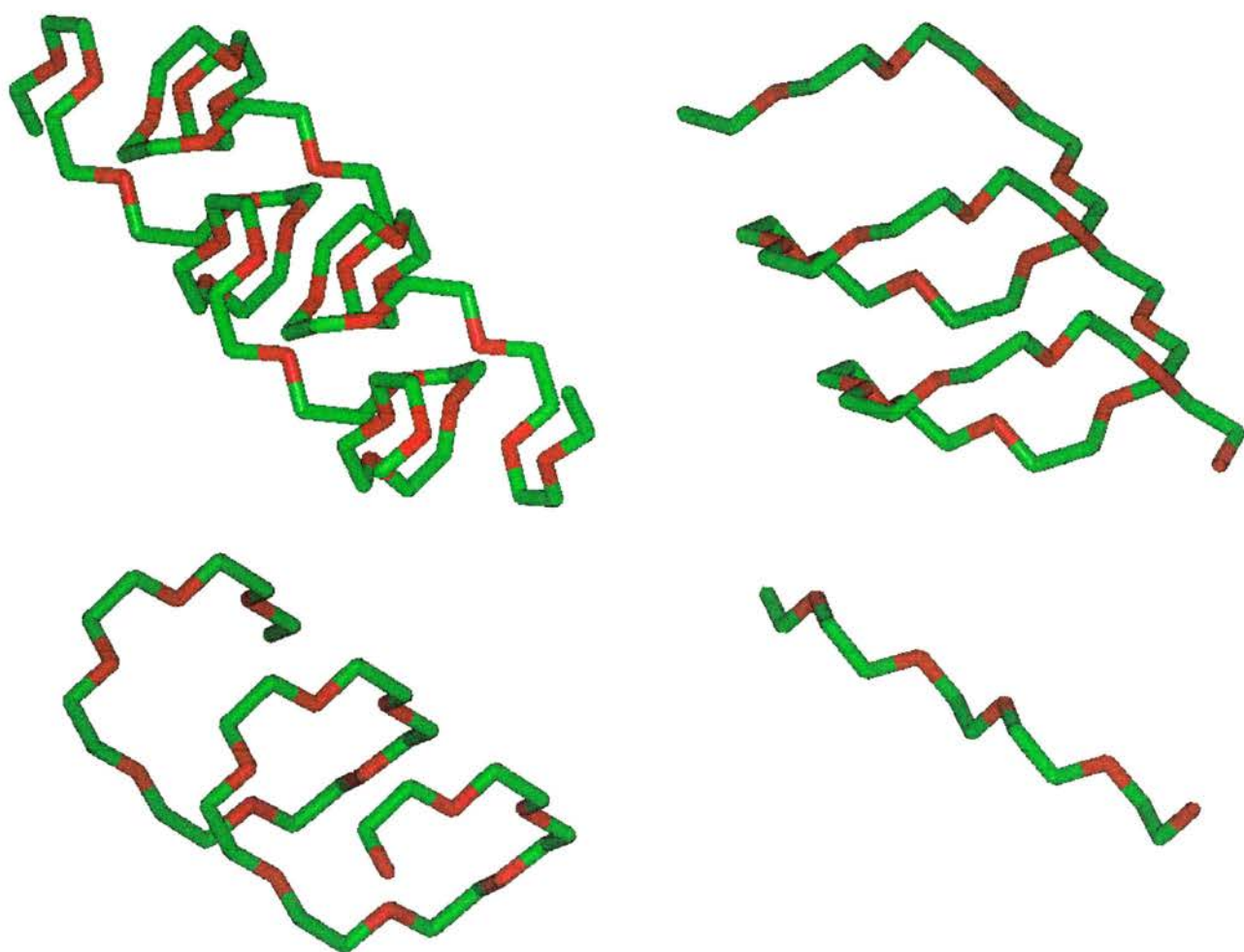


Fig. 7.8: A comparison of the PEO chains of a 6:1 compound ( $\text{PEO}_6\text{LiAsF}_6$ , top left) with that of a 4:1 compound ( $\text{PEO}_4\text{:KSCN}$ , top right), a 3:1 compound ( $\text{PEO}_3\text{:LiTriflate}$ , bottom left) and a 1:1 compound ( $\text{PEO}:\text{NaCF}_3\text{SO}_3$ , bottom right).

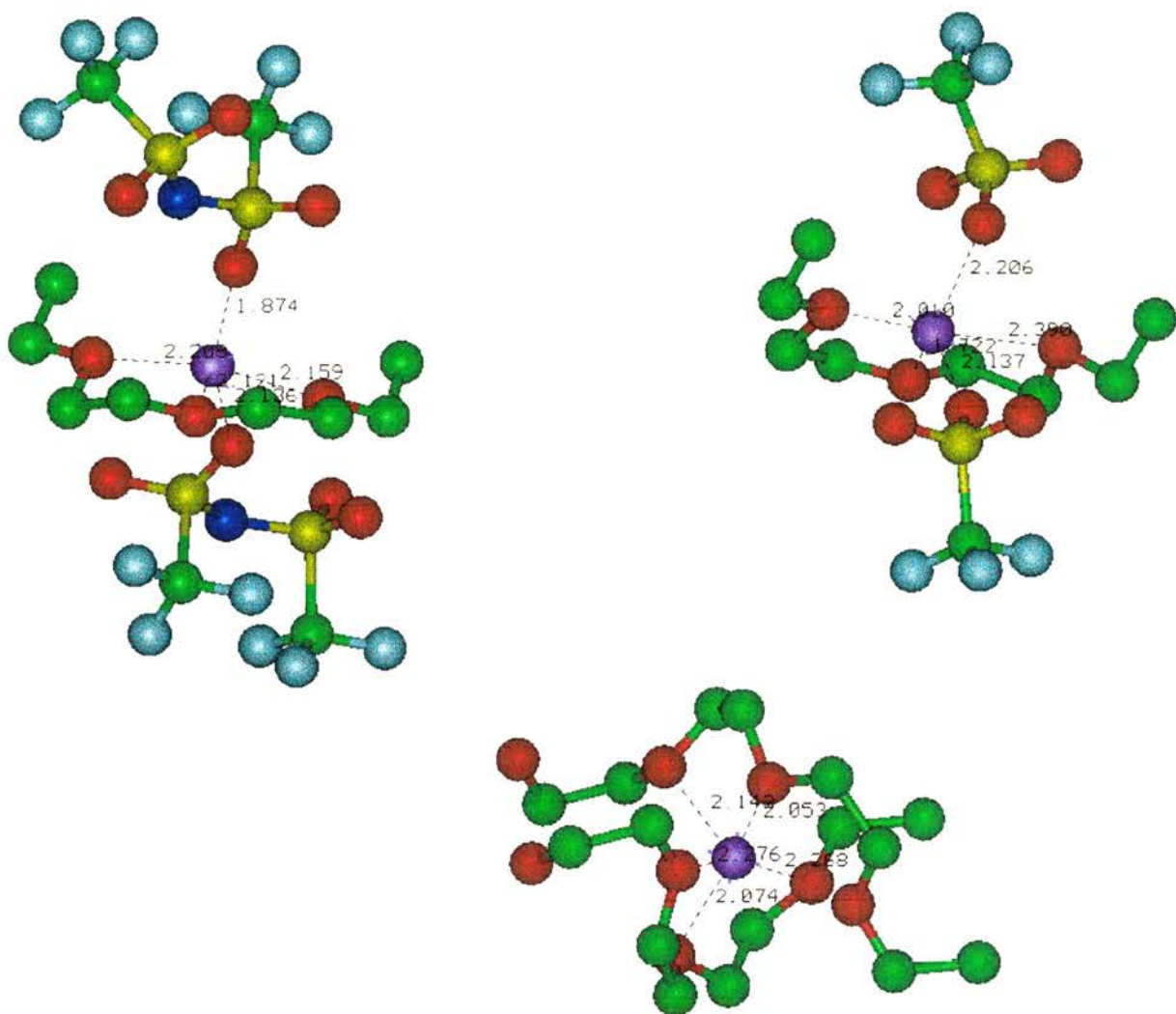


Fig. 7.9: Cationic coordination in the three PEO:Lithium salt compounds solved to date,  $\text{PEO}_3:\text{LiImide}$ , top left;  $\text{PEO}_3:\text{LiTriflate}$ , top right and  $\text{PEO}_6:\text{LiAsF}_6$ , bottom.

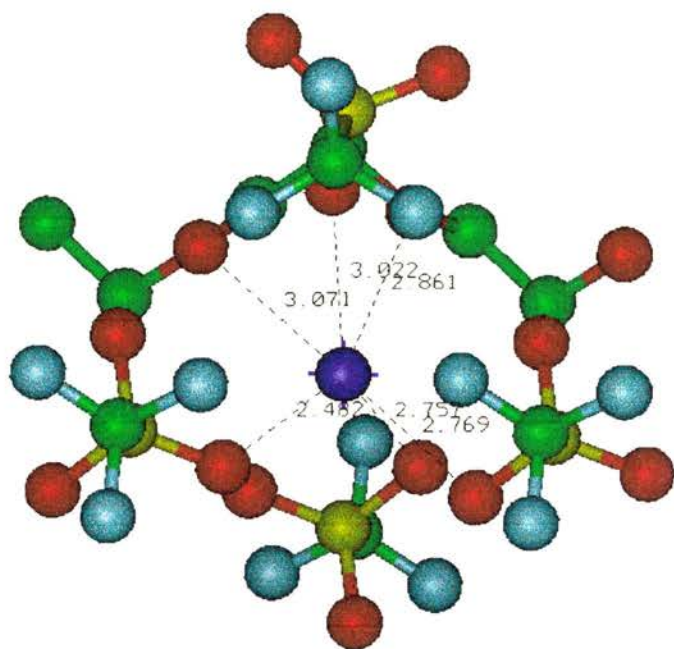
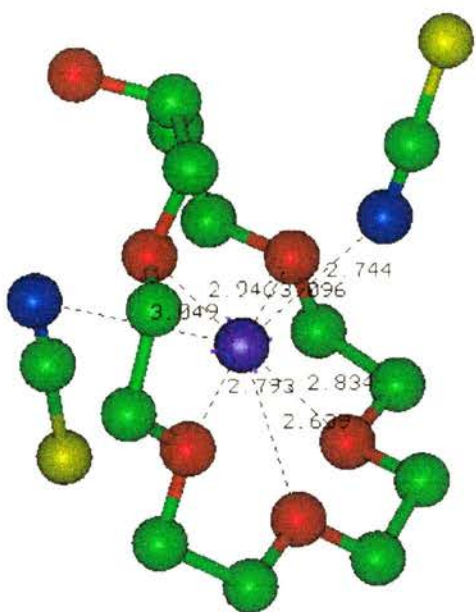
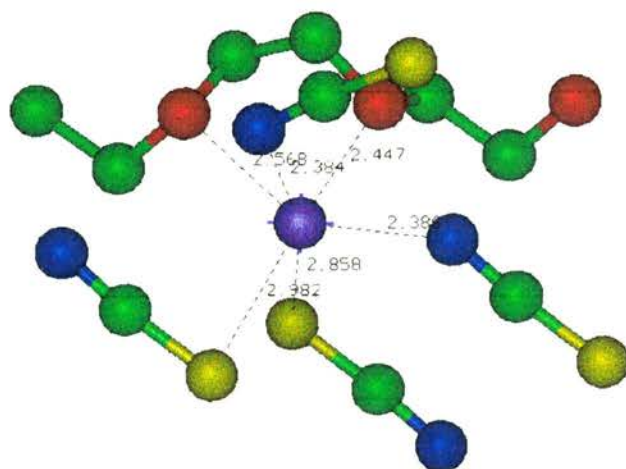
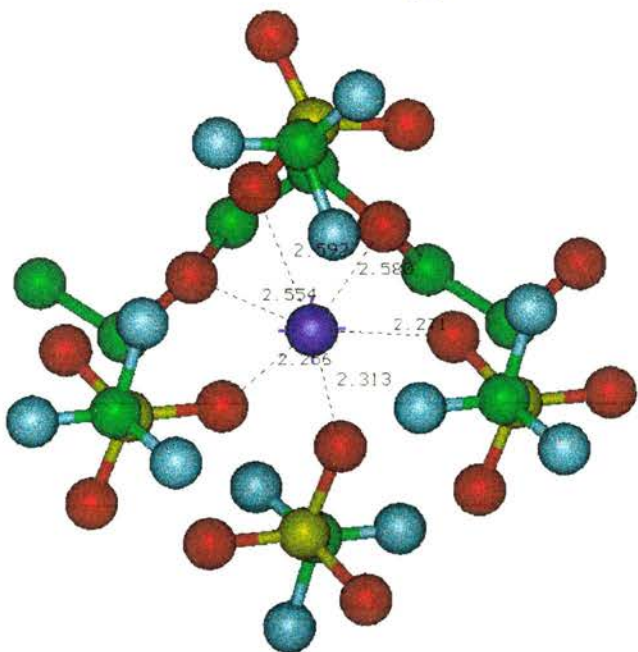
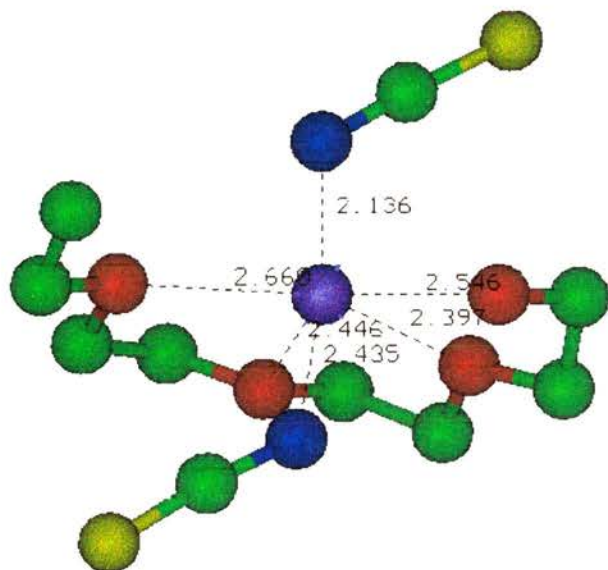
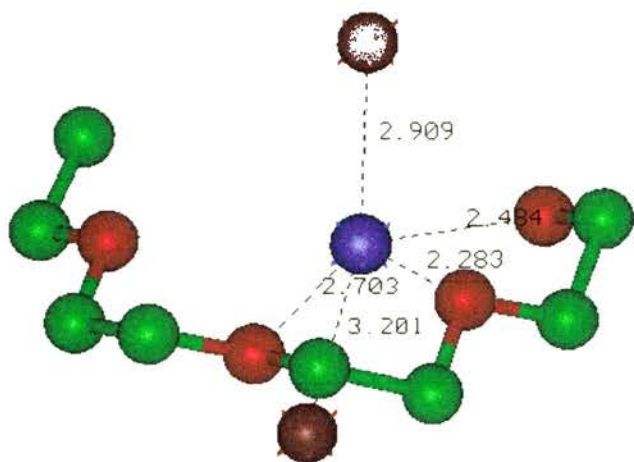
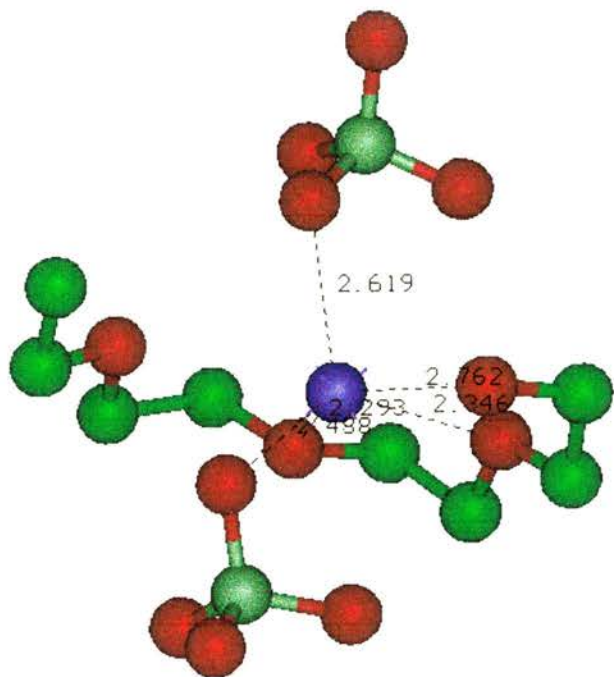


Fig. 7.10: Potassium coordination in PEO<sub>4</sub>:KSCN (left) and PEO:KCF<sub>3</sub>SO<sub>3</sub> (right).

Fig. 7.11: Following page. A comparison of the sodium coordination in all of the PEO:Nasalt compounds solved to date, top left: PEO<sub>3</sub>:NaClO<sub>4</sub>, top right, PEO<sub>3</sub>:NaI, centre: PEO<sub>3</sub>NaSCN, bottom left: PEO:NaTrflate, bottom right: PEO:NaSCN.



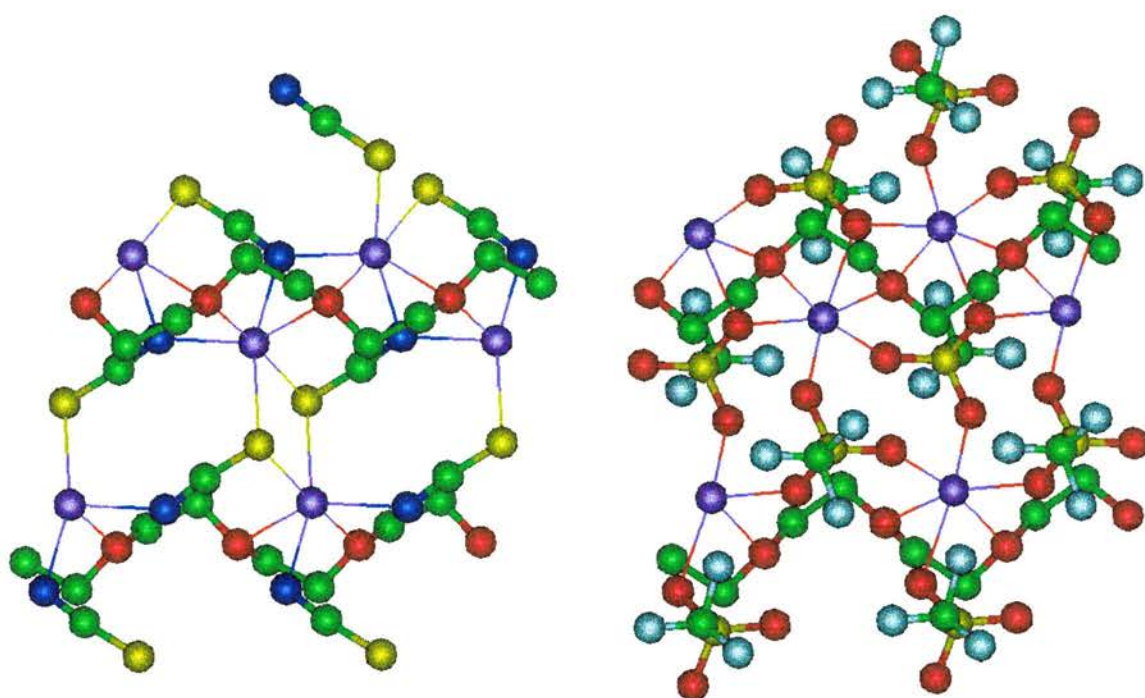


Fig. 7.12: A comparison of the structure of PEO:NaSCN, left, with that of PEO:NaCF<sub>3</sub>SO<sub>3</sub>, right.

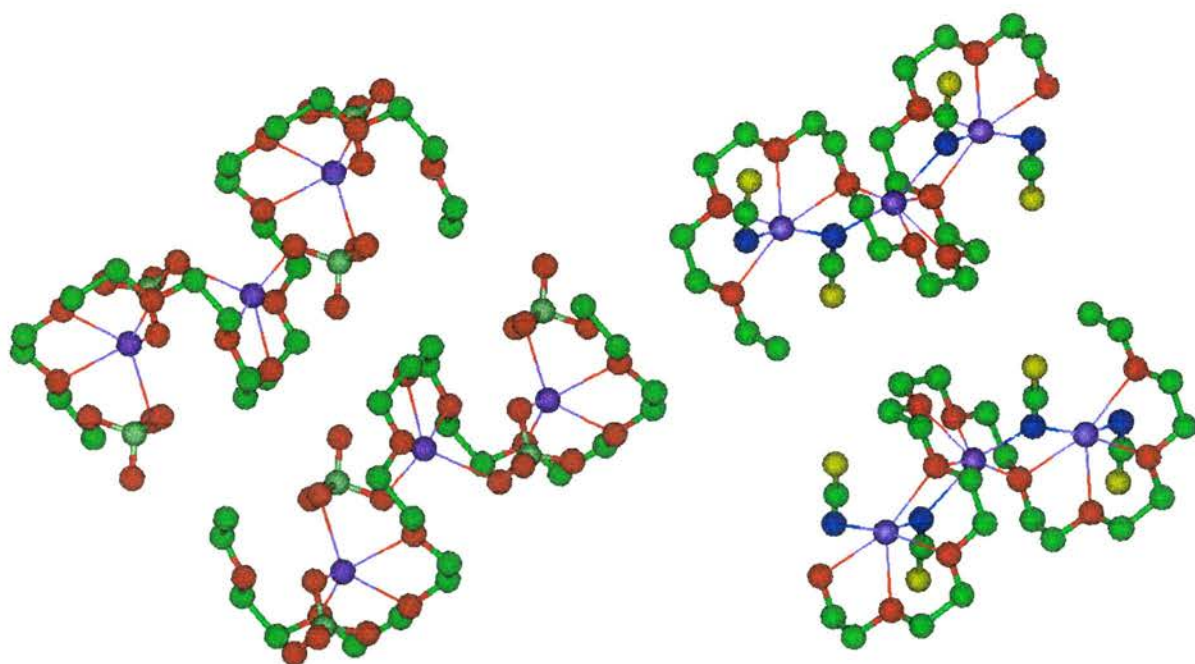


Fig. 7.13: A comparison of the structure of PEO:NaClO<sub>4</sub>, left, with that of PEO<sub>3</sub>:NaSCN, right.

**APPENDIX 1: The work presented in this thesis was also published in the following papers:**

- "Structure of the polymer electrolyte PEO6:LiAsF6", G.S.MacGlashan, Y.G.Andreev, P.G.Bruce, *Nature* **398** (1999) 792
- P.G.Bruce, G.S.MacGlashan, Y.G.Andreev in *Implications of Molecular and Materials Structure for New Technologies*, ed. J.A.Howard and F.H.Allen, *Nato Science Series E: Applied Sciences*, Kluwer, Dordrecht, 1999-05-16
- "Structure of the polymer-salt co-ordination complex  $[(\text{CH}_2\text{CH}_2\text{O})_n]:\text{KCF}_3\text{SO}_3$ , obtained from powder diffraction data", G.S.MacGlashan, Y.G.Andreev, P.G.Bruce, *Journal Of The Chemical Society-Dalton Transactions*, **6** (1998) 1073
- "Ab initio solution of a complex crystal structure from powder-diffraction data using simulated-annealing method and a high degree of molecular flexibility", Y.G.Andreev, G.S.MacGlashan, P.G.Bruce, *Physical Review B-Condensed Matter*, **55** (1997) 12011

## APPENDIX 2: Summary of PEO:salt Compounds Solved to Date

Compound	EO:salt ratio	Date Solved	Space Group / Unit Cell	PEO chain conformation / cation position	Cationic Co-ord. number
PEO <sub>4</sub> :HgCl <sub>2</sub>	4:1	1968	Ccmm a=13.55Å, b=8.58Å, c=11.75Å	Stretched chain / cations external	-
PEO:HgCl <sub>2</sub>	1:1	1969	Pncm a=7.75Å, b=12.09Å, c=5.88Å	Stretched zig-zag / cations external	-
PEO <sub>3</sub> :NaI	3:1	1987	P2 <sub>1</sub> /a a=18.15Å, b=8.41Å, c=7.98Å, β=122.3°	Helix / Cations enclosed	5 (PEO:3, Anion:2)
PEO <sub>3</sub> :NaSCN	3:1	1990	P2 <sub>1</sub> /a a=16.83Å, b=10.64Å, c=7.19Å, β=125.5°	Helix / Cations enclosed	6 (PEO:4, Anion:2)
PEO:NaSCN	1:1	1990	P2 <sub>1</sub> /c a=7.55Å, b=12.10Å, c=5.83Å, β=97.5°	Stretched zig-zag / cations external	6 (PEO:2, Anion:4)
PEO <sub>3</sub> :NaClO <sub>4</sub>	3:1	1992	P2 <sub>1</sub> /a a=18.32Å, b=8.35Å, c=8.58Å, β=123.1°	Helix / Cations enclosed	5 (PEO:3, Anion:2)
PEO <sub>3</sub> :LiCF <sub>3</sub> SO <sub>3</sub>	3:1	1993	P2 <sub>1</sub> /a a=16.77Å, b=8.61Å, c=10.07Å, β=121.0°	Helix / Cations enclosed	5 (PEO:3, Anion:2)
PEO <sub>4</sub> :KSCN	4:1	1994	C2/c a=25.51Å, b=8.08Å, c=16.10Å, β=126.0°	Large Helix / Cations enclosed	7 (PEO:5, Anion:2)

PEO <sub>4</sub> :NH <sub>4</sub> SCN	4:1	1994	C2/c a=26.66Å, b=8.23Å, c=15.80Å, β=125.6°	Large Helix / Cations enclosed	7 (PEO:5, Anion:2)
PEO <sub>4</sub> :RbSCN	4:1	1996	C2/c a=25.75Å, b=8.23Å, c=16.05Å, β=126.0°	Large Helix / Cations enclosed	7 (PEO:5, Anion:2)
PEO <sub>3</sub> :LiN(CF <sub>3</sub> SO <sub>2</sub> ) <sub>2</sub>	3:1	1996	P2 <sub>1</sub> /c a=12.03Å, b=8.66Å, c=19.14Å, β=128.5°	Helix / Cations enclosed	5 (PEO:3, Anion:2)
PEO:NaCF <sub>3</sub> SO <sub>3</sub>	1:1	1997	P2 <sub>1</sub> /c / a=9.83Å, b=12.75Å, c=5.76Å*, β=90.604°	Stretched zig- zag / cations external	6 (PEO:2, Anion:4)
PEO:KCF <sub>3</sub> SO <sub>3</sub>	1:1	1998	P2 <sub>1</sub> /c / a=9.98Å, b=13.44Å, c=5.93Å*, β=89.28°	Stretched zig- zag / cations external	7 (PEO:2, Anion:5)
PEO <sub>6</sub> :LiAsF <sub>6</sub>	6:1	1999	P2 <sub>1</sub> /a / a=11.87Å*, b=17.537Å, c=9.227Å, β=108.21°	Two saw- tooth chain, interlocking to form a cylinder / cations enclosed	5 (PEO:5, Anion:0)